Laminar Natural Convection Heat Transfer from Isothermal Horizontal Cylinders with Annular Fins

by

Chong-Sheng Wang

A thesis
presented to the University of Waterloo
in fulfillment of the
thesis requirement for the degree of
Doctor of Philosophy
in
Mechanical Engineering

Waterloo, Ontario, Canada, 1997

The University of Waterloo requires the signatures of all persons using or photocopying this thesis. Please sign below, and give address and date.

Abstract

A study is presented for laminar natural convection from horizontal cylinders with annular fins, which are referred to as annular-fin heat sinks in the following context. To simplify the analysis, the surfaces of the heat sinks are assumed to be isothermal. The heat sinks used for experimental studies in this work were made from aluminum, with a large ratio of fin thickness to fin diameter, thereby providing surfaces which were very close to isothermal. Previous studies on these types of heat sinks have not included the effects of fin thickness and end surfaces in the derived correlations.

A comprehensive model is presented for predicting natural convection heat transfer from these annular-fin heat sinks. It overcomes the shortcomings of the previous correlations. The model makes the distinction between the external and internal surfaces of the heat sink, allowing the heat transfer mechanisms that dominate on each of these surfaces to be more easily applied.

An approximate heat transfer solution for fully developed flow between the annular fins is obtained. The fully developed flow solution and an existing boundary layer solution for laminar natural convection are employed to construct the model. The model accounts for heat transfer from all surfaces of the heat sink, including the end surfaces and the rim of the fins. The Nusselt number of the heat sink is given as a function of the modified Rayleigh number or Elenbaas number. To account for the radiative heat loss, a radiation model for annular-fin heat sinks is also given.

Measurements for natural convection heat transfer from five heat sinks were performed and are used to validate the model. Radiative heat losses for these heat sinks were obtained from radiation measurements performed in a vacuum chamber.

The model is compared with the present experimental data, previous correla-

tions and experimental data, including the two limiting cases, i.e. disk channels and circular cylinders, plus a set of apple core data. Good agreement is observed in all comparisons. It confirms that the isothermal simplification is justified.

The model provides engineers with a useful tool for designing heat sinks.

Acknowledgments

I would like to express gratitude to my supervisor, Dr. M. M. Yovanovich, for his guidance, advice and support. Working with him has been a rewarding experience for me.

I would like to thank my co-supervisor, Dr. R. J. Culham, for his help and advice during the course of this study.

My thanks also go to the members of my examining committee:
Dr. E. Brundrett, Dr. K. G. T. Hollands, Dr. A. Nathan and Dr. P. H. Oosthuizen for their valuable suggestions.

I would like to thank everyone in the Microelectronics Heat Transfer Laboratory, especially Pete Teertstra for his kind help to all kinds of questions.

I gratefully acknowledge Mr. A. Hodgson for his assistance in my experiments. I also thank Mr. M. Van Reenen for his kind help in the experiments and other things.

Thanks are also extended to my friends both in the Department of Mechanical Engineering and outside for their encouragement and advice.

Finally, I would like to thank my parents and especially my wife Deyin, whose valuable support and patience made the finishing of this work possible.

Dedication

to

My wife

Contents

List of Figures

List of Tables

Nomenclature

A	=	surface area, m^2
A_{CC}	=	surface area of circumscribed cylinder, $\equiv \pi D^2/2 + \pi DL$, m^2
A_{CCS}	=	surface area of channel control surface, $\equiv \pi Db$, m^2
A_{CL}	=	surface area of one channel, $\equiv \pi(D^2 - d^2)/2 + \pi db$, m^2
A_{IN}	=	inner surface area, $\equiv (N_f - 1)A_{CL}$, m^2
A_i	=	component surface area in Eq. (4.21), m^2
A_{OUT}	=	outer surface area, $\equiv \pi D^2/2 + N_f \pi Dt$, m^2
A_{HS}	=	total surface area of heat sink, $\equiv A_{IN} + A_{OUT}$, m^2
b	=	spacing between adjacent fins, m
C	=	constant in Eq. (2.7)
C_1, C_2	=	constants in Eq. (2.4) and Eq. (2.8)
C_0, C_3	=	constants in Eq. (2.8)
$\overline{C}_l$	=	coefficient in Eq. (2.22), Eq. (2.23) and defined in Eq. (2.24)
$\overline{C}_{lm}$	=	coefficient in Eq. (2.15)
C^*	=	heat capacity of test body in Eq. (2.17)
D	=	fin outer diameter, m
d	=	diameter of support cylinder, m
d_e	=	mean diameter in Eq. (2.5), m
F	=	view factor in Eq. (4.57)
$F(Pr)$	=	Prandtl number function
$\mathcal{F}, \mathcal{F}_1, \overline{\mathcal{F}}_2$	=	exchange factors in Eq. (3.1)
G	=	body gravity function
g	=	gravitational acceleration, m/s^2
H	=	height of parallel plates, m
h	=	convection heat transfer coefficient, $W/m^2\,K$
I_0, K_0, I_1, K_1	=	modified Bessel function in Eq. (4.63)
k	=	thermal conductivity, $W/m\,K$
L	=	length of heat sink, $\equiv tN_f + (N_f - 1)b$, m
$\mathcal{L}$	=	arbitrary characteristic length, m
m	=	parameter in Eq. (4.63)
m_1	=	parameter in Eq. (2.16)
N_f	=	total number of fins
Nu^0	=	diffusive limit Nusselt number as $Ra \to 0$
$Nu_{\sqrt{A}}$	=	Nusselt number with $\sqrt{A}$ as characteristic length, $\equiv Q_{Conv}\sqrt{A}/A\Delta T\,k$
Nu_b	=	Nusselt number for heat sink based on A_{HS} and with b as characteristic length, $\equiv Q_{Conv}b/A_{HS}\Delta T\,k$

Nu_d	=	Nusselt number with d as characteristic length in Eq. (2.10), $\equiv Q_{Conv} d / A_{HS} \Delta T\, k$
Nu_e	=	Nusselt number with e as characteristic length in Eq. (2.11), $\equiv Q_{Conv} e / A_{HS} \Delta T\, k$
$Nu_{\mathcal{L}}$	=	Nusselt number with $\mathcal{L}$ as characteristic length, $\equiv Q_{Conv} \mathcal{L} / A \Delta T\, k$
Nu_s	=	Nusselt number with s as characteristic length for parallel plates, $\equiv Q_{Conv} s / A \Delta T\, k$
n	=	Churchill-Usagi blending equation parameter
n^*	=	dimensionless normal in Eq. (4.9)
P_d^*	=	dimensionless pressure component in Eq. (4.2) - Eq. (4.4)
$P(\theta)$	=	local perimeter of axisymmetric surface at certain value of θ, m
Q_{Conv}	=	heat flow rate by convection, W
Q_{HSR}	=	heat sink radiation loss in Eq. (3.1), W
Q_R	=	heat flow rate by radiation, W
Q_T	=	total heat transfer in Eq. (2.20), W
Q_W	=	wire heat loss in Eq. (2.20), W
Q_{WR}	=	wire radiation loss in Eq. (3.1), W
$Ra_{\sqrt{A}}$	=	Rayleigh number with $\sqrt{A}$ as characteristic length, $\equiv g\beta \Delta T \sqrt{A}^3 / \nu\alpha$
Ra_b^*	=	modified Rayleigh number, or Elenbaas number, $\equiv g\beta \Delta T\, b^4 / \nu\alpha D$
Ra_{cr}, Ra_d	=	Rayleigh numbers defined in Eq. (2.10)
Ra_D	=	Rayleigh number with D as characteristic length, $\equiv g\beta \Delta T D^3 / \nu\alpha$
$Ra_{\mathcal{L}}$	=	Rayleigh number with $\mathcal{L}$ as characteristic length, $\equiv g\beta \Delta T \mathcal{L}^3 / \nu\alpha$
Ra_s^*	=	modified Rayleigh number for parallel plates, $\equiv g\beta \Delta T\, s^4 / \nu\alpha H$
S	=	total length of surface streamline in Eq. (2.22), m
s	=	spacing of parallel plates, m
$\overline{T}_a$	=	average ambient temperature in Eq. (2.18), K
T_b	=	surface temperature of test body in Eq. (2.17), K
T_S	=	surface temperature of heat sink, K
T_{tv}	=	temperature measured by thermovision system in Eq. (2.11), K
T_w	=	temperature of vacuum chamber wall, K
T_∞	=	temperature of ambient air, K
t	=	fin thickness, m
ΔT	=	temperature difference, $\equiv T_S - T_\infty$, K
u^*, v^*, w^*	=	dimensionless velocities in Eq. (4.1) - Eq. (4.5)
v_0	=	reference velocity in Eq. (4.5), m/s
x^*, y^*, z^*	=	dimensionless coordinates in Eq. (4.1) - Eq. (4.5)

Greek Symbols

α	=	thermal diffusivity of air, m^2/s
β	=	volumetric coefficient of thermal expansion, $1/K$
ζ	=	parameter of Eq. (2.8), $\equiv d/D$
ϵ	=	surface emissivity
θ	=	angle between outward normal and gravity vector, *radian*
θ^*	=	dimensionless temperature, $(T - T_\infty)/(T_S - T_\infty)$
ν	=	kinematic viscosity, m^2/s
τ	=	time, s
Φ	=	parameter of Eq. (4.63)
σ	=	Stefan-Boltzmann constant, $5.67 \times 10^{-8}\ W/m^2K^4$

Subscripts

CC	=	circumscribed cylinder
A_{CCS}	=	channel control surface area
A_{RIM}	=	fin rim surface area
A_{END}	=	end surface area
CCS	=	channel control surface, based on A_{CL}
CL	=	one channel
CLF	=	channel flow, based on A_{CL}
FD	=	fully developed regime
HS	=	heat sink
A_{IN}	=	inner surface area between adjacent fins, including support cylinder surfaces and lateral fin surfaces
A_{IN-FD}	=	inner surface area with fully-developed flow
A_{IN-T}	=	inner surface area with thin boundary layer flow
IN	=	inner surface; based on A_{HS}
A_{OUT}	=	outer surface area, including fin rims and two end surfaces
OUT	=	outer surface; based on A_{HS}
T	=	thin boundary layer regime
$\sqrt{A}$	=	based on $\sqrt{A}$, as the characteristic length

Superscripts

p,q	=	parameters in Eq. (2.4)
i	=	parameters in Eq. (2.22)
T	=	thin boundary layer regime

Chapter 1

Introduction

Heat dissipation is an important consideration in the design of many kinds of engineering equipment and instruments, such as air conditioners, refrigerators, electrical and electronics assemblies etc.. The use of heat sinks is a common, low cost means of increasing the effective surface area to enhance heat dissipation by convective air cooling. Heat sinks can be used in applications with either forced or natural convection, but natural convection has a distinct reliability advantage since there is no need to use an external source of power to move the cooling fluid. In the event of a fan failure, natural convection can be considered as the fail safe mode of operation. In some cases, fail safe operation can be crucial for the equipment, e.g. aviation electrical and electronics devices, and some communication equipment etc. In computers and other electronic systems, natural convection cooling can also enhance the reliability of the system when compared with forced convection cooling. Therefore natural convection cooling is appealing to many researchers.

Horizontal cylinders with annular fins, a typical cooling structure as shown in Fig. 1.1, will be investigated in the present study and referred to as annular-fin heat sinks in the following context. It is one type of widely used heat sinks in engineering practice.

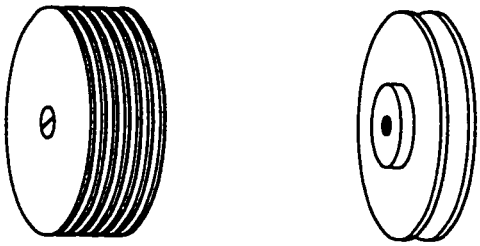

(a)

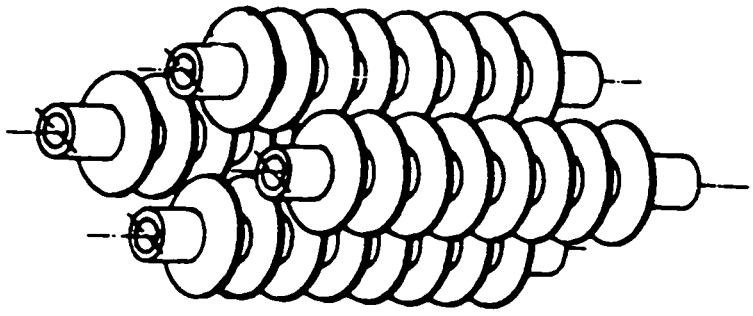

(b) (Kayansayan and Karabacak, 1992)

Figure 1.1: Heat Sinks with Annular Fins.

1.1 Problem Definition

A schematic of the annular-fin heat sink used in this study is shown in Fig. 1.2. in a horizontal orientation, where the gravity force is parallel to the annular fins. The heat sink consists of N_f identical fins with a centrally located circular support cylinder. Each fin section has a fin thickness, t, an outer diameter, D and an inner diameter, d. Adjacent fin sections are separated by a distance, b and the overall length of the heat sink is L.

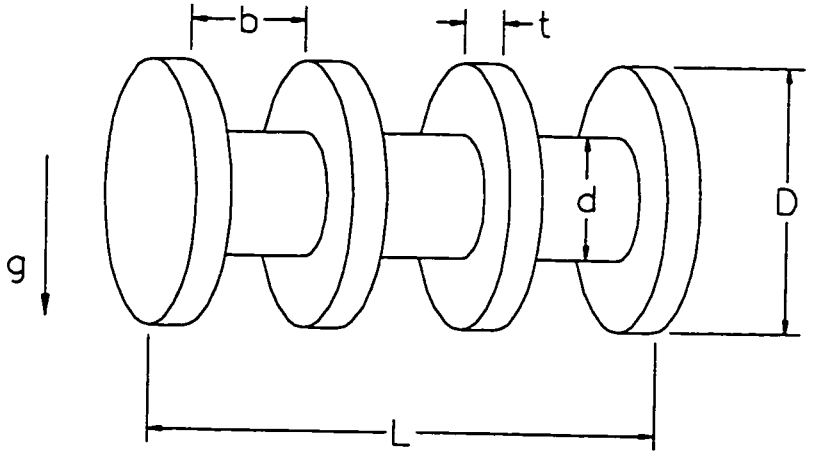

Figure 1.2: Geometric Parameters of Heat Sink.

In this study the surface of the heat sink is assumed to be isothermal and the spacing b is used as the characteristic length (Elenbaas, 1942: Edwards and Chaddock, 1963; Jones and Nwizu, 1969; Tsubouchi and Masuda, 1970). The Nusselt number is defined as

$$Nu_b = \frac{Q}{A\,\Delta T}\frac{b}{k} \tag{1.1}$$

and the modified Rayleigh number or Elenbaas number is (Elenbaas, 1942; Edwards and Chaddock, 1963; Jones and Nwizu, 1969; Tsubouchi and Masuda, 1970)

$$Ra_b^* = \frac{g\beta\,\Delta T\,b^3}{\alpha\nu}\frac{b}{D} \tag{1.2}$$

where ΔT is the temperature difference between the heat sink surface and the ambient air.

Often it is required to design a heat sink given a fixed set of design conditions, such as overall size, shape etc.. In these instances, engineers need to find optimum dimensional values, e.g. spacing b, fin thickness t and diameter ratio D/d etc.. To be able to achieve this efficiently, an accurate and easy-to-use model is very important for the designers. Numerical software, as general computation tools, can be used for this purpose, but they are much more expensive and time consuming.

The objective of this study is to develop a comprehensive model that will account for the effects of all geometric parameters, such as spacing b, diameter ratio d/D, fin thickness t and fin number N_f, thereby providing engineers with a useful design tool.

1.2 Overview of the Thesis

This thesis is arranged in the following manner.

In Chapter 2, previous studies on this problem, relevant experimental methods and boundary layer solutions are briefly reviewed.

In Chapter 3, the experimental method used in the present study is described; then the experimental results for five heat sinks are reported.

In Chapter 4, the models for laminar natural convection are developed for annular-fin heat sinks.

In Chapter 5, the present model is compared with previous correlations, present experimental data and some previous experimental data.

In Chapter 6, a summary and conclusions are presented.

Chapter 2

Literature Review

In this chapter, a brief review of ten pertinent correlations is presented and a summary table of the correlations is given in the following section. Then comparisons between the previous correlations are made in Subsection 2.1.2. A brief review of relevant experimental methods and boundary layer solutions is given in Section 2.2 and Section 2.3.

2.1 Previous Work on Heat Sinks

2.1.1 Previous models and correlations

Elenbaas Model

Elenbaas (1942) reported both analytical and experimental results of natural convection from vertical parallel plates. He used the steady state heat balance method in which resistors are embedded in the plates and the measured voltage and current values are then used to determine the convective heat transfer. He was the first worker to adopt $Ra_s(s/H)$ as the correlating parameter and his experimental results were correlated by

$$Nu_s = \frac{1}{24} Ra_s^* \left[1 - \exp\left(\frac{-35}{Ra_s^*}\right)\right]^{3/4} \tag{2.1}$$

where $Ra_s^* = Ra_s(s/H)$, s is the spacing between the plates and H is the height of the plates.

As $Ra_s^* \longrightarrow 0$, the above equation predicts heat transfer for the fully-developed channel flow where

$$Nu_s = \frac{1}{24} Ra_s^* \tag{2.2}$$

On the other hand, as $Ra_b^* \longrightarrow \infty$ the equation collapses to the one predicting laminar natural convection heat transfer from a single vertical plate:

$$Nu_s = 0.6(Ra_s^*)^{1/4} \tag{2.3}$$

Although Eq. (2.1) was obtained for parallel plates, after being modified it has been extensively used for calculating heat losses from finned surfaces.

Edwards and Chaddock Correlations

Edwards and Chaddock (1963) used an experimental method similar to that of Elenbaas to measure heat transfer from cylindrical disk extended surfaces. Based on the form of the Elenbaas equation and using fitting techniques, they developed correlations for 3 different diameter ratios (D/d = 1.94, 2.97, 5.17) and 3 materials namely copper, aluminum and stainless steel. In their experiments the fin thickness was fixed at 0.5 mm. The temperature of the support cylinder was taken as the temperature of the heat sink. They reported the following correlation:

$$Nu_b = C_1(Ra_b^*)^p \left[1 - \exp\left(\frac{-C_2}{Ra_b^*}\right)\right]^q \tag{2.4}$$

where $5 < Ra_b^* < 10^4$ and the parameters are as given in Table 2.1 through Table 2.3.

Table 2.1: Parameters for Copper Fins.

D/d	C_1	C_2	p	q
5.17	0.1065	106	0.5510	0.2953
2.97	0.1255	155	0.5292	0.2599
1.94	0.1250	137	0.5506	0.2943

Table 2.2: Parameters for Aluminum Fins.

D/d	C_1	C_2	p	q
5.17	0.0845	101	0.6137	0.3346
2.97	0.1165	57	0.5295	0.2199
1.94	0.1463	296	0.4903	0.2070

Table 2.3: Parameters for Stainless Steel Fins.

D/d	C_1	C_2	p	q
5.17	0.0510	65	0.4611	0.1827
2.97	0.1002	120	0.4784	0.2207
1.94	0.1347	466	0.4758	0.2174

Knudsen and Pan Correlation

Knudsen and Pan (1963) reported their experimental results for natural convection heat transfer from tubes with circular fins. They used the mean diameter, $d_e = (D + d)/2$, as the characteristic length. They gave the following correlation:

$$Nu_e = 0.201 \left[Ra_e \left(\frac{b}{d} \right) \right]^{1/3} \tag{2.5}$$

where $10^{4.4} < Ra_e < 10^{5.6}$, and

$$Nu_e = \frac{h\, d_e}{k}$$

$$Ra_e = \frac{g \beta \Delta T\, d_e^3}{\alpha \nu}$$

This correlation is a straight line in log-log plot. It does not represent the region of fully developed flow. A least square analysis was used to obtain the parameters. The average deviation of their experimental data from the correlation is ±7.5%.

Jones and Nwizu Correlation

Jones and Nwizu (1969) measured heat transfer from horizontal tubes with circular fins for four diameter ratios (D/d = 1.33, 1.50, 1.67 and 1.83) which were not covered by the Edwards-Chaddock experiments. In their experimental apparatus, a guard section at each end of the finned tube was introduced to minimize end losses. The guard sections were heated separately and maintained at the same temperature level as the test section. Thus the heat transfer is eliminated at the end surfaces as shown in Fig. 2.1. Their correlation is similar to that of Elenbaas. It gives 10% smaller values when compared with that of Edwards and Chaddock.

A plain horizontal cylinder was tested with the same apparatus, and the data lying 5% below the correlation of McAdams (1954) were found. So the authors concluded that their data were slightly conservative. Their correlation for diameter ratios of $D/d = 1.33$ to 1.83 was given as

$$Nu_b = 0.116(Ra_b^*)^{0.53}\left[1 - \exp\left(\frac{-155}{Ra_b^*}\right)\right]^{0.26} \tag{2.6}$$

where $1 < Ra_b^* < 3\times10^3$. The ratio of fin thickness to fin height, i.e. $t/(D/2-d/2)$, ranged from 0.16 to 0.4. It is relatively larger than those of the other studies reviewed here.

Tsubouchi and Masuda Correlations

Tsubouchi and Masuda (1970) measured heat transfer from horizontal cylinders with circular fins for 30 cases with values of D/d ranging from 1.14 to 3.73.

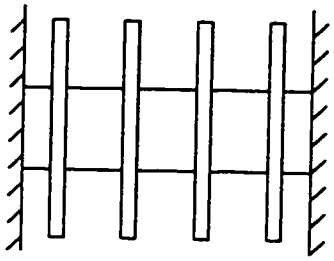

Figure 2.1: Test Section of the Heat Sink.

The guard sections were introduced at two ends of the cylinder. Two sets of correlations were presented: one for the fin rim surface and the other for the lateral fin surfaces with supporting cylinder surface respectively, referring to Fig. 2.2. The air properties are evaluated at the wall temperature. The correlations given below are for the fin rim surface ($2 \leq Ra_b^* \leq 10^4$).

$$Nu_b = C\,(Ra_b^*)^p \tag{2.7}$$

Table 2.4: Parameters for Fin Rim Surfaces.

D/d	3.73	3.00	2.45	1.82	1.36	1.14
C	0.9	0.8	0.66	0.66	0.62	0.59
p	0.29	0.29	0.29	0.29	0.29	0.27
t (mm)	2	2	2	1.5	1	1

They developed correlations for the lateral fin surfaces with the supporting cylinder for the range of $3 < Ra_b^* < 10^4$.

For the diameter ratio range of $1 \leq D/d \leq 1.67$, they proposed the following correlation:

$$Nu_b = C_0 Ra_0^p \left\{1 - \exp\left[-\left(\frac{C_1}{Ra_0}\right)^{C_2}\right]\right\}^{C_3} \tag{2.8}$$

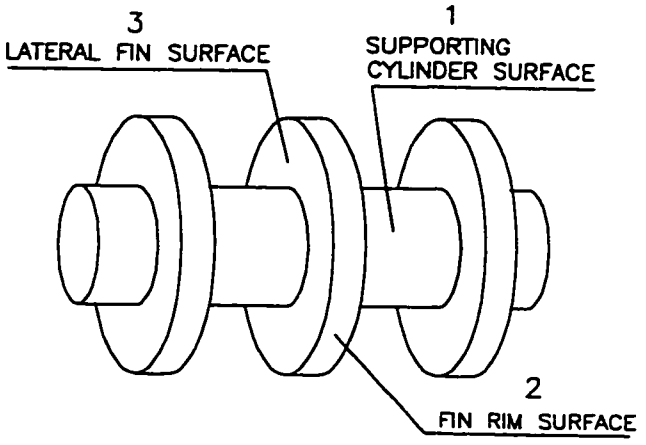

Figure 2.2: Surfaces of a Heat Sink.

where

$$\zeta = d/D$$

$$C_0 = -0.15 + 0.3\zeta + 0.32\zeta^{16}$$

$$C_1 = -180 + 480\zeta - 1.4\zeta^{-8}$$

$$C_2 = 0.04 + 0.9\zeta$$

$$C_3 = 1.3(1-\zeta) + 0.0017\zeta^{-12}$$

$$p = \frac{1}{4} + C_2 C_3$$

$$Ra_0 = Ra_b^* (D/d)$$

For the large values of the diameter ratios $1.67 < D/d < \infty$, they gave the following correlation:

$$Nu_b = \frac{Ra_b^*}{12\pi} \left\{ 2 - \exp\left[-\left(\frac{C_1}{Ra_b^*} \right)^{3/4} \right] - \exp\left[-\beta \left(\frac{C_1}{Ra_b^*} \right)^{3/4} \right] \right\} \qquad (2.9)$$

where

$$\zeta = d/D$$

$$\beta = 0.17\zeta + e^{-4.8\zeta}$$

$$C_1 = \left[\frac{23.7 - 1.1(1 + 152\zeta^2)^{1/2}}{1+\beta}\right]^{4/3}$$

Kayansayan and Karabacak Correlation

Kayansayan and Karabacak (1992) measured natural convection heat transfer from horizontal cylinders with vertically attached circular fins for 16 cases. They gave a correlation for high Rayleigh numbers, which predicts smaller values of Nusselt number near the Ra_{cr} defined below than those of previous correlations. The diameter of supporting cylinder was chosen as characteristic length. The correlation is

$$Nu_d = 0.081 Ra_d^{0.336} \tag{2.10}$$

The correlation is valid for the following ranges of the parameters:

i) $1.5 < D/d < 6.0$ and

ii) $0.25 < b/d < 1.0$ and

iii) $Ra_d > Ra_{cr}$

where

$$Ra_{cr} = 6.11 \times 10^7 (d/D)^3$$

Hahne and Zhu Correlation

Hahne and Zhu (1994) used a heat balance method and a thermovision system *AGA*, model 782 to measure the dissipated heat and the surface temperature. The two end surfaces were coated with black paint in order to obtain a uniform

emissivity close to 1. They did not separate the convection heat loss from the radiation loss. Therefore the correlation given in the paper predicts the total heat loss, including radiation, for D/d = 4.38, 5.63 and 6.88. The effective diameter, $d_e = d + (D - d)/2$, was chosen as the characteristic length. The correlation is as follows:

$$Nu_e = \frac{h\,d_e}{k} = 0.376\left(Ra_e\frac{b}{d}\right)^{0.308} \tag{2.11}$$

where

$$h = \frac{Q_{VI}}{A_{HS}(T_{tv} - T_\infty)}$$

and

$$Ra_e = \frac{g\beta\,(T_{tv} - T_\infty)\,d_e^3 Pr}{\nu^2}$$

where Q_{VI} is the heating rate, T_{tv} is the heat sink temperature measured by thermovision system, T_∞ is the ambient temperature, A_{HS} is the total surface area of the heat sink. The applicable region of the correlation is

$$5 \times 10^4 \leq Ra_e\,(b/d) \leq 5 \times 10^5$$

Bar-Cohen and Rohsenow Correlation for Plate Channel

Bar-Cohen and Rohsenow (1984) obtained a correlation for vertical channel of isothermal plates. They employed the Churchill and Usagi (1972) blending equation and gave the following correlation for the plate channel:

$$Nu_s = \left[(Ra_s^*/24)^{-n} + (0.59Ra_s^{*1/4})^{-n}\right]^{-1/n} \tag{2.12}$$

where $Ra_s^*/24$ is the solution for fully developed regime, and $0.59Ra_s^{*1/4}$ is the solution for isothermal vertical plate. The parameter n is approximately equal to 2. The correlation shows good agreement with the data of Elenbaas (1942) for a vertical channel.

Raithby and Hollands Correlation for Square Fins

Raithby and Hollands (1985) correlated the experimental data of Elenbaas (1942) for square plates and gave the following equation for square fin arrays without the central support cylinder:

$$Nu_s = \left[\left(\frac{Ra_s^{*0.89}}{18} \right)^{-2.7} + (0.62 Ra_s^{*1/4})^{-2.7} \right]^{-1/2.7} \tag{2.13}$$

This equation should account for the edge effect of the square plate channel.

Karagiozis Model for Rectangular Fin Arrays

Karagiozis (1991) developed a model for rectangular fin arrays. It contained three regimes: low Rayleigh number regime, intermediate Rayleigh number regime and high Rayleigh number regime. For the low Rayleigh number regime, the heat transfer rate was taken to be the same as that from the circumscribed cuboid of the fin arrays. It was calculated using the method of Hassani-Hollands (1989). In the intermediate Rayleigh number regime, the fully developed heat transfer between the parallel plates was added to the Nusselt number of the low Rayleigh number regime. The fully developed heat transfer was calculated by the correlation for parallel plates (Elenbaas, 1942):

$$Nu_s = \frac{1}{24} Ra_s^* \tag{2.14}$$

where $Ra_s^* = Ra_s(s/H)$, s is the spacing between the plates and H is the height of the plates. In the high Rayleigh number regime, the vertical plate correlation was used which is

$$Nu_s = \overline{C}_{lm} (Ra_s^*)^{1/4} \tag{2.15}$$

where $\overline{C}_{lm}$ was determined by a fitting technique based on the experimental results. In order to use the blending method, the correlation for high Rayleigh number

regime was modified as

$$Nu_s = \overline{C}_{lm} \left\{ Ra_s^* \left[1 + \left(\frac{C}{Ra_s^*} \right)^{m_1} \right] \right\}^{1/4} \tag{2.16}$$

where C and m_1 were determined by a trial and error procedure.

Finally the Nusselt number for intermediate Rayleigh number regime and the modified Nusselt number for high Rayleigh number regime were blended using the Churchill and Usagi equation to give the correlation for the full range of Rayleigh number.

A summary of the previous studies on annular-fin heat sinks reviewed above is given in Table 2.5.

Table 2.5: Summary of Previous Studies on Annular-Fin Heat Sinks.

Authors	L (mm)	t (mm)	d (mm)	D (mm)	D/d	Ra_b^*	end guard	material
Edwards-Chaddock (1963)	152	0.5	19.1	37.1 56.7 98.7	1.94 2.97 5.17	$5-10^4$	No	Cu[1] Al[2] SS[3]
Knudsen-Pan (1963)	305	-	35	60.3 73.0 85.7	1.73 2.10 2.45	$10^{4.4}-10^{5.6}$ for Ra_e	No	Cu
Jones-Nwizu (1969)	320	2.54	38	50.8 57.2 63.5 69.9	1.33 1.50 1.67 1.83	$1-3\times10^3$	Yes	Al
Tsubouchi-Masuda (1970)	195	1 1 1.5 2 2 2	22	25 30 40 54 66 82	1.14 1.36 1.82 2.46 3.00 3.73	$2-10^4$	Yes	Al
Kayansayan-Karabacak (1992)	600	2	200 150 100 50	300	1.5 2.0 3.0 6.0	$Ra_d > Ra_{cr}$	insulating layer	Cu
Hahne-Zhu (1994)	45	1	16	70 90 110	4.38 5.63 6.88	$5\times10^4-5\times10^5$ for $Ra_e(b/d)$	No	Cu

1 copper; 2 aluminum; 3 stainless steel.

2.1.2 Comparison of previous correlations

In Fig. 2.3, the correlations of Edwards-Chaddock, Knudsen-Pan, Jones-Nwizu, Tsubouchi-Masuda and Kayansayan-Karabacak are plotted together. For the purpose of comparison, a diameter ratio of 1.94 is chosen, which is valid for most of the correlations except for the Hahne-Zhu correlation.

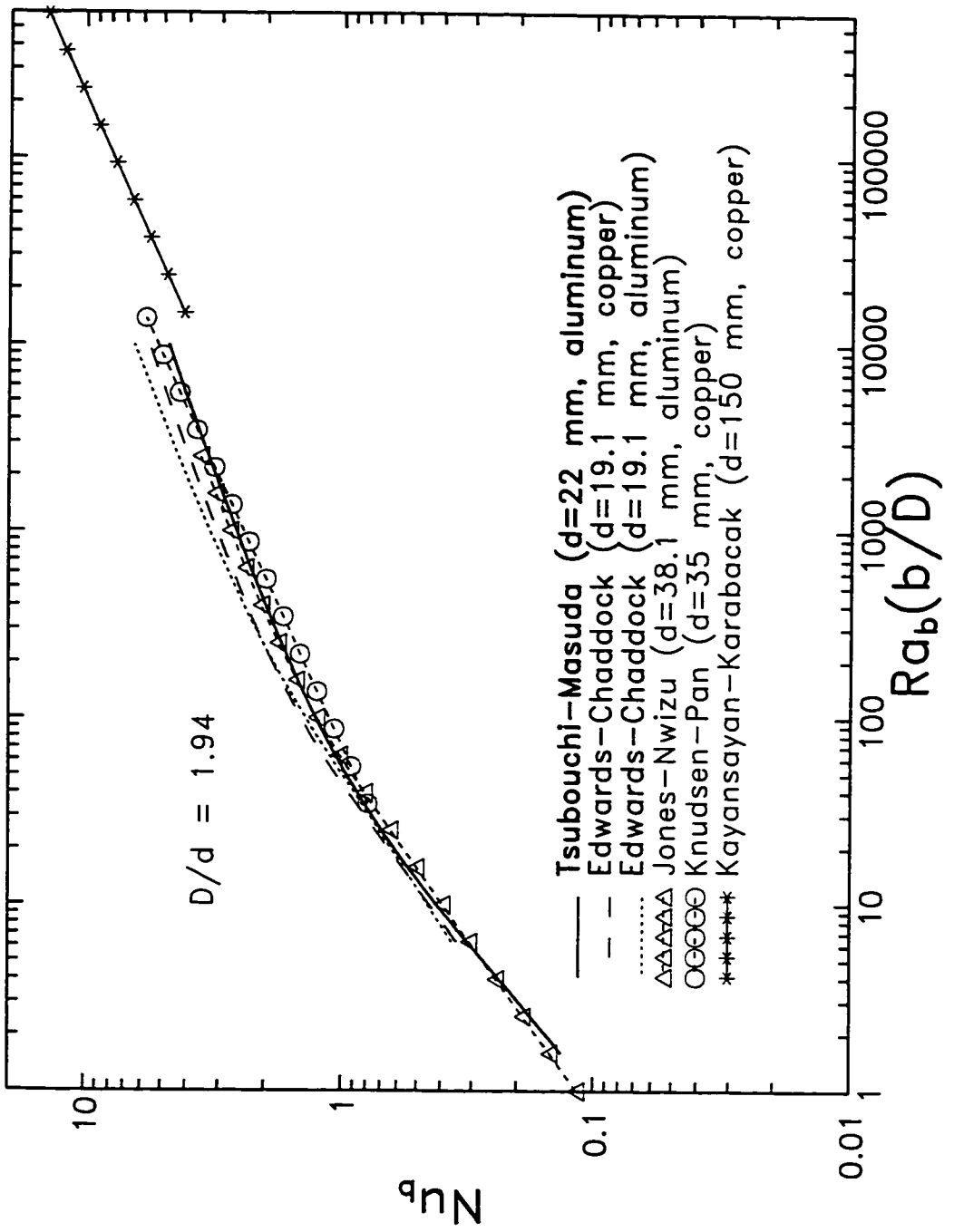

Figure 2.3: Comparison of Previous Correlations.

The Edwards-Chaddock, Jones-Nwizu and Tsubouchi-Masuda correlations have a form similar to that of Elenbaas. They show the same trend, but there are larger differences at high Ra_b^*.

Knudsen and Pan proposed a simple form of correlation, which is a straight line in a log-log plot, it gives large deviations from the Tsubouchi-Masuda correlation, the Jones-Nwizu correlation and the Edwards-Chaddock correlation around Ra_b^* = 100.

The Kayansayan-Karabacak correlation is valid for high Ra_b^*, e.g. $1.5 \times 10^4 - 2.5 \times 10^7$ for D/d = 2. It has a simple form and shows large deviations in its low Ra_b^* region, e.g. $Ra_b^* = 1.5 \times 10^4$ from all the other correlations.

In most previous experiments (Edwards and Chaddock, 1963; Knudsen and Pan, 1963; Jones and Nwizu, 1969; Tsubouchi and Masuda, 1970; Kayansayan and Karabacak, 1992), for each case, the Ra_D is more or less fixed because the temperature difference ΔT varied within a narrow range (a factor of 20 at most), and the pressure was at atmospheric. The wide range of Ra_b^* was achieved by variation of b/D (note: $Ra_b^* = Ra_D b^4/D^4$). Therefore each of their correlations represents a series of heat sinks with different values of b/D. The other geometric parameters (t/D, d/D and L/D) of these heat sinks were fixed.

On the other hand, Karagiozis (1991) performed the experiment in a different manner, where all geometric parameters were fixed for each case and the wide range of Ra_b^* was achieved through a variation of the ambient air pressure. Therefore each of his correlations represents a group of heat sinks which are similar to each other. In other words, each correlation represents the heat sinks whose geometric parameters (t/D, b/D, d/D or L/D) are identical.

From the above review it can also be seen that

i) The differences between the correlations for annular-fin heat sinks can be as high as 40%.

ii) The effect of fin thickness variation is not included in the previous correlations.

iii) End surfaces are not considered separately. Therefore the previous correlations would not be applicable to those cases where end surfaces have significant contribution to the total heat transfer, e.g. the annular-fin heat sinks used in electronic systems which usually have only a few fins as shown in Fig. 1.1 (a).

Accordingly, there is a need to do some experiments to clarify the discrepancy and to develop a more comprehensive model to account for the effects of fin thickness and end surfaces as well as the other parameter effects.

2.2 Relevant Experimental Methods

All the experiments mentioned in Section 2.1 were done using a steady state heat balance method. This method involves introducing electric power into the physical model body (heat sink), measuring the supplied power when the heat transfer becomes steady state, and subtracting the radiation loss which was calculated according to the measured heat sink temperature and the ambient temperature. This method is based on a first law energy balance.

As mentioned in the above section, in the experiment of Karagiozis (1991) the modified Rayleigh number Ra_b^* varied with the pressure. In this case, one can obtain a wide range of Rayleigh numbers (a factor of 10^6) with only one physical model body (Hollands, 1988). One of the advantages of this approach is that by varying the ambient pressure, one can match the Rayleigh number of the physical model to that of the real engineering problem, especially when the real dimensional scale is much larger or much smaller than the physical model scale.

In previous studies, Hassani and Hollands (1989), Clemes et al. (1994) and Karagiozis et al. (1994), a transient approach was used instead of a steady state

method. In this approach, the heat capacity of the test body needed to be measured accurately first. It was carried out in a vacuum chamber, a constant DC power was introduced into the test body and then the temperatures of the test body and the ambient as well as the supplied power were recorded at preset time intervals, until the steady state had been reached. In this process, the energy balance of the test body is

$$\frac{dT_b}{d\tau} = \frac{VI}{C^*} - \frac{\bar{\epsilon}A\sigma}{C^*}(T_b^4 - T_w^4) \tag{2.17}$$

where V and I are the voltage and current supplied to the heater embedded in the test body, T_b is the temperature of the test body and T_w is the temperature of the chamber wall, $\bar{\epsilon}$ is the effective emissivity of the model. A and C^* are the test body surface area and heat capacity respectively, and τ is time. The quantity of $dT_b/d\tau$ in Eq. (2.17) was estimated by employing the Langrange's formula for four point differentiation, and then plotted versus $(T_b^4 - T_w^4)$. Through performing a linear regression analysis, a straight line was obtained whose slope and intercept were taken as $\bar{\epsilon}A\sigma/C^*$ and VI/C^*. After inserting the values of V and I, C^* and $\bar{\epsilon}$ were obtained.

In the natural convection heat transfer experiment, a correlation was obtained first:

$$T_b(\tau) - \overline{T}_a = exp[P(\tau)] \tag{2.18}$$

where $\overline{T}_a$ is the average ambient temperature, $T_b(\tau)$ is the test body temperature, and $P(\tau)$ is a third order polynomial found by curve fitting. Then $dT_b(\tau)/d\tau$ was found by

$$\frac{dT_b(\tau)}{d\tau} = \frac{dP(\tau)}{d\tau} exp[P(\tau)] \tag{2.19}$$

Finaily Q_{Conv} was obtained by

$$Q_{Conv} = Q_T - Q_R - Q_W \tag{2.20}$$

with

$$Q_T = -C^* \frac{dT_b(\tau)}{d\tau} \tag{2.21}$$

where Q_T is the total heat transfer from the body, Q_R and Q_W are the radiation heat loss and conduction heat loss through the wires, respectively. Q_{Conv} is the convection heat flow rate.

This transient approach can save a lot of waiting time, i.e. the time allowing the heat transfer of a test body to reach steady state. Good agreement between the results of this approach and the steady state heat transfer measurements was observed by the authors. But some deviations of Nu for this transient approach from that of the steady state approach were also reported. In the comparisons of results for the two approaches, the maximum differences in Nusselt number are 4.6% at $Ra_D = 9300$ (Clemes, 1990) and 2.0% at $Ra_b^* = 600$ (Karagiozis, 1991). These deviations may include the experimental errors.

2.3 Relevant Boundary Layer Solutions

Acrivos (1960) obtained the boundary layer solutions for laminar natural convection heat transfer from two dimensional surfaces and axisymmetric surfaces as $Pr \to \infty$. Stewart (1971) generalized the solutions to fairly arbitrary three dimensional surfaces. But their solutions are applicable only to large Prandtl numbers.

Raithby and Hollands (1975, 1976, 1978) suggested the conduction-layer approximate method based on the concept proposed by Langmuir (1912), assuming that the body is surrounded by a stationary fluid layer of variable thickness. The solutions obtained by them have the same forms as that of Acrivos (1960) and Stewart (1971), but are applicable to arbitrary Prandtl numbers. Therefore their solutions generalized the previous ones to include lower Pr (e.g. $Pr = 0.71$ for air). Raithby and Hollands (1975, 1976, 1985) also suggested the approaches to

make correction for the curvature effect of boundary layers.

The thin boundary layer solutions for two-dimensional surfaces and axisymmetric surfaces are (Raithby and Hollands, 1975)

$$Nu_S = \overline{C}_l Ra_S^{1/4} \frac{\left[\frac{1}{S}\int_0^S (r^{4i} g_x/g)^{1/3} dx\right]^{3/4}}{\frac{1}{S}\int_0^S r^i dx} \tag{2.22}$$

where $i = 0$ for two-dimensional surfaces, $i = 1$ for axisymmetric surfaces, x is the distance measured along a surface streamline from its leading edge, S is the total length of the surface streamline and taken as the characteristic length, g is gravity acceleration and g_x is its component in the x direction.

With reference to Fig. 2.4, the solutions for vertical planar surfaces are (Raithby and Hollands, 1978)

$$Nu_{\mathcal{L}} = \overline{C}_l Ra_{\mathcal{L}}^{1/4} \frac{\mathcal{L}^{1/4}\int_0^W S^{3/4} d\chi}{\int_0^W S d\chi} \tag{2.23}$$

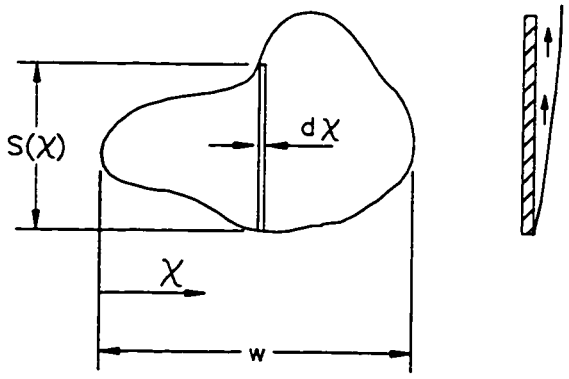

Figure 2.4: Vertical Planar Surface.

The value of $\overline{C}_l$ is based on the correlation of Churchill and Usagi (1972):

$$\overline{C}_l = \frac{0.671}{[1 + (0.492/Pr)^{9/16}]^{4/9}} \tag{2.24}$$

The above solutions show very good agreement with previous measurements, but they are not easy to be applied to practical problems with complex geometry. Therefore Hassani and Hollands (1989) proposed an improved Raithby and Hollands method, making several approximations and simplifications to the thin boundary layer analysis of Raithby and Hollands, and employing certain correlations for the mean conduction thickness and the exponents of the Churchill-Usagi blending equation. Good agreement was reported between experimental results and the predictions by this method.

Yovanovich (1987b,c) and Lee et al. (1991) used a characteristic length based on the surface area, $\sqrt{A}$, to recast the existing boundary layer solutions for laminar natural convection. They obtained a new expression of the boundary layer solutions for isothermal, three dimensional bodies. (The details are given in Chapter 4.) Their approach has the following advantages:

i) Because of the introduction of the characteristic length $\sqrt{A}$, the method gets rid of the difficulty of choosing a proper characteristic length for a body or a subsurface, especially for irregular and complex ones.

ii) The body-gravity function of each subsurface can be calculated separately and then combined with the body-gravity functions of the other sub-surfaces. This makes the method more feasible.

iii) The body-gravity function was found to be a weak function of geometry and orientation of the surfaces or bodies. Therefore the calculations of the body-gravity function mentioned above should not introduce much deviation in the final results.

iv) The method still keeps the approximate analytical nature of the boundary layer solutions.

2.4 Summary

The previous models and correlations of Elenbaas (1942), Edwards and Chaddock (1963) , Knudsen and Pan (1963), Jones and Nwizu (1969), Tsubouchi and Masuda (1970), Kayansayan and Karabacak (1992), Hahne and Zhu (1994). Bar-Cohen and Rohsenow (1984), Raithby and Hollands (1985), and Karagiozis (1991) are reviewed. The correlations for annular-fin heat sinks are compared with each other; up to 40% discrepancies are observed at high Ra_b^*. In addition, the correlations and models are not well suited to the heat sinks with only a few fins, because they do not take into account the effect of end surface cooling on the total heat transfer. These types of heat sinks are frequently used in electronic systems.

The relevant experimental methods and boundary layer solutions are also briefly reviewed.

In the next chapter, the experimental method and the results will be presented.

Chapter 3

Experiments and Data Reduction

The experimental method used in the present study is described in the following four sections. The data reduction procedure is given in Section 3.5 and the experimental results are presented in Section 3.6.

3.1 Experimental Method

When convection heat transfer takes place, radiation and conduction heat transfer usually also exist. To obtain the rate of heat transfer by convection, it is necessary to deduct the radiation and conduction portion of heat transfer from the total rate of heat transfer.

In some previous experiments (Edwards and Chaddock, 1963; Knudsen and Pan, 1963; Jones and Nwizu, 1969; Tsubouchi and Masuda, 1970), the radiation loss from heat sinks was estimated and then subtracted from the total heat transfer rate. In this case, the accuracy of the heat sink surface emissivity is important in the accurate estimation of radiation loss. Because the radiation loss is proportional to the emissivity.

In the present experiments the radiation loss was measured and correlated. Then the correlation was used to calculate the radiation loss in the convection measurements. In this approach, the radiation loss through the power leads and

the thermocouple wires was also accounted for by the correlation. Because the measured radiation loss includes the radiation loss from the wire surfaces. However. in the convection measurements there was an additional heat loss, i.e. the heat loss due to convection on the power leads and the thermocouple wire surfaces. To cover this additional heat loss, a calculation procedure, which was used to calculate this additional heat loss, has been developed and is presented in Appendix B.

To achieve accurate experimental results, a steady state heat balance method was used in the present study.

3.2 Physical Models

3.2.1 Heat sinks

Five heat sinks used in the present experiments are shown in Fig. A.1 through Fig. A.5 in Appendix A. The geometric parameters of the heat sinks are given in Table 3.1, where A_{IN} stands for the inner surface area, i.e. the total surface area between adjacent fins, including the surfaces of supporting cylinder; A_{OUT} for the outer surface area including fin rim surfaces and the two end surfaces of the heat sink; A_{HS} for the total surface area of the heat sink; and A_{CC} for the surface area of the circumscribed cylinder.

Table 3.1: Geometric Parameters for Test Heat Sinks. (length unit: mm)

Heat Sink	b	t	N_f	L	d	D	D/d	A_{IN}	A_{OUT}	A_{HS}	A_{CC}
A	22.5	10	3	75	22	36.5	1.66	5775	5533	11308	10693
B	7.5	9	5	75	22	36.5	1.66	7403	7253	14656	10693
C	4	9	6	74	22	36.5	1.66	8044	8285	16329	10578
D	2	9	7	75	22	36.5	1.66	8824	9317	18141	10693
E	1	10	7	76	22	36.5	1.66	8409	10120	18529	10807

The heat sinks were machined from aluminum alloy 2024 cylindrical bar stock. Thus the fins were an integral part of the support cylinder with no joints or contact resistance. The fin diameter D was fixed at 36.5 mm and the support cylinder diameter d at 22 mm. To see the effect of fin thickness on the total heat transfer of the heat sink, the fin thickness was made quite large, around 10 mm. And, to find the effect of the end surfaces on the total heat transfer, only a few fins were made for each heat sink. Thus the end surface heat transfer was significant in the total heat transfer, similar to that of the heat sinks used in electronic systems. In order to obtain data in different ranges of Ra_b^*, values of b for the five heat sinks were made as 22.5 mm, 7.5 mm, 4 mm, 2 mm and 1 mm.

The heat sinks were manufactured with the same procedure in the Engineering Machine Shop at the University of Waterloo. The tolerances for the small spacings ($b = 1$ mm and $b = 2$ mm) were less than 1%, and the tolerances for the other dimensions were well below 1% and the finish of the heat sink surfaces was 0.4 μm.

3.2.2 Heaters

A FIREROD cartridge heater was embedded in the center of the heat sink to provide a source for internal heat generation. The heater fit the mounting hole inside the heat sink well and the gap between the heater and the heat sink was filled with aluminum putty to discharge the air from the gap. The electrical resistance of the heater was 50 ohms and the applied voltage was varied from 2 to 25 volts. Because the power leads of the heater was relatively thick (each lead consisted of 7 wires and each wire had a diameter of 0.23 mm; material was Nickel 200), the heat loss through the power leads was taken into consideration in the experiments.

3.2.3 Thermocouples

T-type (copper-constantan) thermocouple wire of 36 gauge (a diameter of 0.127 mm) coated with Teflon were used in this study. All the thermocouples were made from the same high precision roll of wire using the identical technique. In the calibration, a maximum difference of 0.13 K was found compared with the Platinum resistance thermometer or PRT (Azonix Corporation Model No A12001) whose accuracy is better than 0.01 K.

Several thermocouples were embedded just under the heat sink surface at selected locations. As shown in Fig. 3.1, a groove of 1 mm width and 1 mm depth was cut out along the fin rim. The thermocouple along with a length of thermocouple wire was placed inside the groove and then the groove was filled with aluminum putty to provide support and additional electrical insulation. In this way the heat transfer through the thermocouple wire will not interfere with the temperature field at the location of the thermocouple. The heat loss through the thermocouple wire was also taken into consideration in the present experiments. Temperatures were measured at typical locations for each heat sink. For example, for heat sink A shown in Fig. 3.1, thermocouples were embedded at the highest point and the lowest point of fins and support cylinders. Because of the symmetry, only one location was measured for the support cylinders and the end fins. The average temperature of the heat sink was calculated according to the measured temperatures and the local surface areas represented by the temperatures.

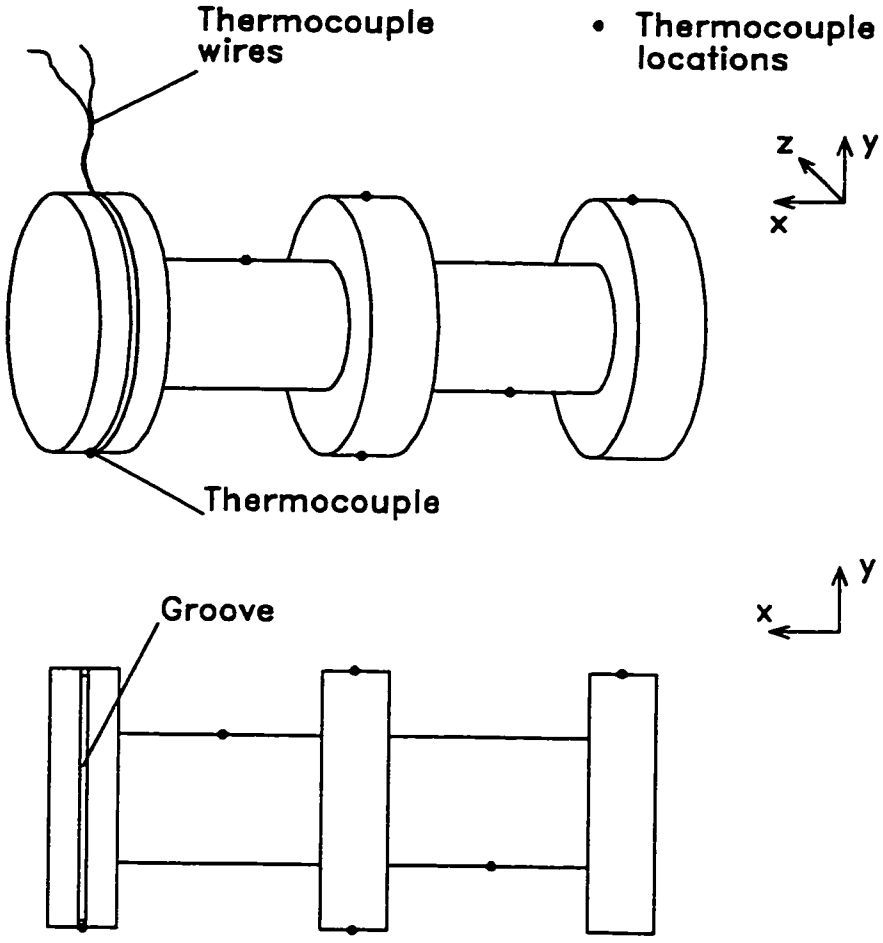

Figure 3.1: Thermocouple Installation.

3.3 Measurement of Radiative Heat Transfer

3.3.1 Description of experiment

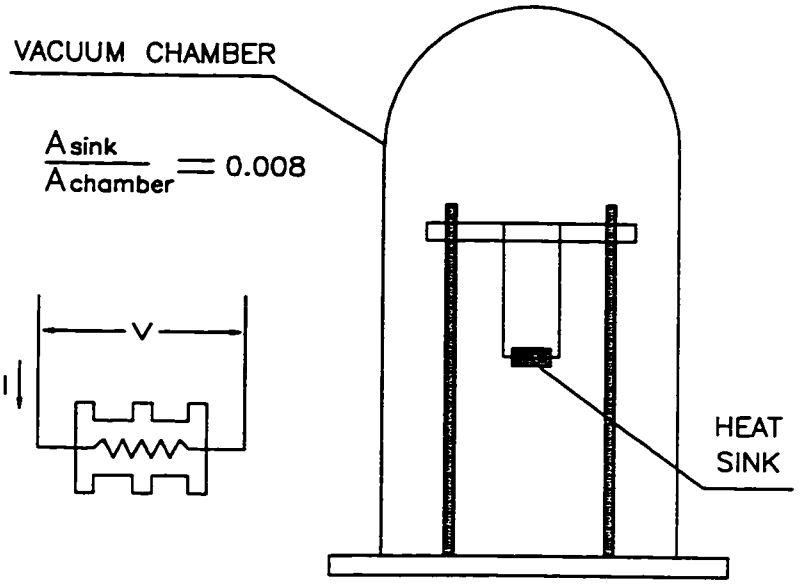

Figure 3.2: Measurement of Radiative Heat Transfer.

As shown in Fig. 3.2, the heat sink was placed in a vacuum chamber, which was made of steel, with the inner diameter of 445 *mm* and the height of 760 *mm*. A steady DC voltage was introduced to the heater embedded in the heat sink. The pressure of the chamber was kept at 10^{-6} torr, so that natural convection and gaseous conduction heat transfer was minimized. The applied heat was then dissipated only by radiation to the surroundings. There was heat conduction along the power leads and thermocouple wires, but in fact, this heat loss conducted through power leads and thermocouple wires was also dissipated by radiation from the wire surfaces (Appendix B). Therefore the measured radiation loss consisted of two parts: the major portion was the radiation loss from the heat sink surface, and the minor portion was the radiation loss from the power leads and the thermocouple

wire surfaces. The radiation equation for the heat sink is derived as follows. In order to combine the heat sink radiation and the wire radiation into one formula, the wire radiation part is converted to be based on the total surface area of the heat sink A and the wire base temperature T_S.

$$\begin{aligned} Q_R &= V \cdot I \\ &= Q_{HSR} + Q_{WR} \\ &= \mathcal{F}_1 A\sigma(T_S^4 - T_w^4) + Q_{WR} \\ &= \mathcal{F}_1 A\sigma(T_S^4 - T_w^4) + \frac{Q_{WR}}{A\sigma(T_S^4 - T_w^4)} A\sigma(T_S^4 - T_w^4) \\ &= \mathcal{F}_1 A\sigma(T_S^4 - T_w^4) + \overline{\mathcal{F}}_2 A\sigma(T_S^4 - T_w^4) \\ &= (\mathcal{F}_1 + \overline{\mathcal{F}}_2) A\sigma(T_S^4 - T_w^4) \\ &= \mathcal{F} A\sigma(T_S^4 - T_w^4) \end{aligned} \tag{3.1}$$

where Q_R stands for the total radiation loss, Q_{HSR} for the heat sink radiation loss and Q_{WR} for the heat loss by radiation from the wire surface. V and I are the voltage and current of the heaters, $\mathcal{F}_1$ is the exchange factor of the heat sink, $\overline{\mathcal{F}}_2$ is the equivalent exchange factor for the wire radiation loss, $\mathcal{F}$ is the exchange factor accounting for both the heat sink radiation and wire surface radiation losses, A is the total surface area of the heat sink, T_S is the temperature of the heat sink, and T_w is the temperature of the chamber wall.

Therefore Eq. (3.1) is actually for the total radiation heat transfer which accounts for both the heat sink radiation loss as well as the power leads and thermocouple wire radiation loss. By means of a fitting technique, the correlation of Q_R versus $(T_S^4 - T_w^4)$ was obtained, which afterward was used to decouple radiation loss from the natural convection heat transfer of interest.

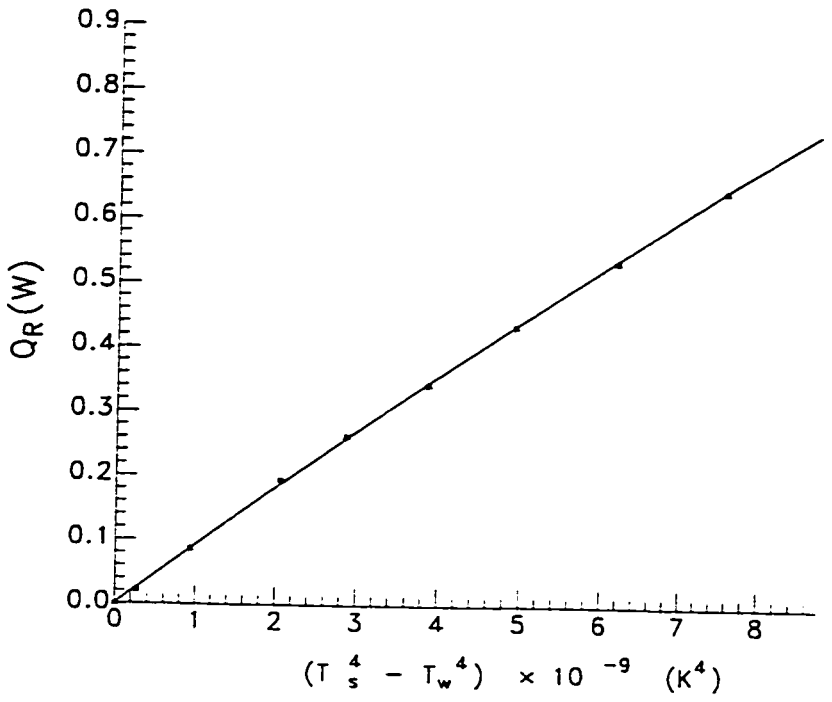

Figure 3.3: Radiative Heat Loss for Heat Sink A.

Figure 3.3 shows the correlation curve for heat sink A as an example.

One of the advantages of this approach is that it reduces the errors of experimental data. In some other experimental methods, the emissivity of the heat sink is determined first using the same results as described above. Then the emissivity is used to calculate the radiation loss in convection measurement. In the process because the emissivity is taken as a constant, it will bring in more deviations than the approach used in this study.

3.3.2 Experimental set-up

The apparatus used in the experiment is as follows:

- vacuum chamber,
- thermocouple board,
- Sciemetric Instruments model 321 data logger,

- Personal Computer,

- DC power supply,

- shunt resistor,

- mechanical vacuum pump,

- diffusion pump.

The test heat sink was suspended in the vacuum chamber. The thermocouple wires were connected to the thermocouple board and the embedded heater was connected to an electrical connector. The thermocouple board and the electrical connector were linked through the base plate of the vacuum chamber to a Scientific Instruments data logger and DC power supply, respectively. A standard resistor with a value of 0.1 ohm was added in series to the heater-power supply circuit. It was used to measure the electrical current passing through the heater. Having this current and the voltage across the heater, the input power can be readily calculated.

3.3.3 Experimental procedure

After suspending the test heat sink inside the vacuum chamber and connecting the thermocouple wires and power leads to the thermocouple board and the electrical connector, the vacuum chamber was sealed; then the vacuum pump was started. When the pressure inside the vacuum chamber dropped below 10^{-6} *torr*, the power supply was turned on and set at a constant voltage. At each temperature level, the voltage was maintained at a fixed value for 24 hours allowing the heat sink temperature to reach steady state. Then the values of the heat sink temperature, the voltage and current of the heater were recorded. The maximum temperature difference between the thermocouples on the surface of the heat sink was less than 0.2 K with $\Delta T = 50\ K$, or less than 0.4% of the temperature excess of the heat sink. As a result the heat sink was assumed to be isothermal. The voltage and

current were measured using a Hewlett Packard multimeter 3466A.

Because the data were taken at the same time each day, the room temperature fluctuations were very small. In fact, the temperature variation each day (24 hours) is about 3 degrees. Assume the temperature variation followed a curve of $\sin\tau$ (τ is time), the largest temperature variation rate with respect to time is about

$$\frac{dT_S}{d\tau} = \frac{3K}{8\ hours} = 1.04 \times 10^{-4}\ \ K/s$$

The heat capacity of the heat sink, e.g. heat sink A. is 117.8 J/K. and hence the heat absorbed by the heat sink due to $dT_S/d\tau$ caused by the ambient temperature variation will be

$$C^* \frac{dT_S}{d\tau} = 0.012\ \ (W)$$

This portion of the heat was not included in the radiation correlation mentioned above, and is taken as one of the uncertainties in the radiation measurements. But it is only a small portion of the radiation rate. For example. the radiation rate of heat sink A is 0.6 (W) for $\Delta T = 50\ K$, so the heat absorbed by the heat sink only accounted for 2% of the radiation rate.

The heat sink temperature rise $(T_S - T_w)$ ranged from 20 K to 90 K, and the data were taken at six temperature levels. With these data, a correlation of Q_R versus $(T_S^4 - T_w^4)$ was obtained using a fitting technique, as shown in Fig. 3.3.

The uncertainty analysis in Appendix C shows that the uncertainty of Q_R predicted by this correlation is $\pm 2.8\%$.

3.4 Measurement of Natural Convection Heat Transfer

3.4.1 Description of experiment

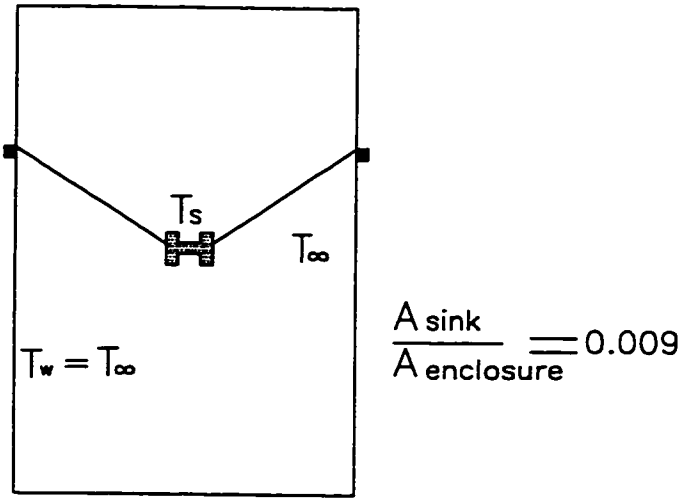

Figure 3.4: Measurement of Natural Convection Heat Transfer.

In this experiment, as shown in Fig. 3.4, the heat sink was supported by synthetic fiber lines in a large enclosure with small openings to the atmosphere. The enclosure was made of laminated wood coated by white paint, and with the length of 460 mm, the width of 305 mm and the height of 600 mm. A steady DC power was supplied to the heater inside the heat sink. In this case, the applied heat was carried away by convection and radiation from the heat sink surface, the power leads surface and the thermocouple wire surface. The energy balance can be expressed as

$$I \cdot V = Q_{Conv} + Q_R + \Delta Q_{WIR} \tag{3.2}$$

where I and V are the current and voltage of the heater; Q_{Conv} is the rate of convection heat transfer from the heat sink; Q_R is the radiation loss calculated

using the correlation obtained in the radiation loss measurement which accounts for radiation loss from all surfaces of the heat sink, the power leads and thermocouple: ΔQ_{WIR} is the additional wire heat loss due to the natural convection on the power leads and the thermocouple wire surfaces.

Because of the natural convection on the wire surfaces, the wire heat loss from the power leads and the thermocouple wires was enhanced when compared to the wire heat loss in the radiation measurement. The increment, ΔQ_{WIR}, can be estimated using the procedure developed in Appendix B. The convection heat transfer rate therefore was obtained by

$$Q_{Conv} = I \cdot V - Q_R - \Delta Q_{WIR} \tag{3.3}$$

Although the radiation measurement and the convection measurement were carried out in two different enclosures, whose surface emissivities may be different from each other, the correlation obtained in the radiation measurement still can be applied to the convection measurement to calculate the radiation loss Q_R. The reason is given as follows.

For a small object situated in the center of a large enclosure, if the surface of the enclosure is isothermal and $A_1/A_2 \approx 0$, where A_1 is the surface area of the object and A_2 is the surface area of the enclosure, then the following equation will be valid unless the emissivity of the enclosure is very small (Incropera and DeWitt 1990):

$$Q_{R1-2} = \bar{\epsilon}_1 A_1 \sigma (T_1^4 - T_2^4) \tag{3.4}$$

where Q_{R1-2} is the radiation heat flow rate from the object to the enclosure, $\bar{\epsilon}_1$ is the effective emissivity of the object, T_1 and T_2 are temperatures of the object surface and the enclosure surface respectively. Equation (3.4) shows that in this case the radiation heat transfer rate from the object to the enclosure is independent

of the emissivity and the area of the enclosure surface; it is determined only by the emissivity, surface area and geometry of the object itself, and the two temperatures.

In the present experiments, both radiation and convection measurements met the conditions stated above, therefore the correlation obtained in the radiation measurement can be used in the convection measurement to decouple the natural convection heat transfer from the radiation loss, regardless of the difference between the two emissivities of the enclosure surfaces. In the present experiments $A_1/A_2 \approx 0.01$, in this case the error resulted from Eq. (3.4) is less than 1%.

3.4.2 Experimental set-up

The experimental equipment used for convection measurement consists of

- natural convection enclosure
- Personal Computer
- *Fluke Helios I Computer Front End* data logger
- DC power supply ($0 \sim 100$ volt)
- shunt resistor

Three thermocouples were used to measure the ambient temperature. The extension wire from all the thermocouples were connected to the *Fluke Helios I Computer Front End* data logger, which is an acquisition and control subsystem and can be used with any kind of Personal Computer. The data logger is a medium speed (scanning 50 channels per second), accurate measurement control system. It is suitable for the present experiment because the temperatures were measured at steady state and hence the medium scanning speed was sufficient. The shunt resistor connected in series with the heater was used to measure the current passing through the heater. Both the voltage and current of the heater were measured and recorded by the data logger.

3.4.3 Experimental procedure

After the heat sink had been installed in the natural convection enclosure, a measurement program was started from the Personal Computer which automatically conducted the following procedure. At each preset power level, the power supplied to the heater was fixed, until the steady state criteria were met and then the data logger measured the voltage and current of the heater and the temperatures of all thermocouples. Sixty sets of readings were taken and averaged to reduce the random errors due to analogue-digital conversion. Since the maximum temperature difference between the heat sink thermocouples was less than 0.25 K, including thermocouple measuring errors, with $(T_S - T_\infty) = 50\ K$ the heat sink was also considered as isothermal.

The steady state criteria in the convection measurement were:

i) the minimum "waiting time" was 2×10^4 seconds, and

ii) the maximum absolute difference between a temperature reading and the next one in time steps was less than 0.05 K, and

iii) the maximum percentage difference was less than 0.05% (in Celsius scale).

The uncertainty analysis in Appendix C shows that the uncertainty of the rate for natural convection heat transfer, Q_{Conv}, is $\pm 0.5\%$.

3.5 Data Reduction

The natural convection heat transfer rate is given by Eq. (3.3):

$$Q_{Conv} = I \cdot V - Q_R - \Delta Q_{WIR}$$

where

Q_{Conv}	—	rate of convection heat transfer, W
I	—	current of heater, Ampere
V	—	voltage of heater, Volt
Q_R	—	rate of radiation loss, W
ΔQ_{WIR}	—	additional wire heat loss, W

The radiation loss, Q_R, is calculated using the correlations obtained in the radiation experiments. The additional wire heat loss, ΔQ_{WIR}, is found by following the procedure in Appendix B.

The Rayleigh number was obtained using Eq. (1.2):

$$Ra_b^* = \frac{g\beta\,\Delta T\,b^3}{\alpha\,\nu}\frac{b}{D}$$

where

g	—	gravitational acceleration, m/s^2
β	—	volumetric coefficient of thermal expansion, $1/K$
α	—	thermal diffusivity, m^2/s
ν	—	kinematic viscosity, m^2/s
ΔT	—	temperature difference, $\equiv T_S - T_\infty$, K
b	—	spacing between adjacent fins, m
D	—	fin outer diameter, m

where β is evaluated at T_∞ and all the other physical properties were evaluated at the film temperature, i.e. $T_f = (T_S + T_\infty)/2$ (Raithby and Hollands, 1985).

The uncertainty analysis in Appendix C for the experiment shows that for the typical temperature difference $\Delta T = 50\ K$, the uncertainty of Ra_b^* is 3.3% for $Ra_b^* \approx 2.6 \times 10^4$, and 5.1% for $Ra_b^* \approx 1.5$.

The Nusselt number is calculated using Eq. (1.1):

$$Nu_b = \frac{Q_{Conv}}{A_{HS}\,\Delta T}\frac{b}{k} \tag{3.5}$$

where

Q_{Conv}	—	rate of convection heat transfer, W
A_{HS}	—	surface area of heat sink, m^2
ΔT	—	temperature difference, $\equiv T_S - T_\infty$, K
b	—	spacing between adjacent fins, m
k	—	thermal conductivity, $W/m\,K$

Q_{Conv} is given by Eq. (3.3) and k is evaluated at the film temperature $T_f = (T_S + T_\infty)/2$.

The uncertainty analysis in Appendix C shows that the uncertainty of Nu_b is $\pm 1.3\%$ for $Nu_b \approx 6.9$ and $\pm 1.6\%$ for $Nu_b \approx 0.36$.

3.6 Verification of Experimental Method

Heat sink D, which has the spacing of 2 mm, was used to establish a confidence level in the experimental method. According to the narrow-channel criterion (Bejan 1993), which can be expressed approximately for the heat sink as follows.

$$Ra_b(b/D) \leq 1 \tag{3.6}$$

the channels between two adjacent fins of heat sink D are narrow and the buoyancy-induced flow between them is fully-developed flow.

The measurement result of heat flow rate Q_{Conv} for heat sink D is just 9.5% higher than that of its circumscribed cylinder whose heat flow rate is calculated using an established method (Jafarpur, 1992). According to the fully developed flow analysis, the channel flow between fins of heat sink D accounts for about 10% of the heat transfer of the circumscribed cylinder. It confirms that the measurement result for heat sink D is correct. Thus it is believed that the overall experimental method is reliable.

3.7 Experimental Results

The results of the experiments are plotted in Fig. 3.5, and given in Table 3.2 through Table 3.6. The five heat sinks were measured at the same conditions, i.e. at atmospheric pressure, the temperature difference between the heat sink and the ambient air ranging from 20 K to 80 K, and the ambient temperature being about 293 K. It can be seen from Fig. 3.10 that the results for the five heat sinks lie in different ranges of Ra_b^*, because they have different values of b/D (note: $Ra_b^* = Ra_D b^4/D^4$).

In the range of $Ra_b^* > 4\times10^3$ the thin boundary layer heat transfer is dominant, so the experimental results of heat sink A lie along a straight line of slope 1/4. For $Ra_b^* = 10^0 \sim 10^3$, the introduction of channeling effects results in an increase in the slope of the data for heat sinks B, C and D. For $Ra_b^* < 10^{-1}$, the thin boundary layer heat transfer from the outer surface (the fin rim surfaces and the end surfaces) becomes dominant, and the slope of the experimental data for heat sink E returns to 1/4 again.

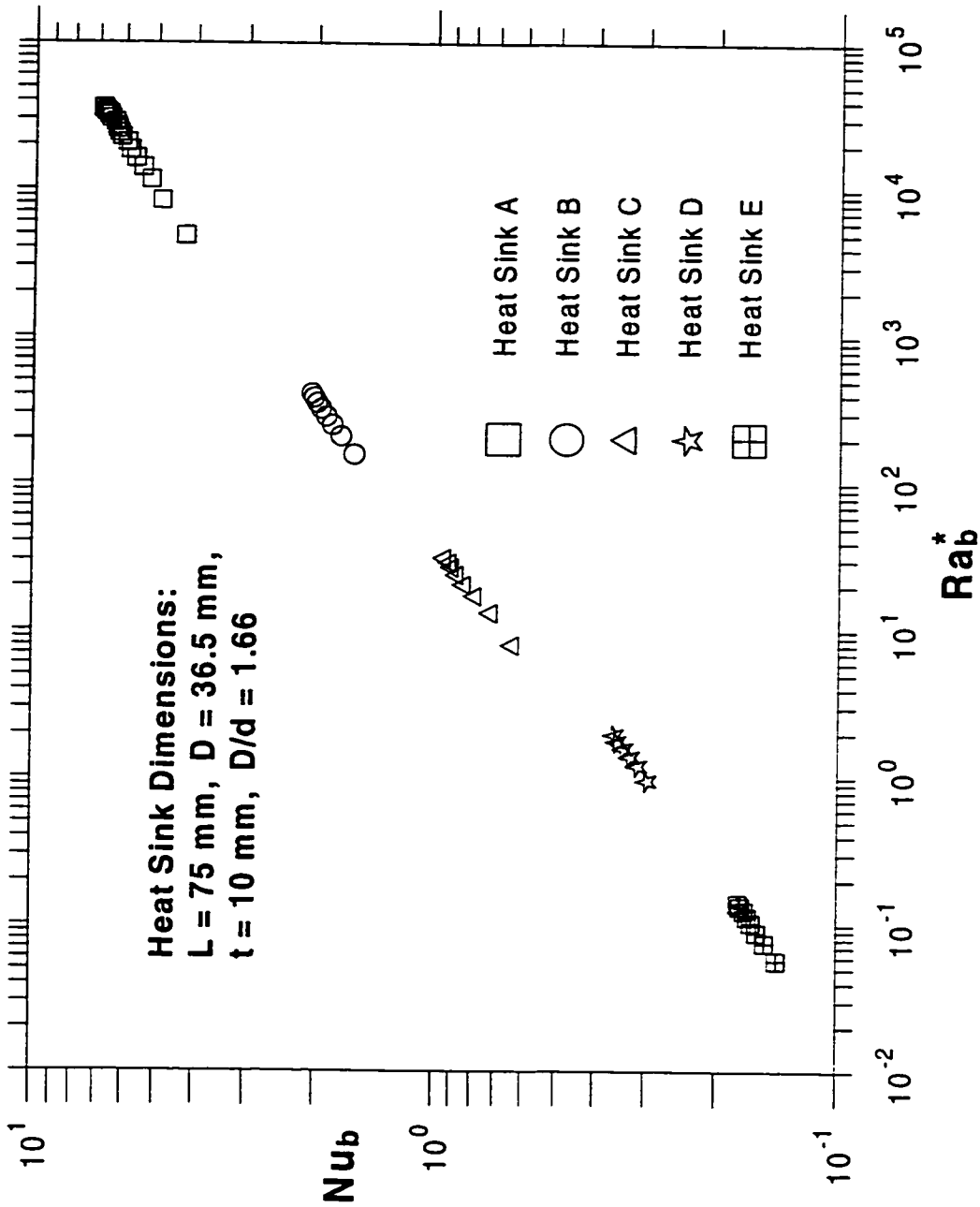

Figure 3.5: Present Experimental Results.

Table 3.2: Experimental Results — Heat Sink A.

$Ra_b(b/D)$	Nu_b	$Ra_b(b/D)$	Nu_b
4874.6	4.27	25497.8	6.30
8420.9	4.89	26819.4	6.33
11590.9	5.22	28566.0	6.41
14034.0	5.47	30241.8	6.56
16282.5	5.69	31610.8	6.63
18530.4	5.88	32496.2	6.65
20794.5	5.97	33657.3	6.72
22607.5	6.18	34835.2	6.82
24052.4	6.25	35912.8	6.87

Table 3.3: Experimental Results — Heat Sink B.

$Ra_b(b/D)$	Nu_b
158.9	1.60
210.5	1.73
251.9	1.82
287.2	1.88
322.6	1.94
355.0	1.99
385.5	2.03
408.6	2.05

Table 3.4: Experimental Results — Heat Sink C.

$Ra_b(b/D)$	Nu_b
8.03	0.634
13.19	0.718
17.18	0.785
20.56	0.838
24.05	0.874
27.09	0.899
28.95	0.912
31.12	0.938

Table 3.5: Experimental Results — Heat Sink D.

$Ra_b(b/D)$	Nu_b
0.949	0.296
1.204	0.313
1.390	0.325
1.590	0.338
1.779	0.352
1.967	0.357

Table 3.6: Experimental Results — Heat Sink E.

$Ra_b(b/D)$	Nu_b
0.057	0.140
0.075	0.150
0.089	0.157
0.103	0.162
0.114	0.166
0.125	0.169
0.135	0.173
0.141	0.175

3.8 Summary

In this chapter the experimental method used in this study, the test heat sinks, the experimental set-up and the experimental procedure are described.

The radiation losses were measured using the steady state heat balance method in a vacuum chamber. The correlations of the radiation losses were used to decouple the convection heat transfer from the radiative heat flow rate.

The experimental results for the five heat sinks are also presented.

In the next chapter, models for the heat sinks will be developed.

Chapter 4

Models for Annular-Fin Heat Sinks

A dimensional analysis for annular-fin heat sinks is given in the following section. The external natural convection solution used in this study is briefly reviewed in Section 4.2. In Section 4.3, the model development, model simplification and model prediction trends are presented. In Section 4.4, a radiative heat transfer model for the heat sinks is developed. Finally, the non-isothermal fins are considered in Section 4.5.

4.1 Dimensional Analysis

Assume steady state natural convection within a Newtonian fluid of constant properties, except density which causes the buoyancy force (the Boussinesq approximation, Incropera and Dewitt, 1990). Also assume that the fluid is incompressible. Drop the terms which have only minor influence in the process. With reference to Fig. 4.1, the simplified equations of motion for steady state natural convection problems are as follows (Raithby and Hollands, 1985) with the gravity force acting in the negative z direction:

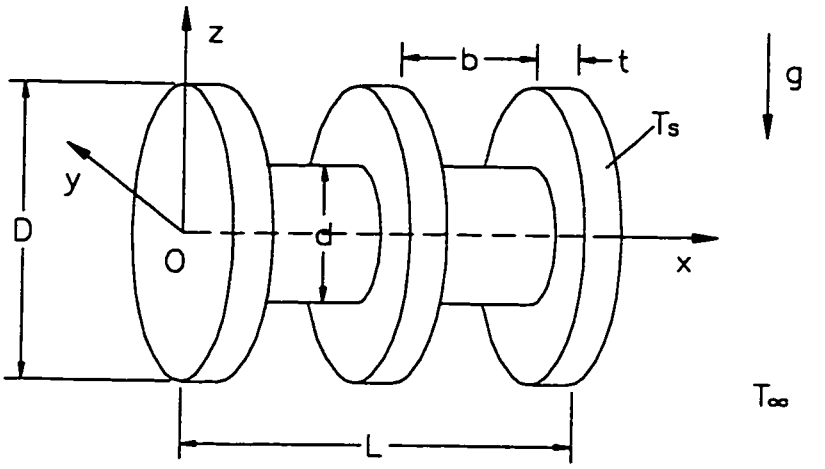

Figure 4.1: Coordinates of Heat Sink.

Continuity equation:

$$\frac{\partial u^*}{\partial x^*} + \frac{\partial v^*}{\partial y^*} + \frac{\partial w^*}{\partial z^*} = 0 \tag{4.1}$$

Momentum equations:

$$u^*\frac{\partial u^*}{\partial x^*} + v^*\frac{\partial u^*}{\partial y^*} + w^*\frac{\partial u^*}{\partial z^*} = -\frac{\partial P_d^*}{\partial x^*} + \sqrt{Pr\frac{(1+Pr)}{Ra_{\mathcal{L}}}}\left(\frac{\partial^2 u^*}{\partial x^{*2}} + \frac{\partial^2 u^*}{\partial y^{*2}} + \frac{\partial^2 u^*}{\partial z^{*2}}\right) \tag{4.2}$$

$$u^*\frac{\partial v^*}{\partial x^*} + v^*\frac{\partial v^*}{\partial y^*} + w^*\frac{\partial v^*}{\partial z^*} = -\frac{\partial P_d^*}{\partial y^*} + \sqrt{Pr\frac{(1+Pr)}{Ra_{\mathcal{L}}}}\left(\frac{\partial^2 v^*}{\partial x^{*2}} + \frac{\partial^2 v^*}{\partial y^{*2}} + \frac{\partial^2 v^*}{\partial z^{*2}}\right) \tag{4.3}$$

$$u^*\frac{\partial w^*}{\partial x^*} + v^*\frac{\partial w^*}{\partial y^*} + w^*\frac{\partial w^*}{\partial z^*} = -\frac{\partial P_d^*}{\partial z^*} + \sqrt{Pr\frac{(1+Pr)}{Ra_{\mathcal{L}}}}\left(\frac{\partial^2 w^*}{\partial x^{*2}} + \frac{\partial^2 w^*}{\partial y^{*2}} + \frac{\partial^2 w^*}{\partial z^{*2}}\right) + (1+Pr)\theta^* \tag{4.4}$$

Energy equation:

$$u^*\frac{\partial \theta^*}{\partial x^*} + v^*\frac{\partial \theta^*}{\partial y^*} + w^*\frac{\partial \theta^*}{\partial z^*} = \sqrt{\frac{(1+Pr)}{Ra_{\mathcal{L}}\,Pr}}\left(\frac{\partial^2 \theta^*}{\partial x^{*2}} + \frac{\partial^2 \theta^*}{\partial y^{*2}} + \frac{\partial^2 \theta^*}{\partial z^{*2}}\right) \tag{4.5}$$

where $Ra_{\mathcal{L}} = g\beta\Delta T\mathcal{L}^3/\nu\alpha$, and the dimensionless terms are defined with respect to an arbitrary characteristic length $\mathcal{L}$ as

$$x^* = x/\mathcal{L}, \quad y^* = y/\mathcal{L}, \quad z^* = z/\mathcal{L},$$

$$v_0 = \sqrt{g\,\beta_\infty\,\Delta T\,\mathcal{L}/(1+\nu_0/\alpha_0)}$$

$$u^* = u/v_0, \quad v^* = v/v_0, \quad w^* = w/v_0$$

$$\theta^* = \frac{T-T_\infty}{T_S-T_\infty}, \quad P_d^* = \frac{P_d}{\rho_0 v_0^2/2}$$

where ρ_0, ν_0, α_0 are the values evaluated at $(T_S+T_\infty)/2$. P_d is the pressure component associated with dynamics of flow.

The boundary conditions are:

At the surface of the heat sink,

$$u^* = v^* = w^* = 0, \quad \theta^* = 1 \tag{4.6}$$

Specifically,

i) at the two end surfaces:

$x^* = 0$, and $x^* = L/\mathcal{L}$, and $0 \le \sqrt{y^{*2}+z^{*2}} \le D/\mathcal{L}$; and

ii) at the internal lateral surfaces (left side):

$x^* = t/\mathcal{L} + i(b+t)/\mathcal{L}$, $(i = 0, 1, \cdots N_f - 2)$, and $d/\mathcal{L} \le \sqrt{y^{*2}+z^{*2}} \le D/\mathcal{L}$, and

iii) at the internal lateral surfaces (right side):

$x^* = i(b+t)/\mathcal{L}$, $(i = 1, 2, \cdots N_f - 1)$, and $d/\mathcal{L} \le \sqrt{y^{*2}+z^{*2}} \le D/\mathcal{L}$; and

iv) at the rim of the fins:

$i(b+t)/\mathcal{L} \le x^* \le t/\mathcal{L}+i(b+t)/\mathcal{L}$, $(i = 0, 1, \cdots N_f-1)$, and $\sqrt{y^{*2}+z^{*2}} = D/\mathcal{L}$; and

v) at the support cylinder surfaces:

$t/\mathcal{L}+i(b+t)/\mathcal{L} \leq x^* \leq (i+1)(b+t)/\mathcal{L}$, $(i = 0, 1, \cdots N_f-2)$, and $\sqrt{y^{*2}+z^{*2}} = d/\mathcal{L}$.

$$u^* = v^* = w^* = 0, \quad \theta^* = 1$$

where the fin number N_f is a function of b, t and L or

$$N_f = f(b/\mathcal{L},\ t/\mathcal{L},\ L/\mathcal{L})$$

At a large distance from the heat sink,

$$u^* = v^* = w^* = \theta^* = 0 \tag{4.7}$$

If the enclosure surrounding the heat sink is large enough, it has no influence on the natural convection of the heat sink.

From the simplified equations of motion and the boundary conditions, the temperature field has the following dependence:

$$\theta^* = \theta^*(x^*,\ y^*,\ z^*,\ Ra_{\mathcal{L}},\ Pr,\ b/\mathcal{L},\ D/\mathcal{L},\ d/\mathcal{L},\ t/\mathcal{L},\ L/\mathcal{L}) \tag{4.8}$$

Because the total heat flow rate is

$$\begin{aligned} Q &= \iint_{A_{HS}} -k\frac{\partial T}{\partial n} dA \\ &= -k\frac{T_S - T_\infty}{\mathcal{L}} \iint_{A_{HS}} \left(\frac{\partial \theta^*}{\partial n^*}\right) dA \end{aligned} \tag{4.9}$$

where $n^* = n/\mathcal{L}$. And hence the average Nusselt number is

$$\begin{aligned} Nu_{\mathcal{L}} &= \frac{Q\,\mathcal{L}}{A_{HS}\,k\,(T_S - T_\infty)} \\ &= \frac{1}{A_{HS}} \iint_{A_{HS}} \left(-\frac{\partial \theta^*}{\partial n^*}\right) dA \end{aligned} \tag{4.10}$$

Thus the average Nusselt number $Nu_{\mathcal{L}}$ has the following functional form:

$$Nu_{\mathcal{L}} = f(Ra_{\mathcal{L}},\ Pr,\ b/\mathcal{L},\ D/\mathcal{L},\ d/\mathcal{L},\ t/\mathcal{L},\ L/\mathcal{L}) \tag{4.11}$$

Therefore the Nusselt number is a function of seven variables.

Case 1:

If the values of $Pr,\ b/\mathcal{L},\ D/\mathcal{L},\ d/\mathcal{L},\ t/\mathcal{L},\ L/\mathcal{L}$ are fixed, then

$$Nu_{\mathcal{L}} = f_1(Ra_{\mathcal{L}}) \tag{4.12}$$

Taking D as the characteristic length, we have the functional relationship:

$$Nu_D = f_1(Ra_D) \tag{4.13}$$

Multiplying both sides of the relation by b/D gives

$$Nu_b = f_1(Ra_D)\, b/D$$

Because b/D is constant, letting $f_2() = b/D\ f_1()$, the above functional relation becomes

$$Nu_b = f_2(Ra_D)$$

or, alternatively, with b/D held constant,

$$\begin{aligned} Nu_b &= f_3(Ra_D\, b^4/D^4) \\ &= f_3(Ra_b^*) \end{aligned} \tag{4.14}$$

The functional relation Eq. (4.14) means that for a group of geometrically similar heat sinks, i.e. heat sinks with identical values of b/D, d/D, t/D and L/D, if Pr is a constant, their measured results can be correlated by a single $Nu_b - Ra_b^*$ curve. The essence of this functional form is the relationship between

Nu_D and Ra_D, i.e. Eq. (4.13). For different geometric parameter values, e.g. different values of b/D, there will be different curves corresponding to the different parameter values. This was confirmed by the experimental results of Karagiozis (1991), although the rectangular fin arrays were used in his experiments instead of annular-fin heat sinks. In the experiments, Ra_b^* varied with air pressure, while all the geometric parameters were fixed in each case.

Case 2:

If the values of $Ra_{\mathcal{L}}$, Pr, $D/\mathcal{L}$, $d/\mathcal{L}$, $t/\mathcal{L}$, $L/\mathcal{L}$ are fixed, Eq. (4.11) becomes

$$Nu_{\mathcal{L}} = F(b/\mathcal{L}) \tag{4.15}$$

Taking D as the characteristic length, we have another functional relationship:

$$Nu_D = F(b/D) \tag{4.16}$$

Multiplying both sides of the relation by b/D yields

$$Nu_D \frac{b}{D} = F(b/D)\frac{b}{D}$$

or

$$Nu_b = F_1(b/D)$$

From the above functional relation, the following functional relation can also be established:

$$Nu_b = F_2(b^4/D^4)$$

or, alternatively, with Ra_D held constant,

$$\begin{aligned} Nu_b &= F_3(Ra_D\, b^4/D^4) \\ &= F_3(Ra_b^*) \end{aligned} \tag{4.17}$$

The functional relation Eq. (4.17) means that for a group of heat sinks whose values of d/D, t/D, L/D are identical, but the values of b/D are different, and if the values of Ra_D are fixed, the measured results can be correlated by a single $Nu_b - Ra_b^*$ curve. The essence of this functional form is the relationship between Nu_D and b/D, i.e. Eq. (4.16).

In this case, for different values of Ra_D, there should be different curves corresponding to the values of Ra_D. But as shown by the present experimental results in Fig. 3.5 and the previous experiments (Elenbaas, 1942; Edwards and Chaddock, 1963; Jones and Nwizu, 1969; Tsubouchi and Masuda, 1970), when the variation of Ra_D is limited (e.g. $Ra_D = 0.15 \times 10^5 \sim 2.5 \times 10^5$ in the present experiment), it is possible to use a single $Nu_b - Ra_b^*$ curve to represent the different curves corresponding to different values of Ra_D with only small deviations. For the present experiments with the temperature difference $(T_S - T_\infty)$ ranging from 20 K to 80 K, or Ra_D ranging from 9.1×10^4 to 2.5×10^5, the deviations are within 3.7%.

In most previous experiments, both Ra_D and b/D were varied, but the variation of Ra_D is limited to a narrow range, say a factor of 20, the wide range of Ra_b^* was achieved through variation of b/D. Therefore, in the following chapter, the comparisons with these previous correlations should be made in such a way that Ra_D is fixed at an average value and Ra_b^* varies with b/D. In addition, the values of d/D, t/D, L/D and the end surface condition should also be taken into consideration.

4.2 External Natural Convection Solutions

As mentioned in Chapter 2, Yovanovich (1987b,c) and Lee et al. (1991) used a characteristic length based on the surface area, $\sqrt{A}$, to recast the existing boundary layer solutions for laminar natural convection (Acrivos, 1960; Stewart, 1971;

Raithby and Hollands, 1975, 1978) and obtained a new expression of the solutions for isothermal, three dimensional bodies. When combined with the diffusive limit, it gives the total heat transfer in the following form:

$$Nu_{\sqrt{A}} = Nu^0_{\sqrt{A}} + F(Pr)\, G_{\sqrt{A}}\, Ra^{1/4}_{\sqrt{A}} \tag{4.18}$$

The first term of the equation, $Nu^0_{\sqrt{A}}$, is the diffusive limit of the body, which accounts for the correction for the curvature effect of the boundary layers. The second term of the equation, $F(Pr)\, G_{\sqrt{A}}\, Ra^{1/4}_{\sqrt{A}}$, is the boundary layer solution for the total surface, where $F(Pr)$ is the approximate 'universal' Prandtl number function (Churchill and Churchill, 1975) defined as

$$F(Pr) = \frac{0.670}{\left[1 + (0.5/Pr)^{9/16}\right]^{4/9}} \tag{4.19}$$

The body-gravity function for two-dimensional or axisymmetric surfaces, $G_{\sqrt{A}}$, is obtained from

$$G_{\sqrt{A}} = \left[\frac{1}{A} \int\int_A \left(\frac{P(\theta)\sin\theta}{\sqrt{A}} \right)^{1/3} dA \right]^{3/4} \tag{4.20}$$

where A is the total area of the surface considered; $P(\theta)$ is the local perimeter of the axisymmetric body; and θ is the angle between the outward normal $\vec{n}$ and the gravity vector, $\vec{g}$.

For two dimensional surfaces as shown in Fig. 4.2, $P(\theta)$ is replaced by the width of the surface, B.

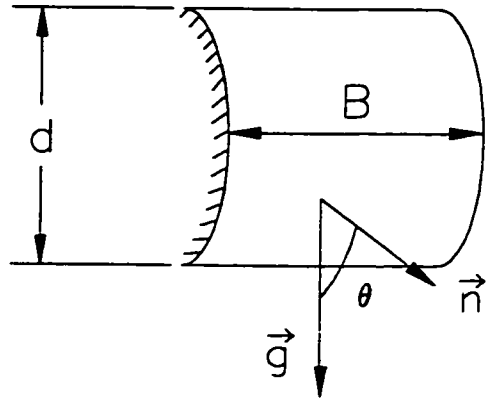

Figure 4.2: Half of Horizontal Circular Cylindrical Surface.

The overall body-gravity function for N component surfaces connected in parallel with respect to the flow stream can be obtained by (Lee et al., 1991):

$$G_{\sqrt{A}} = \sum_{i=1}^{N} G_{\sqrt{A_i}} \, (A_i/A)^{7/8} \tag{4.21}$$

where A_i refers to the component surface areas and A is the total surface area for the N component surfaces, which is given by

$$A = \sum_{i=1}^{N} A_i$$

The overall body-gravity function for component surfaces connected in series with respect to the flow stream can be obtained from (Lee et al., 1991):

$$G_{\sqrt{A}} = \left[\sum_{i=1}^{N} G_{\sqrt{A_i}}^{4/3} \, (A_i/A)^{7/6} \right]^{3/4} \tag{4.22}$$

Because of the introduction of the characteristic length $\sqrt{A}$, the body gravity function $G_{\sqrt{A}}$ is easy to obtain when dealing with relatively complex geometries. The entire surface of a body can be divided into component surfaces whose body gravity functions $G_{\sqrt{A_i}}$ are easy to calculate. After the body-gravity-functions of the component surfaces are obtained, they are combined to form the total $G_{\sqrt{A}}$ of

the body in an appropriate way using Eq. (4.21) or Eq. (4.22) or both of them. Because the body gravity function is insensitive to the changes in geometry and orientation of bodies (Lee et al., 1991), the above procedure should not introduce much deviation in the total body gravity function.

Based on the definitions of Nu_b and Ra_b^*, i.e. Eq. (1.1) and Eq. (1.2), in Chapter 1:

$$Nu_b = \frac{Q}{A\,\Delta T}\frac{b}{k}$$

and

$$Ra_b^* = \frac{g\beta\,\Delta T\,b^3}{\alpha\nu}\frac{b}{D}$$

the heat transfer, Eq. (4.18), can be transformed as follows:

Applying the second term of Eq. (4.18) to the surface of interest gives a thin boundary layer solution for the surface:

$$Nu^T_{\sqrt{A}} = F(Pr)\,G_{\sqrt{A}}\,Ra^{1/4}_{\sqrt{A}} \tag{4.23}$$

From the term of the RHS of Eq. (4.23), we have

$$\begin{aligned} F(Pr)\,G_{\sqrt{A}}\,Ra^{1/4}_{\sqrt{A}} &= F(Pr)\,G_{\sqrt{A}}\left[Ra_b^*\,\frac{D}{b}\left(\frac{\sqrt{A}}{b}\right)^3\right]^{1/4} \\ &= F(Pr)\,G_{\sqrt{A}}\,(Ra_b^*)^{1/4}\frac{D^{1/4}(\sqrt{A})^{3/4}}{b} \end{aligned}$$

Multiplying both sides of Eq. (4.23) by $(b/\sqrt{A})$ yields

$$\begin{aligned} Nu_b^T &= F(Pr)\,G_{\sqrt{A}}\,(Ra_b^*)^{1/4}\frac{D^{1/4}(\sqrt{A})^{3/4}}{b}\frac{b}{\sqrt{A}} \\ &= F(Pr)\,G_{\sqrt{A}}\left(\frac{D}{\sqrt{A}}\right)^{1/4}(Ra_b^*)^{1/4} \end{aligned} \tag{4.24}$$

This equation will be used to calculate the boundary layer heat transfer for the heat sink in the following section.

4.3 Model Development

As shown in Fig. 4.3, a heat sink surface consists of four types of component surfaces, i.e. lateral fin surfaces, support cylinder surfaces, fin rim surfaces and end surfaces. The combination of all lateral fin surfaces and support cylinder surfaces is referred to as the inner surface, while fin rim surfaces and the end surfaces are considered as the outer surface.

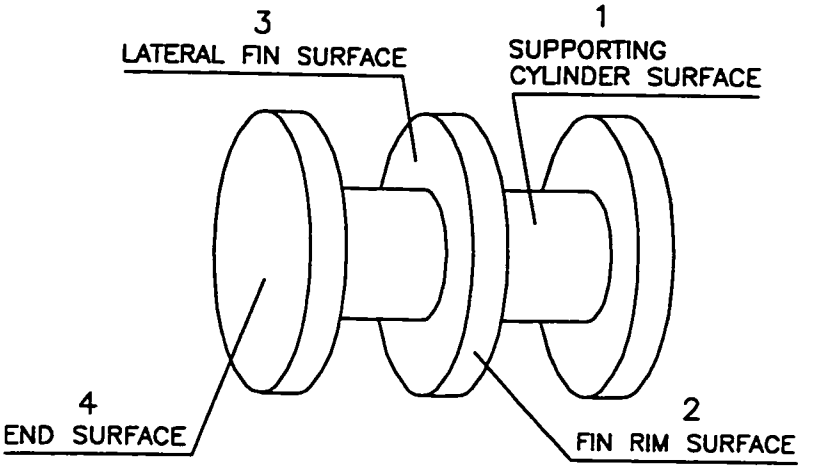

Figure 4.3: Components of Heat Sink Surface.

When the heat sink Rayleigh number Ra_b^* is large, the boundary layers which develop along the vertical surfaces of adjacent fins do not interact. Although there is interference between the boundary layers of the vertical fin surface and the support cylinder surface, the effect is relatively small. This is the thin boundary layer regime. On the other hand, when Ra_b^* is small, the buoyancy-induced flow becomes fully-developed between adjacent fins. This is the fully developed flow regime. Between the thin boundary layer regime and the fully developed flow regime, there is the transition regime.

Therefore the inner surface may experience three modes of heat transfer, i.e. thin boundary layer convection at high Ra_b^*, fully-developed flow at low Ra_b^* and

the transitional region. At the same time, over the outer surface of the heat sink, there is only one mode of heat transfer for the entire range of Ra_b^*, i.e. external natural convection. By distinguishing between the inner and outer surfaces, the heat transfer mechanisms which dominate in each region of the heat sink surface can be more easily applied. An overall rate of heat transfer can be determined by combining the heat transfer from both the inner and outer surfaces.

Based on the consideration above, the model will have the following form:

$$Nu_b = Nu_b^0 + Nu_{b,OUT} + Nu_{b,IN} \tag{4.25}$$

where

Nu_b — Nusselt number of the heat sink

Nu_b^0 — contribution by the diffusive limit

$Nu_{b,OUT}$ — contribution by the convection of the outer surface

$Nu_{b,IN}$ — contribution by the convection of the inner surface

for the inner surfaces,

$$Nu_{b,IN} = f(Nu_{b,A_{IN-T}},\ Nu_{b,A_{IN-FD}}) \tag{4.26}$$

where

$Nu_{b,A_{IN-T}}$ — Nusselt number of the inner surface in thin boundary layer regime

$Nu_{b,A_{IN-FD}}$ — Nusselt number of the inner surface in fully developed regime

In the following subsections each of the above terms will be derived.

4.3.1 Model for Inner Surface

There are two limiting solutions for the inner surface: the solution for thin boundary layer flow, which is valid at high Ra_b^*, and the solution for fully developed flow,

which is valid at low Ra_b^*. Blending the two limiting solutions provides the model for the inner surface over the entire range of Ra_b^*.

Thin Boundary Layer Flow Regime.

For $Ra_b^* > 10^3$, the boundary layers of two adjacent fins do not interact, and hence the average heat transfer over the inner surface will be close to that of the external convection with the same surface area. In this circumstance, the above external natural convection solutions can be directly applied to the inner surface.

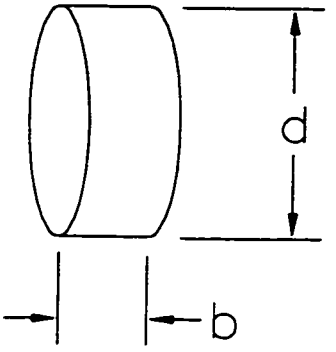

Figure 4.4: Circular Cylindrical Surface.

The surface component 1 in Fig. 4.3 is a cylindrical surface. If the diameter of the cylindrical surface is d and its length is b as shown in Fig. 4.4, the body gravity function for the cylindrical surface, Eq. (4.20), can be simplified as

$$G_{\sqrt{A}} = 0.891 \left(\frac{b}{d}\right)^{1/8} \tag{4.27}$$

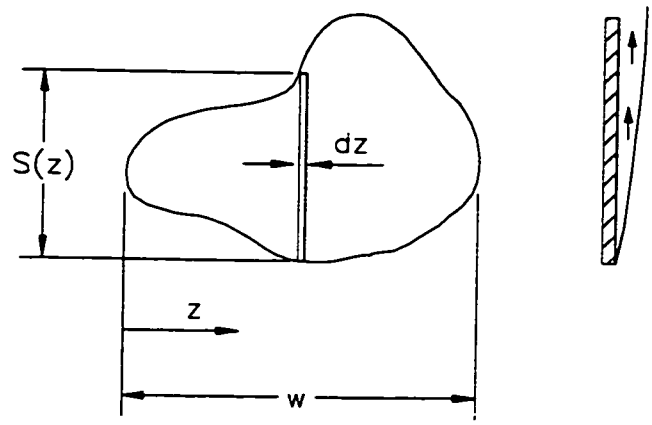

Figure 4.5: Vertical Planar Surface.

The surface component 3 in Fig. 4.3 is a vertical planar surface. For this kind of surfaces as shown in Fig. 4.5, Eq. (4.20) becomes

$$G_{\sqrt{A}} = \frac{1}{A^{7/8}} \int_0^W S(z)^{3/4}\, dz \tag{4.28}$$

Thus the body gravity functions of the 2 types of component surfaces of the inner surface can be calculated by Eq. (4.27) and Eq. (4.28) respectively. In order to take into account the effect of the plume rising from the support cylinder upon the lateral fin surface heat transfer, the rate of heat transfer from the area affected by the plume will be reduced by half. To make the calculation easier, the area P in Fig. 4.6 is used to represent the area affected by plume. As shown in Fig. 4.6 (b), the area 1 is a portion of the plume affected area, and is outside the area P. But it is approximately represented by the area 2 which is inside the area P. It is assumed that the average temperature difference between the fin surface of area P and the plume is $(T_S - T_\infty)/2$. Therefore the heat transfer from the area P is reduced by half compared with that from the same area without the plume effect. The body gravity functions of the inner surface components are combined using Eq. (4.21) to give the body gravity function for the inner surface, $G_{\sqrt{A}_{IN}}$.

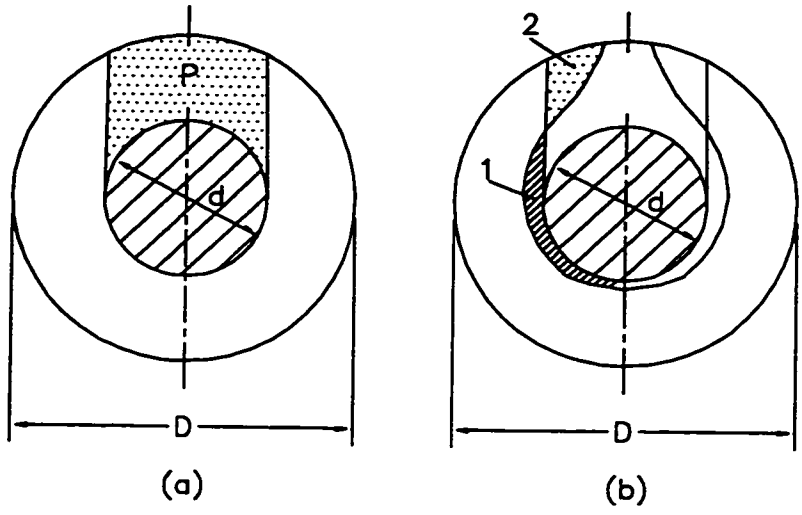

Figure 4.6: Area Affected by Cylinder Plume.

The Nusselt number for the inner surface in the thin boundary layer regime can be obtained using Eq. (4.24):

$$Nu_{b,A_{IN}-T} = F(Pr)\, G_{\sqrt{A_{IN}}}\, (D/\sqrt{A_{IN}})^{1/4}\, Ra_b^{*1/4} \tag{4.29}$$

Fully Developed Flow Regime.

Two adjacent fins of the heat sink form a "channel". In the fully developed regime (approximately $Ra_b^* < 1$, Bejan 1993) the heat transferred from the channel surface consists of two parts: i) the heat carried away by the channel flow, and ii) the heat conducted radially outward from the channel.

Heat transfer due to channel flow: As shown in Fig. 4.7, the channel air flow near the edge BC is assumed fully developed and in the direction straight up. Because it has passed a distance close to the fin diameter D except for a small portion near the lateral edge, based on the criterion of the fully developed regime $Ra_b^* < 1$ (Bejan 1993), the flow can be considered fully developed. The velocity

distribution in this region is (Bejan 1993)

$$v = \frac{g\beta\Delta T b^2}{8\nu}\left[1 - \left(\frac{x}{b/2}\right)^2\right] \tag{4.30}$$

where x is the coordinate parallel to the axis of the heat sink and with the origin at the center of the spacing.

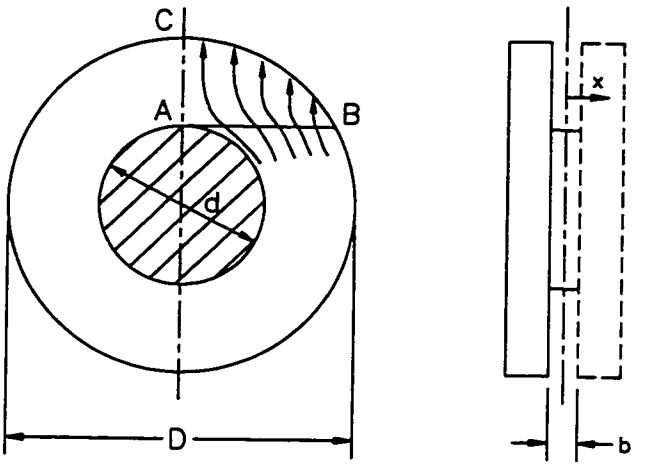

Figure 4.7: Narrow Channel Flow between Adjacent Fins.

The vertical flow rate per unit width in the direction of $\overline{AB}$ is

$$\dot{m}' = \int_{-b/2}^{b/2} \rho v \, dx = \frac{\rho g \beta \Delta T b^3}{12\nu} \tag{4.31}$$

Because the projected length of arc BC in the direction of gravity is AB, the mass flow rate for the "channel" is approximately

$$\dot{m} = \dot{m}' W \tag{4.32}$$

where

$$W = 2\,AB = \sqrt{D^2 - d^2}$$

Thus the heat flow rate carried away by the channel flow is

$$\begin{aligned} Q &= \dot{m}\, c_p (T_S - T_\infty) \\ &= \frac{\rho\, g\, \beta\, c_p (\Delta T)^2 b^3}{12\, \nu} W \end{aligned} \tag{4.33}$$

Then the Nusselt number for one channel flow based on the channel surface area, A_{CL}, can be obtained:

$$\begin{aligned} Nu_{b,CLF} &= \frac{Q\, b}{\Delta T\, k\, A_{CL}} \\ &= \frac{\rho\, g\, \beta\, c_p (\Delta T)^2 b^3}{12\, \nu} \frac{b W}{\Delta T\, k\, A_{CL}} \\ &= \frac{1}{12} Ra_b \frac{b W}{A_{CL}} \\ &= \frac{1}{12} Ra_b^* \frac{D \sqrt{D^2 - d^2}}{A_{CL}} \end{aligned} \tag{4.34}$$

<u>Heat transfer due to outward conduction</u>: When Ra_b^* is very small. e.g. as the spacing b becomes small, the channel flow will be restricted, and the rate of heat carried away by the channel flow will be minimal. Under these circumstances heat will be transferred out of the channel primarily by conduction as shown in Fig. 4.8. This portion of the heat transfer will be modeled as convective heat transfer from an isothermal, cylindrical surface with diameter D and width b. This surface is referred to as the channel control surface and its body gravity function $G_{\sqrt{A_{CCS}}}$ can be found using Eq. (4.27).

$$G_{\sqrt{A_{CCS}}} = 0.891 \left(\frac{b}{D}\right)^{1/8} \tag{4.35}$$

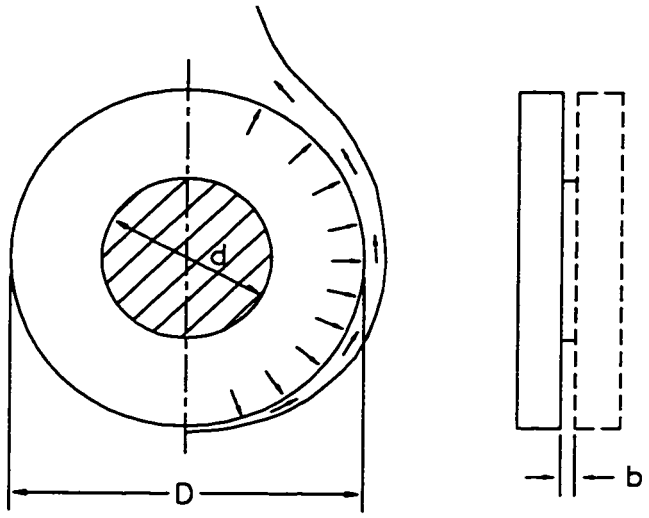

Figure 4.8: External Heat Transfer of Narrow Channel.

The heat transfer at this surface can also be calculated using Eq. (4.24):

$$Nu_{b,A_{CCS}} = F(Pr)\, G_{\sqrt{A}_{CCS}}\, (D/\sqrt{A}_{CCS})^{1/4}\, Ra_b^{*1/4} \tag{4.36}$$

This heat transfer is assumed from the channel surface, so it is converted to the channel surface area:

$$Nu_{b,CCS} = Nu_{b,A_{CCS}} A_{CCS}/A_{CL} \tag{4.37}$$

The heat transfer from the inner surface in the fully developed regime can be found by

$$Nu_{b,A_{IN-FD}} = Nu_{b,CLF} + Nu_{b,CCS} \tag{4.38}$$

Combining Two Limits.

The composite solution technique suggested by Churchill and Usagi (1972) is used to combine the two limits of the inner surface heat transfer to give the model for inner surface for a wide range of Ra_b^*:

$$Nu_{b,A_{IN}} = \left[(Nu_{b,A_{IN-T}})^{-n} + (Nu_{b,A_{IN-FD}})^{-n}\right]^{-1/n} \tag{4.39}$$

Based on comparisons with the present experimental data, previous correlations and experimental data, $n = 1$ was chosen for heat sink applications. The model may give better predictions if different values of n for different diameter ratio d/D are used. But for the purpose of simplicity, $n = 1$ was chosen for heat sink applications. In practice, diameter ratio of heat sinks does not change very much.

Channel Model.

For channel heat transfer ($D/d >> 1$ and without the outer surface heat transfer), the above model for inner surface can be applied with a small change. Because the channel heat transfer does not include heat transfer from the control surface, such as the Elenbaas correlation, Eq. (4.38) will be replaced by

$$Nu_{b,A_{IN-FD}} = Nu_{b,CLF} \tag{4.40}$$

In this case, the blending parameter n in Eq. (4.39) was chosen to be 1.7 based on the comparisons with Tsubouchi-Masuda (1970) channel correlation.

4.3.2 Thin Boundary Layer Model for Outer Surface

The body gravity function of the fin rim, $G_{\sqrt{A}_{RIM}}$, can be calculated using Eq. (4.27):

$$G_{\sqrt{A}_{RIM}} = 0.891\left(\frac{t}{D}\right)^{1/8} \tag{4.41}$$

and the body gravity function of the end surface, $G_{\sqrt{A}_{END}}$, can be found using Eq. (4.28) as

$$G_{\sqrt{A}_{END}} = 1.021 \tag{4.42}$$

With the assumption that the boundary layer flows over the fin rim and the end surfaces are independent of one another, the overall body gravity function for the outer surfaces, $G_{\sqrt{A}_{OUT}}$, can be obtained using Eq. (4.21) for parallel surface components. The thin boundary layer heat transfer from the outer surface then can be calculated using Eq. (4.24):

$$Nu_{b,A_{OUT}} = F(Pr)G_{\sqrt{A}_{OUT}}(D/\sqrt{A}_{OUT})^{1/4}\, Ra_b^{*1/4} \tag{4.43}$$

4.3.3 Effective Diffusive Limit

In a previous study by Wang (1993), it was shown that based on the circumscribed cylinder surface area, the diffusive limit of the heat sink is close to that of the circumscribed cylinder. Therefore, the diffusive limit of the circumscribed cylinder is taken to represent the heat sink, and it can be calculated using (Smythe 1956, 1962; Yovanovich 1987a) (for $0 \leq L/D \leq 8$)

$$Nu^0_{\sqrt{A}_{CC}} = \frac{3.1915 + 2.7726(L/D)^{0.76}}{\sqrt{1 + 2(L/D)}} \tag{4.44}$$

Based on the characteristic length b and the heat sink surface area, the diffusive limit is recast as

$$Nu^0_b = Nu^0_{\sqrt{A}_{CC}} \frac{\sqrt{A}_{CC}\, b}{A_{HS}} \tag{4.45}$$

4.3.4 Full Model for Heat Sink

The full model for the heat sink can be obtained by combining the three component solutions, namely the heat transfer from the inner surface, the thin boundary layer heat transfer from the outer surface and the diffusive limit.

Based on the total surface area of the heat sink, the contribution of the inner surface to the Nusselt number for the heat sink is

$$Nu_{b,IN} = Nu_{b,A_{IN}} \frac{A_{IN}}{A_{HS}} \tag{4.46}$$

while the contribution of the outer surface to the Nusselt number for the heat sink is

$$Nu_{b,OUT} = Nu_{b,A_{OUT}} \frac{A_{OUT}}{A_{HS}} \tag{4.47}$$

Finally, the total heat transfer from the heat sink is obtained as

$$Nu_b = Nu_b^0 + Nu_{b,OUT} + Nu_{b,IN} \tag{4.48}$$

The first term of Eq. (4.48) Nu_b^0 is for correction of curvature effect of the boundary layers. For a given heat sink (all the dimensions are fixed), as $Ra_b^* \to 0$ Nu_b^0 will be dominant. The contribution of the outer surface $Nu_{b,OUT}$ mainly depends on the ratio of the outer surface area to the total surface area. If the ratio is large, the relative contribution of the outer surface will be large. The contribution of the inner surface $Nu_{b,IN}$ depends on two factors. One is its surface area ratio to the total surface area, similar to that of the outer surface. The other is the mode of heat transfer over the inner surface. If it is a thin boundary layer heat transfer regime, the rate of heat transfer will be large. If it is a fully developed flow regime, the rate of heat transfer from the inner surface will be small. If the channel flow is restricted because of $Ra_b^* \to 0$, the rate of heat transfer from the inner surface will be very small.

4.3.5 Simplification of Model

In order to make the calculation of Nu_b, in Eq. (4.48), easier, the individual components of the Nusselt number have been simplified using the following correlation

equations.

When $0.1 \leq L/D \leq 8$, the diffusive limit, Nu_b^0, can be approximated by

$$Nu_b^0 = [3.36 + 0.087(L/D)] \sqrt{A_{CC}}\, b/A_{HS} \tag{4.49}$$

When $0.1 \leq t\,N_f/D \leq 8$, the Nusselt number for the outer surface, $Nu_{b,OUT}$, can be calculated by

$$Nu_{b,OUT} = [0.499 - 0.026 \ln(t\,N_f/D)]\, Ra_b^{*1/4} A_{OUT}/A_{HS} \tag{4.50}$$

The Nusselt number for the inner surface, $Nu_{b,IN}$, is

$$Nu_{b,IN} = Nu_{b,A_{IN}} \frac{A_{IN}}{A_{HS}} \tag{4.51}$$

with

$$Nu_{b,A_{IN}} = \left[(Nu_{b,A_{IN-T}})^{-n} + (Nu_{b,A_{IN-FD}})^{-n} \right]^{-1/n} \tag{4.52}$$

where $n = 1$ for heat sink applications.

For heat sinks in atmosphere, when $2.9 \times 10^4 \leq Ra_D \leq 2.3 \times 10^5$, a typical range for electronic heat sinks, and when $0.1 \leq d/D \leq 0.8$, the thin boundary layer Nusselt number for the inner surface, $Nu_{b,A_{IN-T}}$, can be calculated by

$$Nu_{b,A_{IN-T}} = \left[0.573 - 0.184(d/D) + 0.0388(d/D)^2 \right] Ra_b^{*1/4} \tag{4.53}$$

and the fully developed regime Nusselt number for the inner surface, $Nu_{b,A_{IN-FD}}$, is approximated by

$$Nu_{b,A_{IN-FD}} = \left[0.0323 - 0.0517(d/D) + 0.11(d/D)^2\right] Ra_b^{*1/4}$$
$$+ \left[0.0516 + 0.0154(d/D) - 0.0433(d/D)^2\right.$$
$$\left. + 0.0792(d/D)^3\right] Ra_b^* \quad (4.54)$$

For the channel model ($D/d >> 1$ and without the outer surface heat transfer),

$$Nu_{b,A_{IN-FD}} = \left[0.0516 + 0.0154(d/D) - 0.0433(d/D)^2\right.$$
$$\left. + 0.0792(d/D)^3\right] Ra_b^* \quad (4.55)$$

and the parameter n in Eq. (4.52) is taken as 1.7.

Although the model was simplified for heat sinks within the above parameter ranges, it is also used outside the parameter ranges in the following chapter. In Appendix E, comparisons between the full and simplified models are presented for four cases. It is shown that in the practical range of Ra_b^*, the simplified model agrees with the full model very well. In Appendix F, a summary of the present models is given, which includes both the full model and the simplified model.

4.3.6 Trends of Model Predictions

The model predictions for the heat sinks used in this study are shown in Fig. 4.9 for a wide range of Ra_b^* between 10^{-2} and 10^5. They are the five curves between the upper and lower limit curves for the heat sinks. The upper limit curve is the dashed line which represents a solid horizontal circular cylinder (specifically, $L = 75\ mm$, $D = 36.5\ mm$, $d/D = 0.999$, $t = 20\ mm$, $b = 35\ mm$ and $N_f = 2$). The lower limit curve is the thicker solid line which represents a heat sink with the same d/D as the test heat sinks but with very small fin thickness and very large fin number (specifically, $L = 75\ mm$, $D = 36.5\ mm$, $d/D = 0.6$, $t = 0.2\ mm$, $b = 0.2\ mm$

and $N_f = 188$). In this case, the inner surface heat transfer is dominant in the entire range of Ra_b^*, so the curve is similar to a channel heat transfer curve. All of the curves in Fig. 4.9 are generated by the present model. For each curve in this figure, geometric parameters are fixed, Ra_b^* varies with Ra_D.

If L/D, t/D and d/D of the heat sink and Pr are fixed, which is common practice by most researchers, Nu_b is a function of two parameters, i.e. $Nu_b = f(Ra_b^*, b/D)$, as shown in Fig. 4.9 where for each value of Ra_b^* there are multiple values of Nu_b corresponding to different heat sinks or different b/D. Similar trends of numerical results for parallel plate channel were reported previously by Martin et al. (1991) and Li and Chung (1996). Therefore comparisons with previous correlations (Edwards and Chaddock, 1963; Jones and Nwizu, 1969; Tsubouchi and Masuda, 1970) should be made in such a way that at each Ra_b^* value, the present values of b/D and Ra_D are the same as those in the previous experiments (note: $Ra_b^* = Ra_D\, b^4/D^4$).

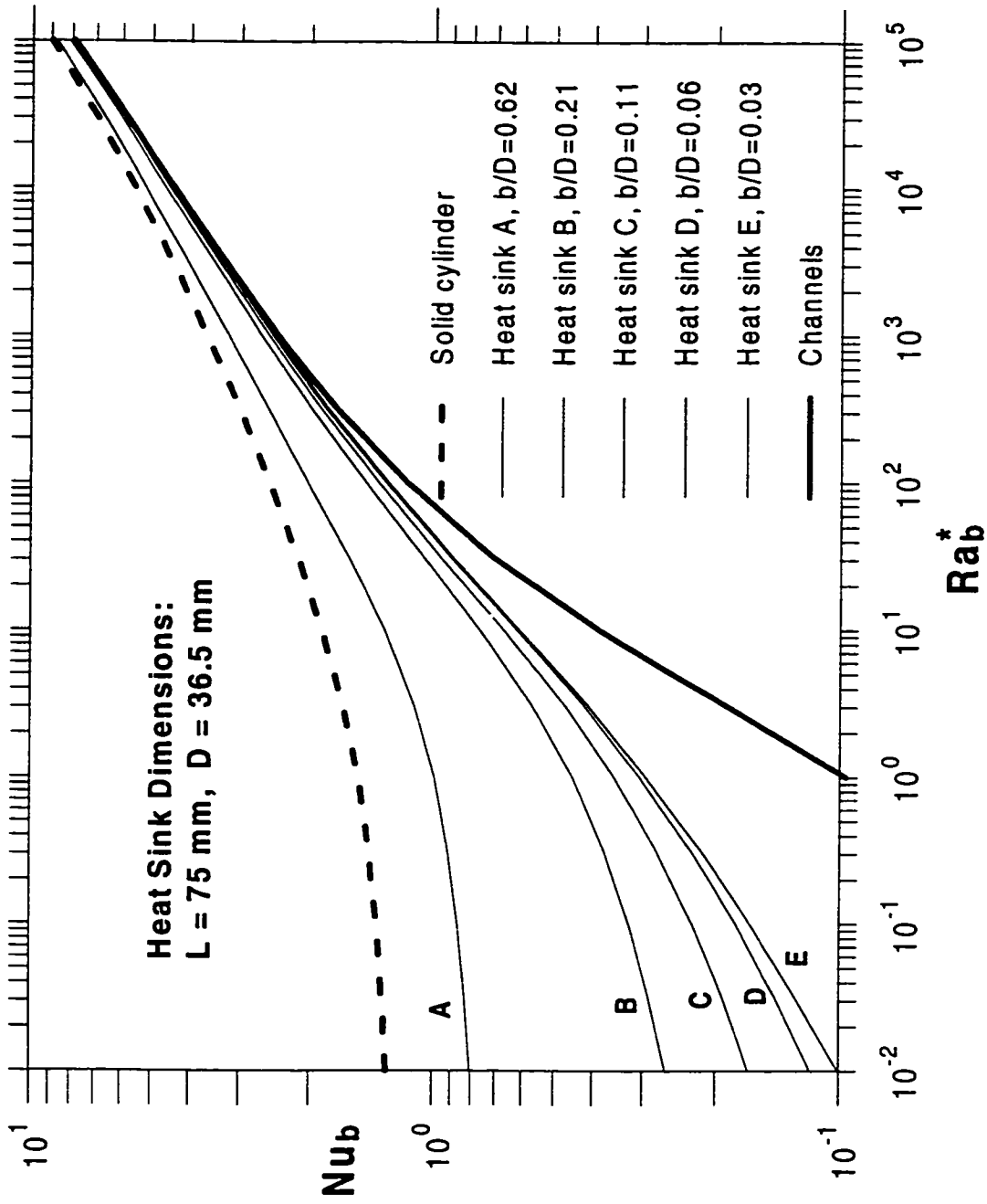

Figure 4.9: Trends of Model Predictions.

4.4 Radiation Model

In the natural convection regime, radiation can play an important role in the total heat transfer. To account for this, a radiative heat transfer model for annular-fin heat sinks is developed below.

As shown in Fig. 4.10, the heat sink is assumed to sit in a large enclosure, the temperature of the enclosure surface is T_2, the heat sink surface temperature is T_1.

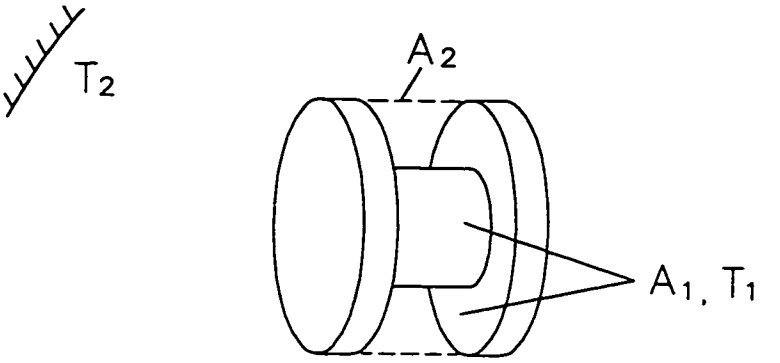

Figure 4.10: Heat Sink in Large Enclosure.

The inner surface of the heat sink, A_1, and the channel control surface, A_2, which is imaginary and represented by the dashed line in Fig. 4.10, form a small two surface enclosure. The surface A_1 is assumed isothermal, diffuse, gray and with uniform radiosity and irradiation. The surface A_2 can be considered as a black surface of temperature T_2. Thus the following equation is obtained (Incropera and DeWitt, 1990):

$$Q_{12} = \frac{\sigma(T_1^4 - T_2^4)}{\frac{1-\epsilon_1}{\epsilon_1 A_1} + \frac{1}{A_1 F_{12}} + \frac{1-\epsilon_2}{\epsilon_2 A_2}} \tag{4.56}$$

where Q_{12} is the radiative heat flow rate from surface A_1 to surface A_2, F_{12} is the view factor from surface A_1 to surface A_2, ϵ_1 and ϵ_2 are the emissivities of surface

A_1 and surface A_2, respectively. Because $A_1F_{12} = A_2F_{21}$ and $\epsilon_2 = 1$, the equation becomes

$$Q_{12} = \frac{\sigma(T_1^4 - T_2^4)}{\frac{1-\epsilon_1}{\epsilon_1 A_1} + \frac{1}{A_2 F_{21}}} \tag{4.57}$$

where F_{21} is the view factor from surface A_2 to surface A_1. F_{21} in turn can be found by

$$F_{21} = 1 - F_{22} \tag{4.58}$$

where F_{22} is the view factor from surface A_2 to itself, which can be found in the literature (Siegel and Howell, 1992):

$$\begin{aligned} F_{22} \;=\; & 1 - \frac{1}{R} + \frac{2}{\pi R}\tan^{-1}\left\{\frac{2\sqrt{R^2-1}}{B}\right\} - \frac{B}{2\pi R} \\ & \left[\frac{\sqrt{4R^2+B^2}}{B}\sin^{-1}\left\{\frac{4(R^2-1)+(B^2/R^2)(R^2-2)}{B^2+4(R^2-1)}\right\}\right. \\ & \left. - \sin^{-1}\left\{\frac{R^2-2}{R^2}\right\} + \frac{\pi}{2}\left(\frac{\sqrt{4R^2+B^2}}{B} - 1\right)\right] \end{aligned} \tag{4.59}$$

where $R = D/d$, $B = 2b/d$.

For a heat sink with N_f fins, the radiative heat transfer from the inner surface A_{IN} will be

$$Q_{R,IN} = (N_f - 1)\, Q_{12} \tag{4.60}$$

The radiative heat transfer from the outer surface, A_{OUT}, is given by

$$Q_{R,OUT} = \sigma\, \epsilon_1\, A_{OUT}(T_1^4 - T_2^4) \tag{4.61}$$

Finally, the total radiative dissipation from the heat sink is obtained:

$$Q_R = Q_{R,IN} + Q_{R,OUT} \tag{4.62}$$

This radiation model shows good agreement with the radiation measurements for the heat sinks used in this study.

4.5 Non-isothermal Fin Surfaces

Heat sinks used in practical applications are not truly isothermal; however, in many cases the temperature variation on the heat sink surface is small. To account of this temperature variation, an average temperature of the heat sink surface may need to be found before using the model for the heat sinks. It can be done through a fin efficiency analysis. Then the average temperature may be taken as the heat sink temperature in the model. Hahne and Zhu (1994) made comparisons between two sets of results for the heat sinks, one was obtained using the total surface area and the average temperature, the other was calculated with subsurface areas and their local temperatures. They found that the difference between the two sets of data was less than 1%. This supports the approach proposed above. In the cases with small surface temperature variation, finding the average surface temperature may not be necessary and the isothermal assumption will provide accurate results.

Several fin efficiency formulas for the annular fin can be found in the literature. one of them, which accounts for fin rim cooling, was given as follows (Yovanovich, 1995).

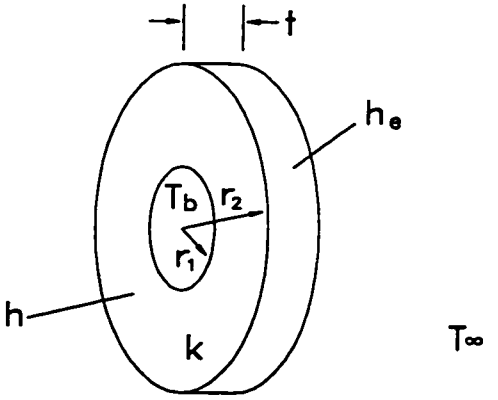

Figure 4.11: Parameters of Fin.

With reference to Fig. 4.11, if $h_e = h$, the fin efficiency can be found by

$$\eta = \frac{2\pi\sqrt{2hr_1^2kt}}{A_{fin}h}\left[\frac{\Phi K_1(mr_1) - I_1(mr_1)}{\Phi K_0(mr_1) + I_0(mr_1)}\right] \tag{4.63}$$

where $I_0(mr_1)$, $K_0(mr_1)$, $I_1(mr_1)$ and $K_1(mr_1)$ are modified Bessel functions. r_1 and r_2 are the inner and outer radii of the fin, A_{fin} is the surface area of the fin in Fig. 4.11, $2\pi(r_2^2 - r_1^2) + 2\pi r_2 t$, h is convective heat transfer coefficient, and

$$\Phi = \frac{mr_2I_1(mr_2) + Bi_eI_0(mr_2)}{mr_2K_1(mr_2) - Bi_eK_0(mr_2)} \tag{4.64}$$

with

$$Bi_e = \frac{h_e r_2}{k} \tag{4.65}$$

and

$$m = \sqrt{\frac{2h}{kt}} \tag{4.66}$$

The average temperature of the fin can be approximated by

$$T_{aver} = T_\infty + (T_b - T_\infty)\eta \tag{4.67}$$

If the heat transfer coefficient h, in Eq. (4.63), is unknown, it can be estimated using the present model with T_b as the heat sink temperature. The approximate average temperature can be found following the above procedure. This average temperature can be used in the model to find a better value of h, then a better average temperature can be calculated with this better h. By this iterative procedure, the estimation of the average temperature can be improved.

4.6 Summary

A dimensional analysis is made for the annular-fin heat sinks. It is shown that the Nusselt number $Nu_{\mathcal{L}}$ is a function of seven parameters namely $Ra_{\mathcal{L}}$, Pr, $b/\mathcal{L}$,

$D/\mathcal{L}$, $d/\mathcal{L}$, $t/\mathcal{L}$ and $L/\mathcal{L}$. In most previous experiments, the Nusselt number Nu_b was a function of two parameters, i.e. Ra_D and b/D. Therefore, when compared with the previous experimental results, the model should have the same values of b/D and Ra_D used in these experiments.

An approximate solution for fully developed flow between fins is derived. Based on the new expression of external natural convection solution, the fully developed flow solution and making the distinction between the external and internal surfaces, a general model for laminar natural convection heat transfer from isothermal, vertical disks with horizontal support cylinder is developed. In order to make the model easier to use, a simplified model is also presented.

The trends of the model prediction are shown in Fig. 4.9. It is consistent with the previous experiments and the numerical results.

To account for radiative heat transfer and non-isothermal fin surfaces, a radiation model for the heat sink is developed in Section 4.4, and a fin efficiency formula is presented in Section 4.5.

Comparisons between the full model and the simplified model are presented in Appendix E. A summary of the present models is given in Appendix F.

In the next chapter, the present model will be validated by comparisons with present experimental data, previous correlations and experimental data.

Chapter 5

Comparisons of Present Model with Previous Correlations and Experimental Data

In this chapter, the present simplified model is compared with three previous heat sink correlations in Section 5.1. The comparison between the present experimental data and the present model is given in Section 5.2. The comparison between the previous apple core data and the model is presented in Section 5.3. In the last two sections, the two limiting cases, i.e. $D/d >> 1$ and $D/d \rightarrow 1$, are examined. The model predictions are compared against experimental data obtained for long and short horizontal circular cylinders and a vertical thin circular disk. In these comparisons, the percent difference is given in the form:

$$\frac{Nu_b - Nu_b(reference)}{Nu_b(reference)} \times 100\%$$

5.1 Previous Correlations

As mentioned in the last chapter, in the previous experiments (Edwards and Chaddock, 1963; Jones and Nwizu, 1969; Tsubouchi and Masuda, 1970), Ra_D was more or less fixed and the wide range of Ra_b^* was achieved by variation of b/D. Therefore, in the following comparisons, the present model predictions are given in such

a way that Ra_D is fixed at an average value and Ra_b^* varies with b/D. In addition, the heat sink dimensions used by Edwards and Chaddock (1963) are adopted for the present model. In their experiments, the length of the heat sinks, L, the thickness of fins, t, and the diameter of the support cylinder, d, were fixed. They made measurements for three cases of the diameter ratio (D/d = 1.94, 2.97 and 5.17). In the following three subsections, the present model is compared with the three previous correlations for these diameter ratios. It is convenient to use the present model as the common reference in the comparisons. The more detailed comparisons between the present model and each of the correlations are tabulated in Appendix D.

5.1.1 Diameter ratio $D/d = 1.94$

In Fig. 5.1, the present model is compared with the previous correlations for D/d = 1.94. Good agreement can be seen between the model and the three correlations. The maximum difference is -9.8% and the RMS difference is 5.4% between the model and the Jones-Nwizu correlation. In comparison of the model and the Tsubouchi-Masuda correlation, one finds the maximum and the RMS differences are -11.3% and 6.4%, respectively.

In the experiments of Edwards and Chaddock, the end surfaces of the heat sink were active, while for the heat sinks of Jones and Nwizu, Tsubouchi and Masuda, the end surfaces were insulated. This may be one of the reasons for the Edwards-Chaddock correlation giving higher predictions for this case.

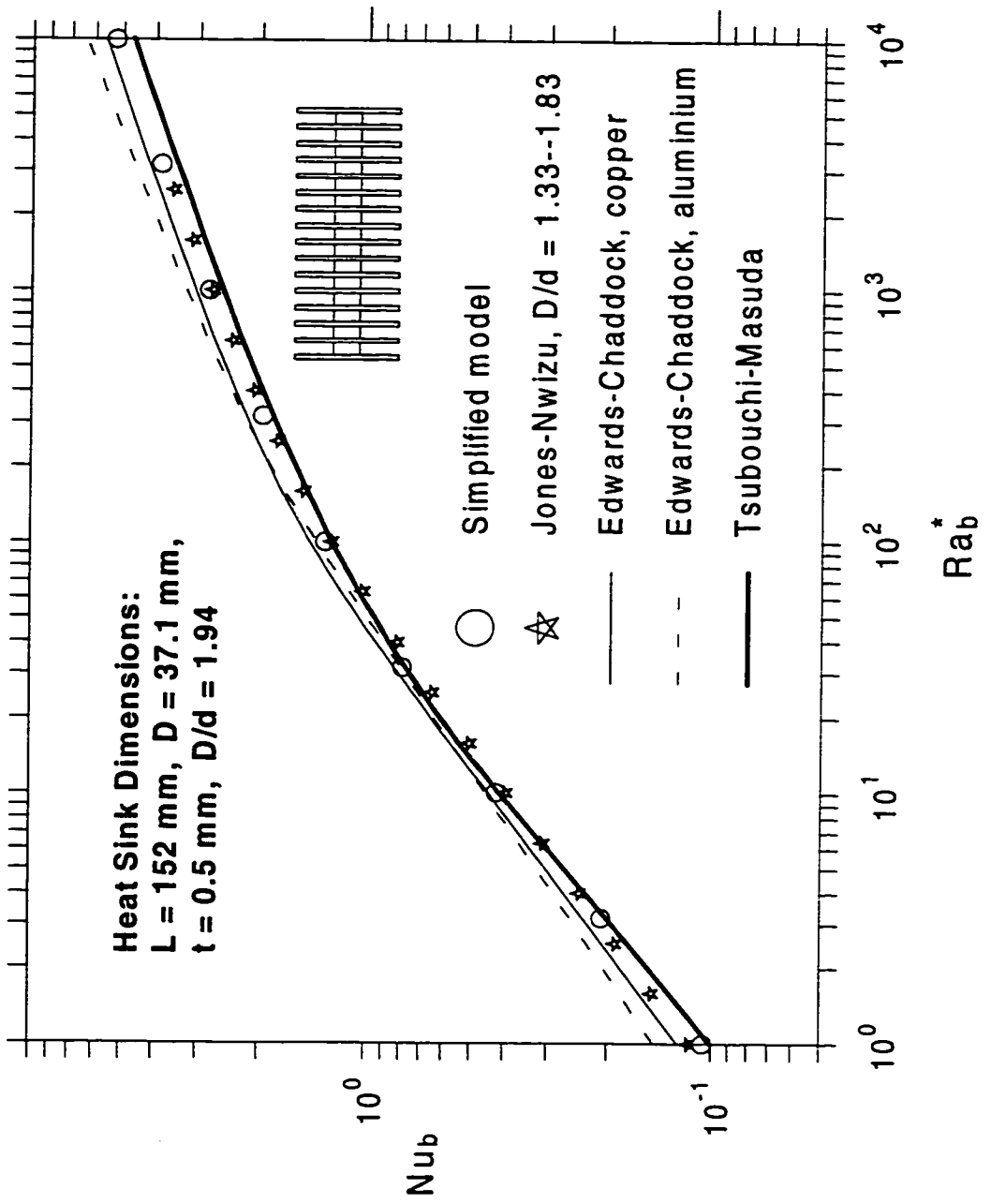

Figure 5.1: Comparison with Previous Correlations ($D/d = 1.94$).

5.1.2 Diameter ratio $D/d = 2.97$

The comparisons for $D/d = 2.97$ are shown in Fig. 5.2. The agreement is also good. The maximum difference between the model and the Tsubouchi-Masuda correlation is 13.7% and the RMS difference is 8.7%. Although the Jones-Nwizu correlation is applicable for the region of $D/d = 1.33 \sim 1.83$, it shows good agreement at high Ra_b^*, i.e. at the thin boundary layer regime. In the region of low Ra_b^*, the correlation gives slightly higher Nu_b predictions, because the value of D/d is beyond its applicable range.

The Edwards-Chaddock correlation for copper fins also shows very good agreement for this case in the range of $Ra_b^* = 16 \sim 10^4$. Both the maximum difference and the RMS difference are about 3% in this range of Ra_b^*.

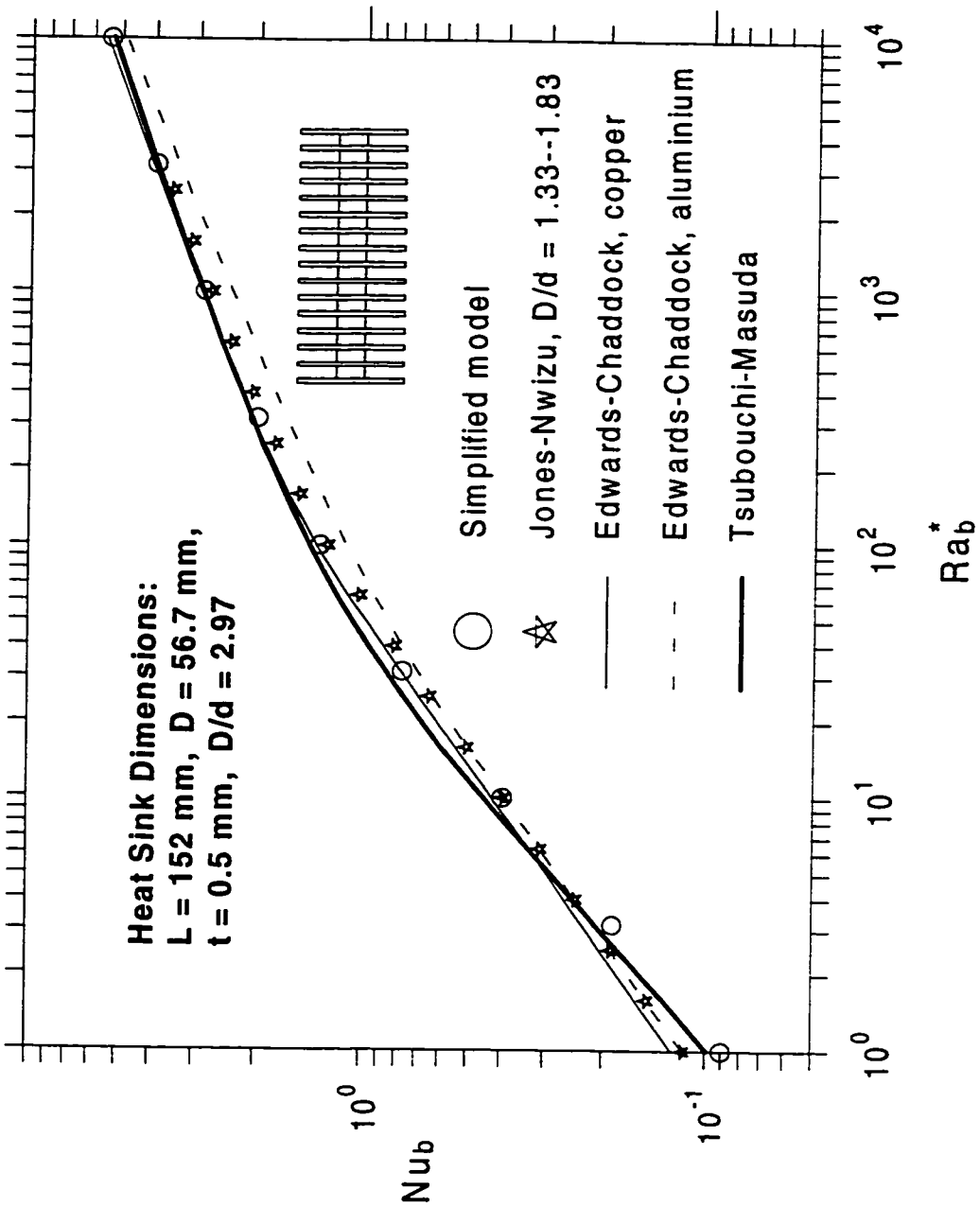

Figure 5.2: Comparison with Previous Correlations ($D/d = 2.97$).

5.1.3 Diameter ratio $D/d = 5.17$

Figure 5.3 shows comparisons between the model and the previous correlations for $D/d = 5.17$. Good agreement can be seen between the model and the Edwards-Chaddock correlation for aluminum fins. The maximum difference and the RMS differences are -11.5% and 8.1%, respectively. The model also shows good agreement with the Jones-Nwizu correlation at high Ra_b^*. The Jones-Nwizu correlation again gives higher predictions at low Ra_b^*, e.g. the 38% higher value than the present model at $Ra_b^* = 1$. As D/d is large, the inner surface becomes a large portion of the total heat sink surface. At low Ra_b^*, the large portion of the heat sink surface will be involved with the fully developed flow, and hence result in lower Nu_b when compared with the case of small D/d. Because in fully developed flow regime, the surface heat flux is much smaller than that in thin boundary layer regime. The Jones-Nwizu correlation does not account for $D/d > 1.83$, so it gives higher predictions at low Ra_b^*.

The Edwards-Chaddock correlation gives lower predictions than the other correlations at most values of Ra_b^*. One of the reasons may be the effect of nonisothermal fins. Edwards and Chaddock took the temperature of the support cylinder as the heat sink temperature. When D/d is large, this temperature may be much larger than the average temperature of the heat sink; and it will lead to lower predictions of the Nusselt number.

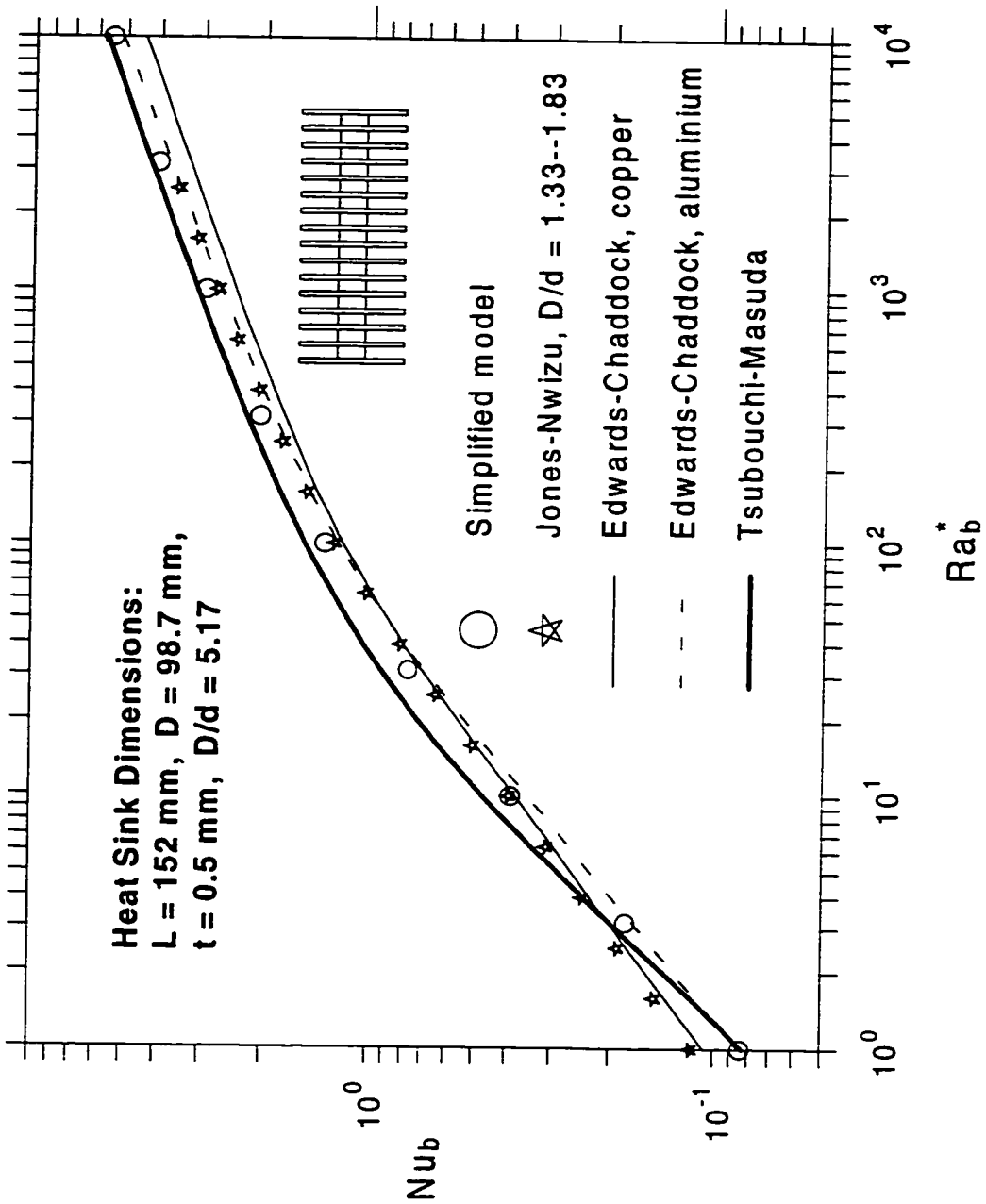

Figure 5.3: Comparison with Previous Correlations ($D/d = 5.17$).

5.2 Present Experimental Data

In Table 5.1 — 5.5, and Fig. 5.4 the present model is compared with the present experimental data. Three previous correlations are also shown in Fig. 5.4 as a comparison. Similar to the above comparison with the previous correlations, the present model predictions are given in such a way that Ra_D is fixed at an average value and Ra_b^* varies with b/D. In addition, the dimensions of the test heat sinks are used in the present model. In the comparisons, the present model predictions are taken as the common reference.

Although the five heat sinks used for the experimental study were tested under similar conditions, or the Ra_D is nearly the same for the five heat sinks, the experimental results (square symbols) lie in different ranges of Ra_b^* because they have different values of b/D. In the order A, B, C, D and E, the experimental results of the heat sinks lie in the range of $Ra_b^* = 2\times10^4$ to 10^{-1}. The agreement between the experimental data and the present model is very good, with a maximum difference of 6.2% and an RMS difference of 4.3%. Figure 5.4 also shows that the previous correlations cannot predict heat transfer from these heat sinks at low Ra_b^*. Since there are just a few fins on these heat sinks, the end surfaces play a significant role in the total heat transfer, and the heat transfer from the fin rim surfaces is also significant in these cases due to the large fin-thickness. These two factors were not considered in the previous correlations, therefore they cannot account for the heat transfer from the end surfaces and the much larger fin rim surfaces, and give much lower predictions for the test heat sinks at low values of Ra_b^*.

An interesting result trend related to the surface area ratio is shown in Fig. 5.4. In the range of $Ra_b^* = 10^{-1} \sim 10^2$, when the outer surface area is only a very small portion of the total heat sink surface area, the results follow the curves close to the Elenbaas correlation which has unit slope (e.g. the three previous correlations);

when the outer surface is a large portion of the total heat sink surface (e.g. heat sinks tested in the present experiment), the results will pull away the curve of the Elenbaas correlation, assuming a slope smaller than 1 (between 1/4 and 1) in log-log plots.

Table 5.1: Comparisons of Model and Data for Heat Sink A.

Ra_b^*	Exp. Data Nu_b	Present Model Nu_b	% Diff.
4.875×10^3	4.268	4.280	-0.3
8.421×10^3	4.886	4.941	-1.1
1.159×10^4	5.216	5.371	-2.9
1.403×10^4	5.470	5.647	-3.1
1.628×10^4	5.690	5.870	-3.1
1.853×10^4	5.881	6.072	-3.1
2.079×10^4	5.971	6.257	-4.6
2.261×10^4	6.175	6.395	-3.4
2.405×10^4	6.252	6.499	-3.8
2.550×10^4	6.303	6.598	-4.5
2.682×10^4	6.334	6.686	-5.3
2.857×10^4	6.412	6.796	-5.7
3.024×10^4	6.564	6.898	-4.8
3.161×10^4	6.627	6.978	-5.0
3.250×10^4	6.649	7.028	-5.4
3.366×10^4	6.723	7.093	-5.2
3.484×10^4	6.818	7.157	-4.7
3.591×10^4	6.870	7.214	-4.8

RMS Diff = 4.2%

Table 5.2: Comparisons of Model and Data for Heat Sink B.

Ra_b^*	Exp. Data Nu_b	Present Model Nu_b	% Diff.
1.589×10^2	1.595	1.661	-4.0
2.105×10^2	1.729	1.807	-4.3
2.519×10^2	1.819	1.905	-4.5
2.872×10^2	1.884	1.979	-4.8
3.226×10^2	1.944	2.047	-5.0
3.550×10^2	1.987	2.104	-5.5
3.855×10^2	2.028	2.154	-5.8
4.086×10^2	2.054	2.190	-6.2

RMS Diff = 5.1%

Table 5.3: Comparisons of Model and Data for Heat Sink C.

Ra_b^*	Exp. Data Nu_b	Present Model Nu_b	% Diff.
8.025×10^0	0.634	0.602	5.4
1.319×10^1	0.718	0.719	-0.2
1.718×10^1	0.785	0.791	-0.8
2.056×10^1	0.838	0.844	-0.7
2.405×10^1	0.874	0.892	-2.0
2.709×10^1	0.899	0.930	-3.3
2.895×10^1	0.912	0.952	-4.2
3.112×10^1	0.938	0.976	-3.9

RMS Diff = 3.0%

Table 5.4: Comparisons of Model and Data for Heat Sink D.

Ra_b^*	Exp. Data Nu_b	Present Model Nu_b	% Diff.
9.490×10^{-1}	0.296	0.296	0.2
1.204×10^{0}	0.313	0.318	-1.5
1.390×10^{0}	0.325	0.332	-2.2
1.590×10^{0}	0.338	0.347	-2.5
1.779×10^{0}	0.352	0.359	-2.0
1.967×10^{0}	0.357	0.371	-3.8

RMS Diff = 2.3%

Table 5.5: Comparisons of Model and Data for Heat Sink E.

Ra_b^*	Exp. Data Nu_b	Present Model Nu_b	% Diff.
5.70×10^{-2}	0.140	0.143	-1.9
7.50×10^{-2}	0.150	0.153	-2.1
8.90×10^{-2}	0.157	0.160	-2.0
1.03×10^{-1}	0.162	0.166	-2.6
1.14×10^{-1}	0.166	0.171	-2.8
1.25×10^{-1}	0.169	0.175	-3.5
1.35×10^{-1}	0.173	0.179	-3.2
1.41×10^{-1}	0.175	0.181	-3.1

RMS Diff = 2.7%

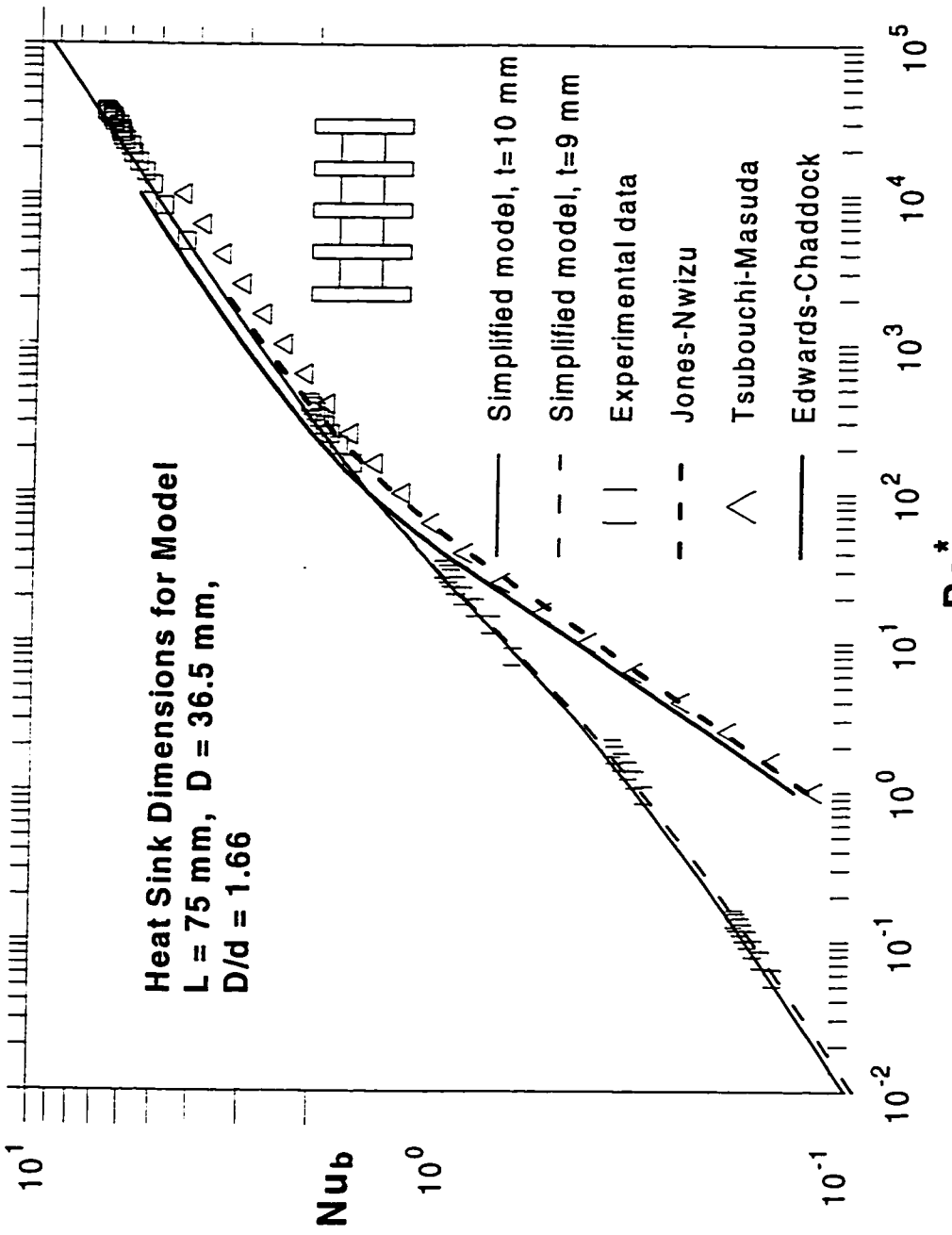

Figure 5.4: Comparison with Present Experimental Data.

5.3 Experimental Data for Apple Core

In this section the present model is compared against a set of experimental data of Hassani and Hollands (1989) who measured natural convection heat transfer from a horizontal, isothermal apple core made of an aluminum alloy.

In order to use the present model, a heat sink equivalent to the apple core was adopted. As shown in Fig. 5.5, the equivalent heat sink has two fins; the diameter D, dimensionless parameters d/D and b/D are equal to those of the apple core. The inner surface area and the outer surface area are the same as those of the apple core. The fin thickness t was determined by equating the outer surface area of the heat sink to the outer surface area of the apple core.

In this comparison the geometry of the heat sink was fixed, so the modified Rayleigh number Ra_b^* varied with Ra_D (note: $Ra_b^* = Ra_D\, b^4/D^4$). This was the way Hassani and Hollands (1989) performed their experiments.

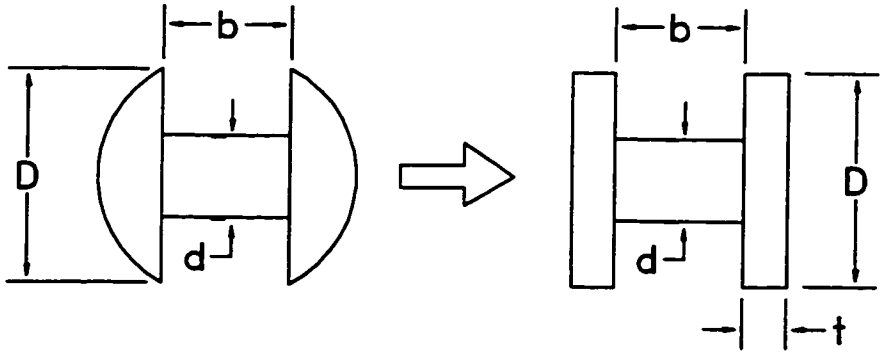

Figure 5.5: Apple Core and Equivalent Heat Sink.

Because the inner surfaces of the apple core and the equivalent heat sink have the identical shape and area, the heat transfer from the both inner surfaces should

be very close. Although the geometries of the two outer surfaces are different, they have the same surface area and hence the heat transfer rates from the two outer surfaces should be close. Finally, the diffusive limits of the two geometries are also close. Therefore the Nusselt number of the heat sink should be very close to that of the apple core.

Results for the two geometries are shown in Table 5.6 and Fig. 5.6 with the apple core data as the reference. The original data of the apple core have been converted to the Nusselt number based on b, i.e. Nu_b versus the modified Rayleigh number Ra_b^*. Good agreement can be seen with the maximum difference of 11.6% and the RMS difference of 5.9%. The predictions of the Hassani-Hollands model for the apple core are also shown in the figure as a comparison. Very good agreement can be seen between the present model and the Hassani-Hollands model in the range of $Ra_b^* = 10^2 \sim 3.6 \times 10^5$. This case confirms that the present model can be applied to this kind of problem, in which the geometry is fixed and Ra_b^* varies with Ra_D through pressure changes.

Table 5.6: Results for Apple Core of Hassani and Hollands.

($D/d = 1.86$, $D = 43.3\ mm$, $b = 25\ mm$, $n = 1.0$)

Ra_b^*	Apple Core Data Nu_b	Present Model Nu_b	% Diff.
1.485×10^0	1.365	1.259	-7.7
2.071×10^0	1.390	1.296	-6.8
2.876×10^0	1.404	1.338	-4.7
3.656×10^0	1.418	1.372	-3.3
5.121×10^0	1.458	1.427	-2.1
7.159×10^0	1.486	1.490	0.3
9.309×10^0	1.537	1.546	0.6
1.182×10^1	1.655	1.601	-3.3
1.271×10^1	1.593	1.619	1.6
1.337×10^1	1.545	1.632	5.6
1.634×10^1	1.698	1.685	-0.8
1.739×10^1	1.641	1.702	3.7
1.832×10^1	1.667	1.717	3.0
2.254×10^1	1.729	1.777	2.8
2.539×10^1	1.779	1.814	1.9
4.041×10^1	1.977	1.970	-0.4
5.541×10^1	2.047	2.087	1.9
6.744×10^1	2.090	2.164	3.6
7.608×10^1	2.107	2.214	5.1
9.058×10^1	2.166	2.287	5.6
1.219×10^2	2.231	2.419	8.5
1.781×10^2	2.383	2.600	9.1
2.362×10^2	2.496	2.745	10.0
3.149×10^2	2.600	2.900	11.6

– More –

Table 5.6: (cont.) Results for Apple Core of Hassani and Hollands.

($D/d = 1.86$, $D = 43.3\ mm$, $b = 25\ mm$, $n = 1.0$)

Ra_b^*	Apple Core Data Nu_b	Present Model Nu_b	% Diff.
4.513×10^2	2.831	3.109	9.8
5.909×10^2	2.972	3.277	10.2
7.781×10^2	3.099	3.458	11.6
1.160×10^3	3.381	3.741	10.6
1.563×10^3	3.618	3.970	9.7
2.128×10^3	3.838	4.224	10.1
3.083×10^3	4.450	4.554	2.3
4.045×10^3	4.667	4.815	3.2
5.342×10^3	4.870	5.101	4.7
8.035×10^3	5.220	5.556	6.4
1.025×10^4	5.513	5.850	6.1
1.318×10^4	5.792	6.173	6.6
1.933×10^4	6.342	6.703	5.7
2.410×10^4	6.689	7.033	5.1
3.029×10^4	7.022	7.394	5.3
4.821×10^4	7.902	8.193	3.7
5.776×10^4	8.206	8.530	4.0
6.952×10^4	8.499	8.891	4.6
1.184×10^5	9.811	10.027	2.2
1.400×10^5	10.186	10.417	2.3
1.663×10^5	10.555	10.834	2.6
3.257×10^5	13.107	12.648	-3.5
3.631×10^5	13.274	12.972	-2.3

RMS Diff = 5.9%

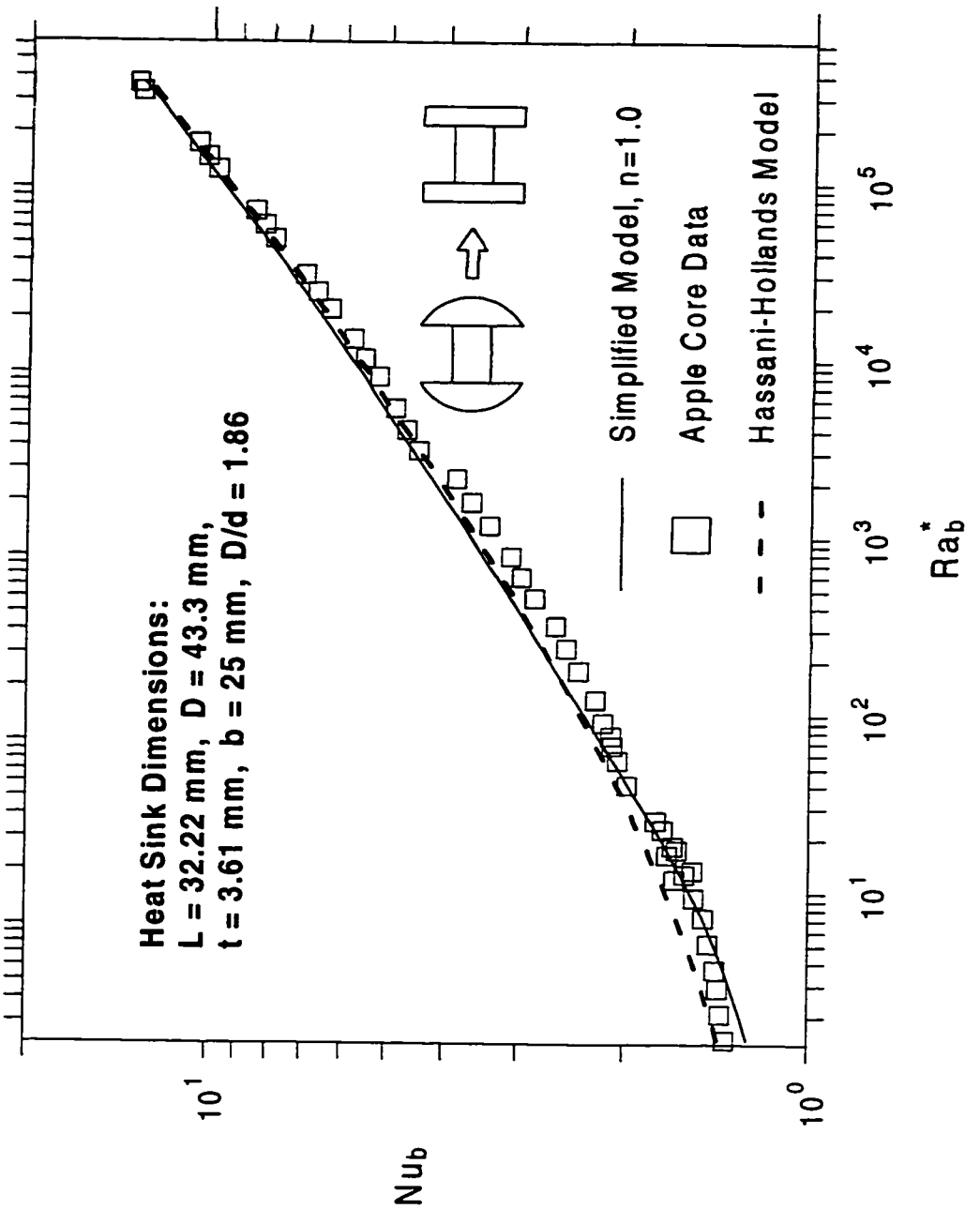

Figure 5.6: Comparison with Apple Core Data of Hassani and Hollands.

5.4 Comparison of Channel Model with Previous Correlations

When $D/d >> 1$, the effect of the support cylinder on the total heat transfer becomes negligible. In this case the heat transfer from the inner surface should be close to that of a channel. From this point of view, the present channel model will be compared with three previous channel model correlations. One is the Tsubouchi-Masuda (1970) correlation for a circular disk channel:

$$Nu_b = \frac{1}{6\pi} Ra_b^* \left\{ 1 - exp\left[-(25.3/Ra_b^*)^{3/4} \right] \right\} \tag{5.1}$$

The second is the Elenbaas (1942) correlation for a plate channel:

$$Nu_s = \frac{1}{24} Ra_s^* \left[1 - exp(-35/Ra_s^*) \right]^{3/4} \tag{5.2}$$

And the third is the Raithby-Hollands (1985) correlation for square fins:

$$Nu_s = \left[\left(\frac{Ra_s^{*0.89}}{18} \right)^{-2.7} + (0.62 Ra_s^{*1/4})^{-2.7} \right]^{-1/2.7} \tag{5.3}$$

In these comparisons, the modified Rayleigh number varied with b/D or s/H, in the same way in which the previous measurements were performed.

5.4.1 Tsubouchi-Masuda Disk Channel Correlation

Both the present channel model and the Tsubouchi-Masuda correlation represent a pure channel heat transfer between two circular disks. In this comparison the dimensions of the disk channel used in the experiments of Tsubouchi and Masuda (1970) were adopted in the present model. And the predictions of the Tsubouchi-Masuda correlation are taken as the reference.

In Table 5.7 and Fig. 5.7, the present channel model, Eq. (4.52) with Eq. (4.53) and Eq. (4.55), is compared with the Tsubouchi-Masuda correlation. Very good agreement can be seen over the entire range of the Ra_b^*. The maximum difference is -5.9% at $Ra_b^* = 4$, and the RMS difference is 3.5%.

Table 5.7: Results for Tsubouchi-Masuda Disk Channel.

($D/d = 82$, $n = 1.7$)

Ra_b^*	Tsubouchi-Masuda Nu_b	Channel Model $Nu_{b,A_{I,N}}$	% Diff.
1.000×10^0	0.053	0.051	-3.3
1.585×10^0	0.084	0.081	-4.1
2.512×10^0	0.133	0.126	-5.1
3.981×10^0	0.207	0.195	-5.9
6.310×10^0	0.315	0.297	-5.8
1.000×10^1	0.459	0.440	-4.2
1.585×10^1	0.638	0.629	-1.4
2.512×10^1	0.845	0.857	1.5
3.981×10^1	1.075	1.112	3.4
6.310×10^1	1.325	1.379	4.1
1.000×10^2	1.592	1.648	3.6
1.585×10^2	1.877	1.922	2.4
2.512×10^2	2.182	2.206	1.1
3.981×10^2	2.511	2.508	-0.1
6.310×10^2	2.869	2.834	-1.2
1.000×10^3	3.261	3.193	-2.1
1.585×10^3	3.693	3.591	-2.8
2.512×10^3	4.170	4.034	-3.3
3.981×10^3	4.701	4.530	-3.6
6.310×10^3	5.292	5.084	-3.9
1.000×10^4	5.951	5.706	-4.1

RMS Diff = 3.5%

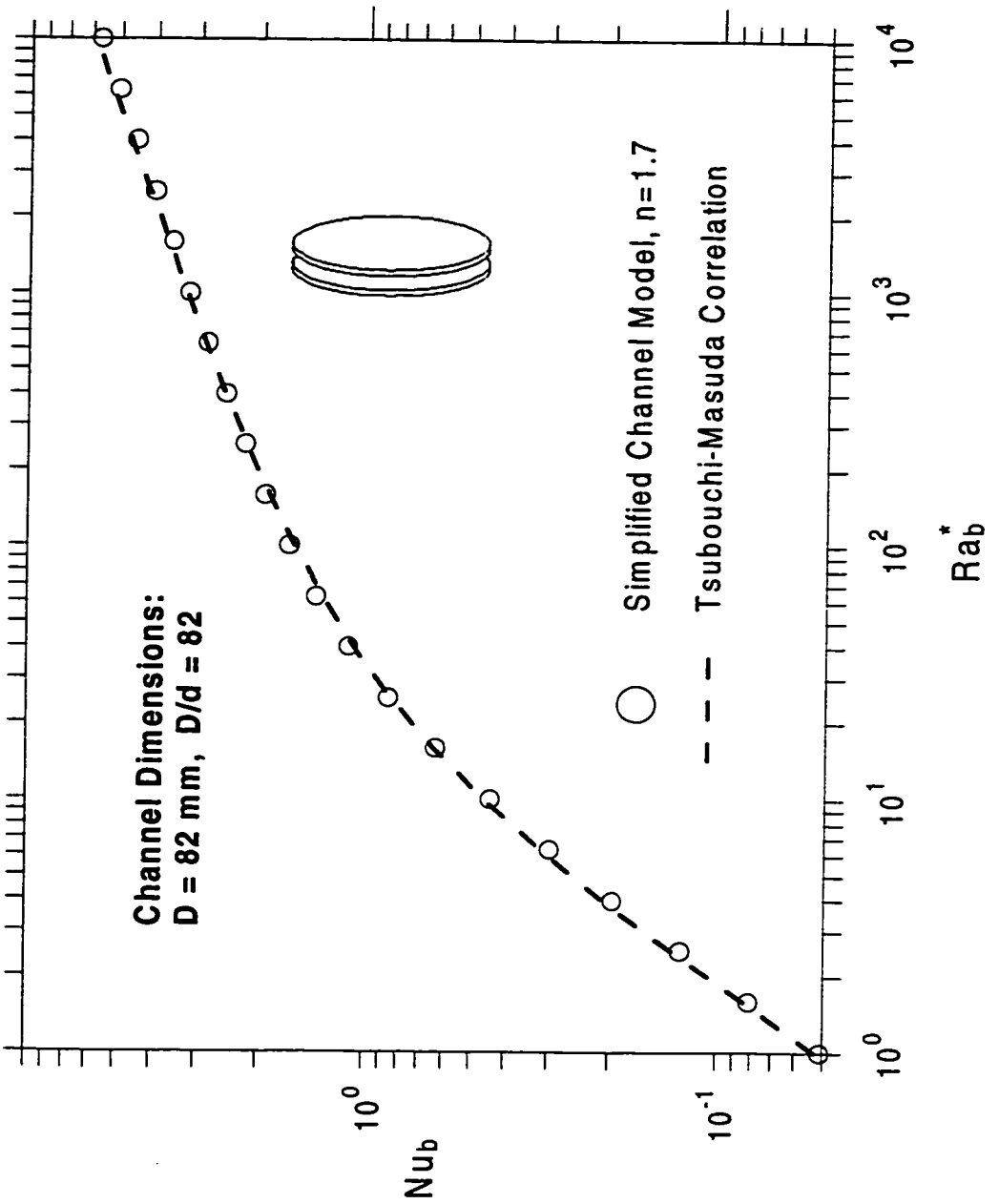

Figure 5.7: Comparison with Tsubouchi-Masuda Disk Channel.

5.4.2 Elenbaas Plate Channel Correlation

The present channel model is compared with the Elenbaas correlation in Table 5.8 and Fig. 5.8. The Elenbaas correlation is the reference in the comparison. The model is for a circular disk channel, while the Elenbaas correlation is for a rectangular plate channel. Although the geometries are different, the results are close to each other over a wide range of Ra_b^*. The disk channel dimensions of Tsubouchi and Masuda mentioned above were adopted for the present model, because the dimensions are within the range of the channel dimensions of Elenbaas.

The agreement is very good in the range of $Ra_b^* = 16 \sim 10^4$, with the maximum difference of -4.7%. But in the range of $Ra_b^* = 1 \sim 10$, large differences, up to 23% at $Ra_b^* = 1$, are observed.

Table 5.8: Comparison with Elenbaas Correlation for Channel.

$(D/d = 82.\ n = 1.7)$

Ra_b^* (or Ra_s^*)	Elenbaas Correlation Nu_s	Channel Model $Nu_{b,A_{IN}}$	% Diff.
1.000×10^0	0.042	0.051	23.1
1.585×10^0	0.066	0.081	22.1
2.512×10^0	0.105	0.126	20.4
3.981×10^0	0.166	0.195	17.6
6.310×10^0	0.262	0.297	13.2
1.000×10^1	0.407	0.440	8.1
1.585×10^1	0.605	0.629	3.9
2.512×10^1	0.845	0.857	1.5
3.981×10^1	1.109	1.112	0.3
6.310×10^1	1.386	1.379	-0.5
1.000×10^2	1.669	1.648	-1.2
1.585×10^2	1.961	1.922	-2.0
2.512×10^2	2.267	2.206	-2.7
3.981×10^2	2.592	2.508	-3.3
6.310×10^2	2.943	2.834	-3.7
1.000×10^3	3.328	3.193	-4.1
1.585×10^3	3.752	3.591	-4.3
2.512×10^3	4.223	4.034	-4.5
3.981×10^3	4.747	4.530	-4.6
6.310×10^3	5.333	5.084	-4.7
1.000×10^4	5.988	5.706	-4.7

RMS Diff = 10.1%

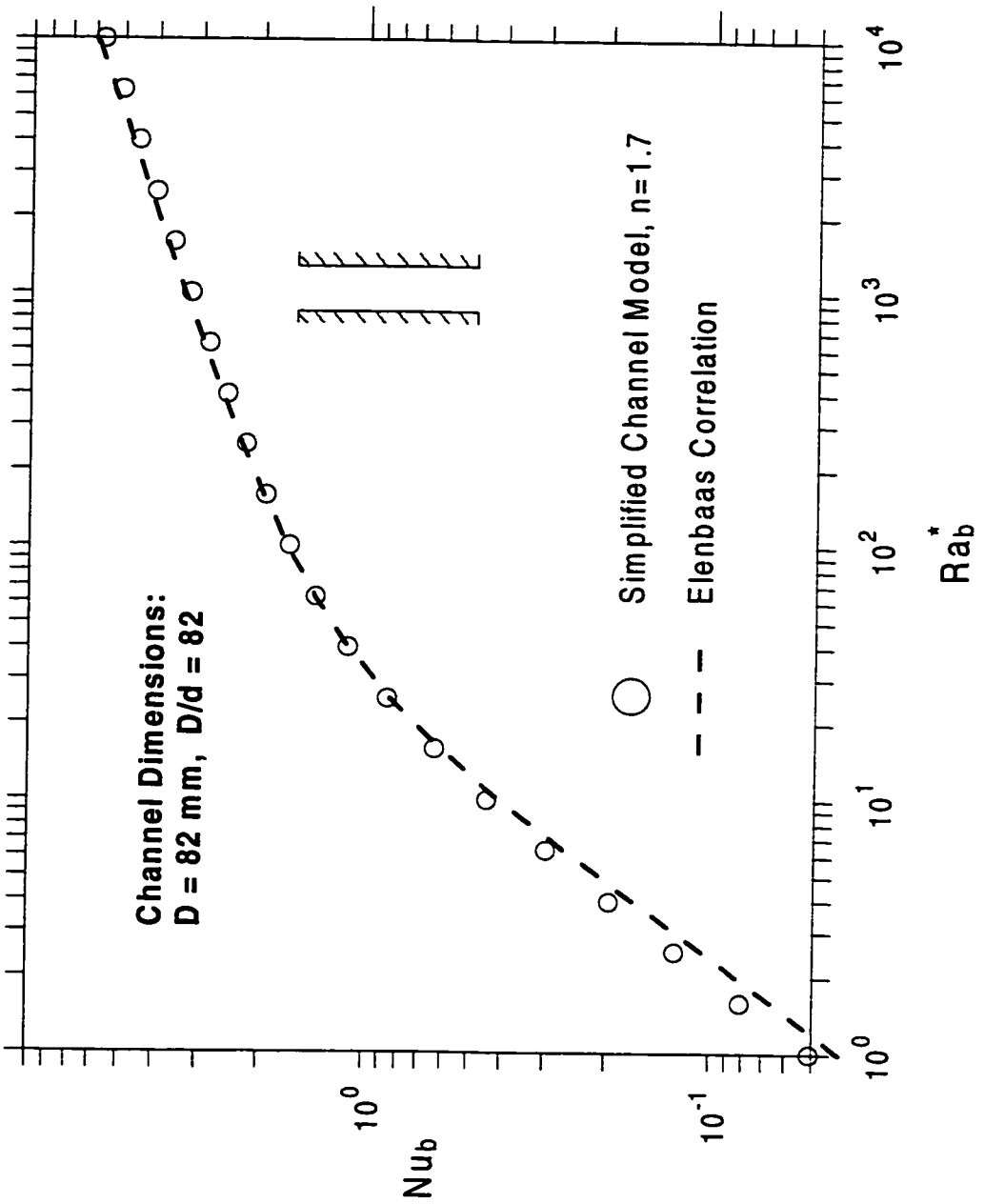

Figure 5.8: Comparison with Elenbaas Correlation for Channel.

5.4.3 Raithby-Hollands Square Fins Correlation

The present channel model is compared with the Raithby-Hollands correlation for square fins in Table 5.9 and Fig. 5.9. The predictions of the Raithby-Hollands correlation are taken as the reference. The dimensions of the Tsubouchi-Masuda disk channel were adopted for the present channel model, because they are within the range of the dimensions used in the experiments of Elenbaas. The data of Elenbaas were the basis of the Raithby-Hollands correlation.

Good agreement is seen in the comparison, with a maximum difference of -9.1% and an RMS difference of 7%. The Raithby-Hollands correlation gives higher predictions for most values of Ra_b^*. One of the reasons may be that their correlation accounts for the edge effect of the fins.

Table 5.9: Comparison with Raithby-Hollands Correlation.

$(D/d = 82,\ n = 1.7)$

Ra_b^* (or Ra_s^*)	Raithby-Hollands Nu_s	Present Model $Nu_{b,A_{I,N}}$	% Diff.
1.000×10^0	0.056	0.051	-7.7
1.585×10^0	0.084	0.081	-3.5
2.512×10^0	0.126	0.126	0.2
3.981×10^0	0.189	0.195	3.3
6.310×10^0	0.283	0.297	5.1
1.000×10^1	0.419	0.440	5.0
1.585×10^1	0.612	0.629	2.8
2.512×10^1	0.867	0.857	-1.0
3.981×10^1	1.171	1.112	-5.0
6.310×10^1	1.495	1.379	-7.8
1.000×10^2	1.813	1.648	-9.1
1.585×10^2	2.119	1.922	-9.3
2.512×10^2	2.426	2.206	-9.1
3.981×10^2	2.748	2.508	-8.7
6.310×10^2	3.096	2.834	-8.5
1.000×10^3	3.481	3.193	-8.3
1.585×10^3	3.909	3.591	-8.1
2.512×10^3	4.388	4.034	-8.1
3.981×10^3	4.924	4.530	-8.0
6.310×10^3	5.525	5.084	-8.0
1.000×10^4	6.200	5.706	-8.0

RMS Diff = 7.0%

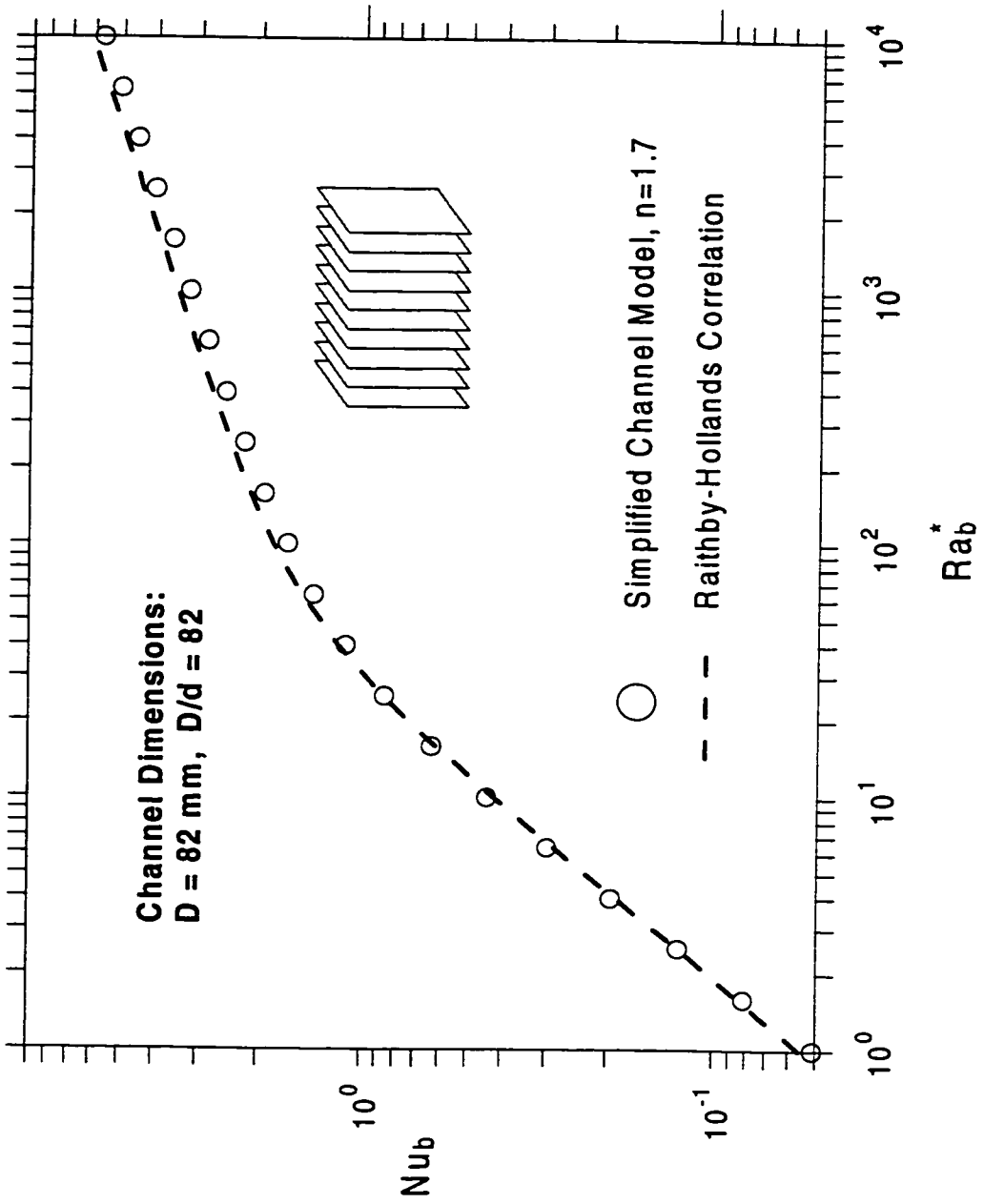

Figure 5.9: Comparison with Raithby-Hollands Correlation.

5.4.4 Comparison with Three Previous Correlations

In Fig. 5.10, the present channel model is compared with the three channel correlations, i.e. the Tsubouchi-Masuda correlation for a disk channel, the Elenbaas correlation for a plate channel and the Raithby-Hollands correlation for square fins. The three correlations show the same trend and are close to each other, because they represent the same thing, i.e. channel heat transfer. Over most values of Ra_b^*, the predictions of the present model lie between those of the previous correlations.

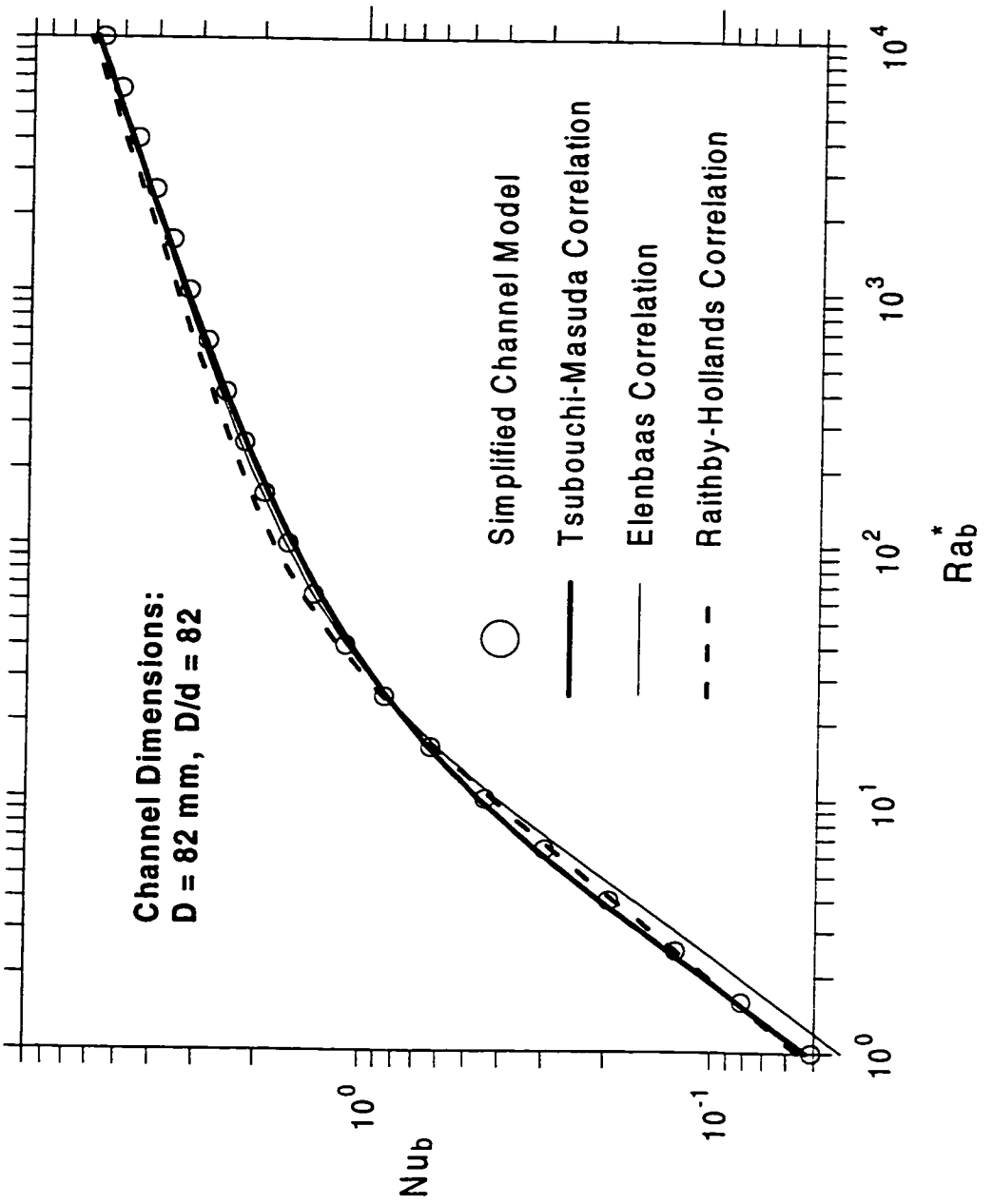

Figure 5.10: Comparison with Three Previous Correlations.

5.5 Comparison of Model with Circular Cylinder Data

In this section, the present model will be compared with cases for the other limit: $D/d \rightarrow 1$. The predictions of the present model are converted, to be based on the characteristic length D, in the form of Nu_D vs Ra_D. In these cases, b/D is fixed, the modified Rayleigh number varies with Ra_D. This is the way the previous experiments were performed. The experimental data are taken as the references in the following comparisons.

5.5.1 Long Circular Cylinder Data of Clemes et al.

The comparison of the present model and the long horizontal circular cylinder data of Clemes et al. (1994) is given in Table 5.10 and plotted in Fig. 5.11. The dimensions of the circular cylinder of Clemes are $D = 49.98\ mm$, $L = 511.9\ mm$, while the dimensions of the heat sink used in the present model are $D = 49.98\ mm$, $L = 511.9\ mm$, $d = 49.9799\ mm$, $t = 170\ mm$, $b = 171.9\ mm$, $N_f = 2$, $D/d = 1.000002$.

The length L and the diameter D of the heat sink are identical to that of the cylinder of Clemes, and the two geometries are nearly the same. The fin thickness t was set approximately equal to the fin spacing b. Although the values of b and t are arbitrarily selected, because $D/d \rightarrow 1$, the effect of fins on the total heat transfer is very small. If the fin thickness, the fin spacing and the fin number are set to other values, the model predictions will not change much.

Excellent agreement is observed in the comparison. The maximum difference between the model predictions and the circular cylinder data of Clemes is -2.6% and the RMS difference is only 1.2%.

Table 5.10: Results for Long Circular Cylinder of Clemes et al..

($L/D = 10.24$, $D/d = 1.000002$)

($b = 171.9\ mm$, $t = 170\ mm$, $N_f = 2$, $n = 1.0$)

Ra_D	Data of Clemes Nu_D	Present Model Nu_D	% Diff.
3.460×10^1	1.71	1.72	0.6
4.290×10^1	1.75	1.77	1.4
5.320×10^1	1.80	1.83	1.8
9.360×10^1	2.04	2.00	-1.9
1.155×10^2	2.12	2.07	-2.4
1.431×10^2	2.16	2.14	-0.8
2.150×10^2	2.30	2.30	-0.2
2.672×10^2	2.44	2.38	-2.4
3.300×10^2	2.53	2.47	-2.3
4.580×10^2	2.69	2.62	-2.6
5.700×10^2	2.76	2.73	-1.2
7.100×10^2	2.86	2.84	-0.7
9.390×10^2	3.00	2.99	-0.2
1.167×10^3	3.16	3.12	-1.3
1.453×10^3	3.25	3.25	0.1
1.900×10^3	3.43	3.43	-0.1
2.360×10^3	3.60	3.58	-0.6
2.930×10^3	3.71	3.74	0.7
3.860×10^3	4.01	3.95	-1.5
4.770×10^3	4.15	4.13	-0.6
5.900×10^3	4.33	4.31	-0.4
7.670×10^3	4.57	4.55	-0.4
9.500×10^3	4.80	4.76	-0.7
1.181×10^4	4.98	4.99	0.2
1.506×10^4	5.28	5.26	-0.4
1.868×10^4	5.52	5.51	-0.2
2.327×10^4	5.73	5.78	0.8

- More -

Table 5.10: (cont.) Results for Long Circular Cylinder of Clemes et al..

($L/D = 10.24$, $D/d = 1.000002$)

($b = 171.9\ mm$, $t = 170\ mm$, $N_f = 2$, $n = 1.0$)

Ra_D	Data of Clemes Nu_D	Present Model Nu_D	% Diff.
2.992×10^4	6.19	6.10	-1.4
3.700×10^4	6.52	6.40	-1.9
4.600×10^4	6.72	6.71	-0.1
5.880×10^4	7.24	7.09	-2.0
7.270×10^4	7.54	7.44	-1.3
9.020×10^4	7.82	7.81	-0.1
1.161×10^5	8.39	8.27	-1.4
1.434×10^5	8.77	8.68	-1.0
1.780×10^5	9.15	9.12	-0.3
2.256×10^5	9.79	9.63	-1.6
2.807×10^5	10.18	10.13	-0.5
3.510×10^5	10.72	10.67	-0.5
4.500×10^5	11.28	11.31	0.3
5.570×10^5	11.86	11.89	0.3
6.920×10^5	12.36	12.51	1.2
8.850×10^5	13.27	13.26	-0.1
1.097×10^6	13.92	13.95	0.2
1.368×10^6	14.52	14.70	1.2
1.781×10^6	16.05	15.65	-2.5
2.200×10^6	16.50	16.46	-0.2
2.727×10^6	17.38	17.33	-0.3
3.530×10^6	18.53	18.43	-0.5
4.350×10^6	19.68	19.38	-1.5
5.390×10^6	20.47	20.41	-0.3
6.910×10^6	21.80	21.67	-0.6
8.540×10^6	23.15	22.81	-1.5
1.061×10^7	24.19	24.04	-0.6

RMS Diff = 1.17%

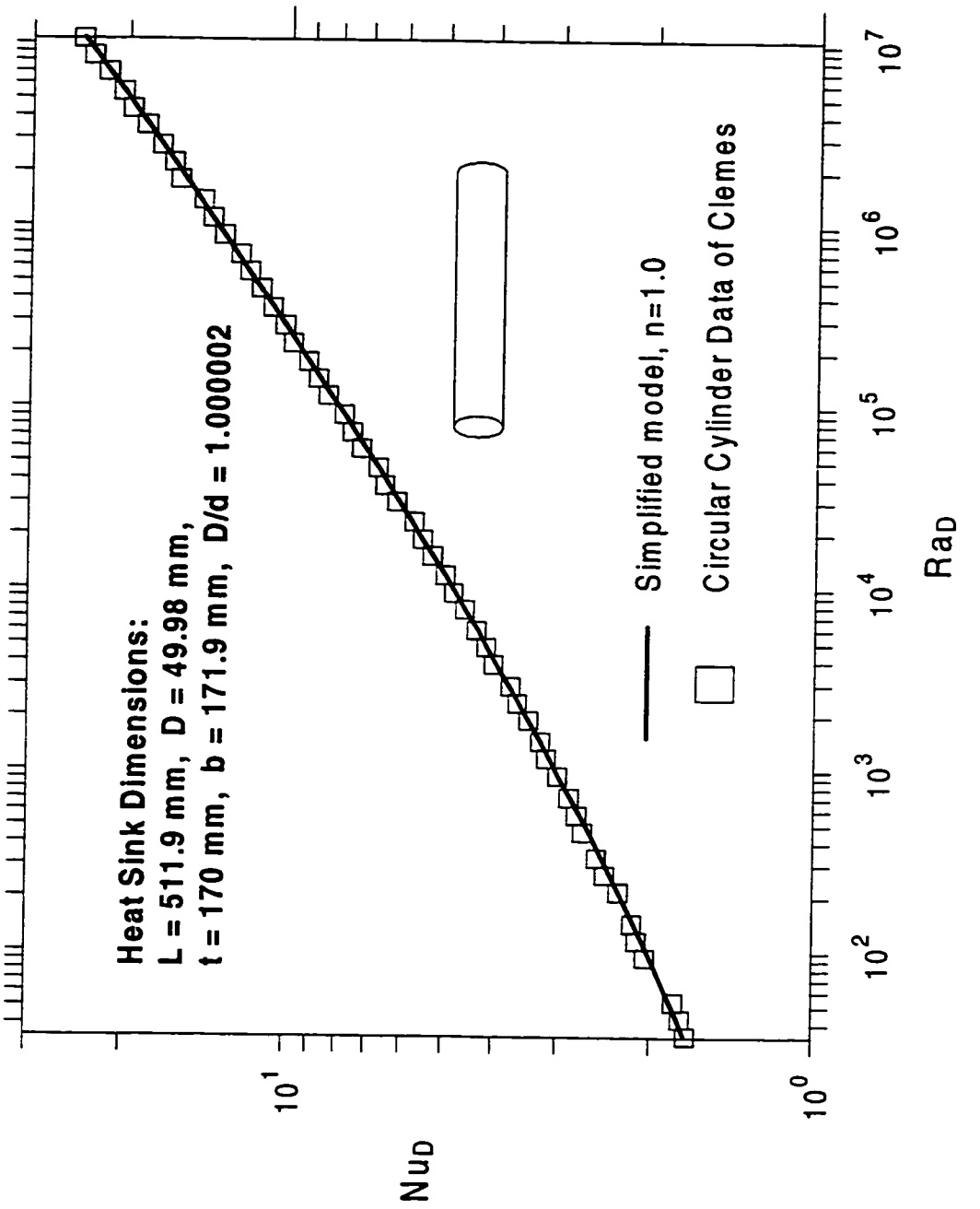

Figure 5.11: Comparison with Circular Cylinder Data of Clemes et al..

5.5.2 Short Circular Cylinder Data of Hassani and Hollands

The comparison between the present model and the short horizontal circular cylinder data of Hassani and Hollands (1989) is presented in Table 5.11 and Fig. 5.12. The dimensions of the circular cylinder are $D = 43\ mm$, $L = 43\ mm$, while those of the corresponding heat sink for the present model are $D = 43\ mm$, $L = 43\ mm$, $t = 15\ mm$, $b = 13\ mm$, N_f=2, $d = 42.997\ mm$, $D/d = 1.000023$.

The length L and the fin diameter D of the heat sink are identical to that of the cylinder of Hassani. Because $D/d \rightarrow 1$, variations in the fin thickness, the fin spacing and the fin number will not affect the model predictions much.

The agreement is also excellent, the maximum difference and the RMS difference are 4.4% and 2.4% respectively.

Table 5.11: Results for Short Circular Cylinder of Hassani and Hollands.

($L/D = 1$, $D/d = 1.00002$)

($b = 13\ mm$, $t = 15\ mm$, $N_f = 2$, $n = 1.0$)

Ra_D	Data of Hassani Nu_D	Present Model Nu_D	% Diff.
1.785×10^1	2.32	2.38	2.5
2.608×10^1	2.41	2.46	2.0
3.480×10^1	2.50	2.53	1.0
5.070×10^1	2.61	2.62	0.5
7.380×10^1	2.68	2.73	1.9
1.018×10^2	2.82	2.83	0.4
1.471×10^2	2.96	2.96	0.0
2.129×10^2	3.08	3.11	0.9
2.591×10^2	3.17	3.19	0.7
3.730×10^2	3.32	3.36	1.3
5.380×10^2	3.44	3.55	3.3
6.330×10^2	3.59	3.64	1.5
9.070×10^2	3.86	3.86	0.1
1.312×10^3	4.10	4.11	0.4
1.758×10^3	4.20	4.33	3.1
2.501×10^3	4.49	4.61	2.8
3.590×10^3	4.76	4.93	3.6
4.610×10^3	4.99	5.17	3.6
6.520×10^3	5.36	5.52	3.1
9.320×10^3	5.68	5.92	4.2
1.159×10^4	5.97	6.18	3.5

- More -

Table 5.11: (cont.) Results for Short Circular Cylinder of Hassani and Hollands.

$(L/D = 1,\ D/d = 1.00002)$

$(\ b = 13\ mm,\ t = 15\ mm,\ N_f = 2,\ n = 1.0)$

Ra_D	Data of Hassani Nu_D	Present Model Nu_D	% Diff.
1.623×10^4	6.40	6.60	3.2
2.298×10^4	6.78	7.08	4.4
2.889×10^4	7.19	7.41	3.1
4.020×10^4	7.72	7.93	2.7
5.660×10^4	8.20	8.51	3.8
7.580×10^4	8.81	9.05	2.7
1.041×10^5	9.46	9.67	2.2
1.445×10^5	10.05	10.37	3.2
1.937×10^5	10.77	11.05	2.6
2.596×10^5	11.53	11.77	2.1
3.520×10^5	12.23	12.58	2.9
5.100×10^5	13.33	13.66	2.4
6.690×10^5	14.21	14.51	2.1
8.860×10^5	15.04	15.45	2.7
1.272×10^6	16.45	16.77	1.9
1.619×10^6	17.51	17.71	1.2
2.082×10^6	18.52	18.76	1.3
3.037×10^6	20.33	20.46	0.7
3.790×10^6	21.50	21.54	0.2
4.780×10^6	22.64	22.73	0.4

RMS Diff = 2.43%

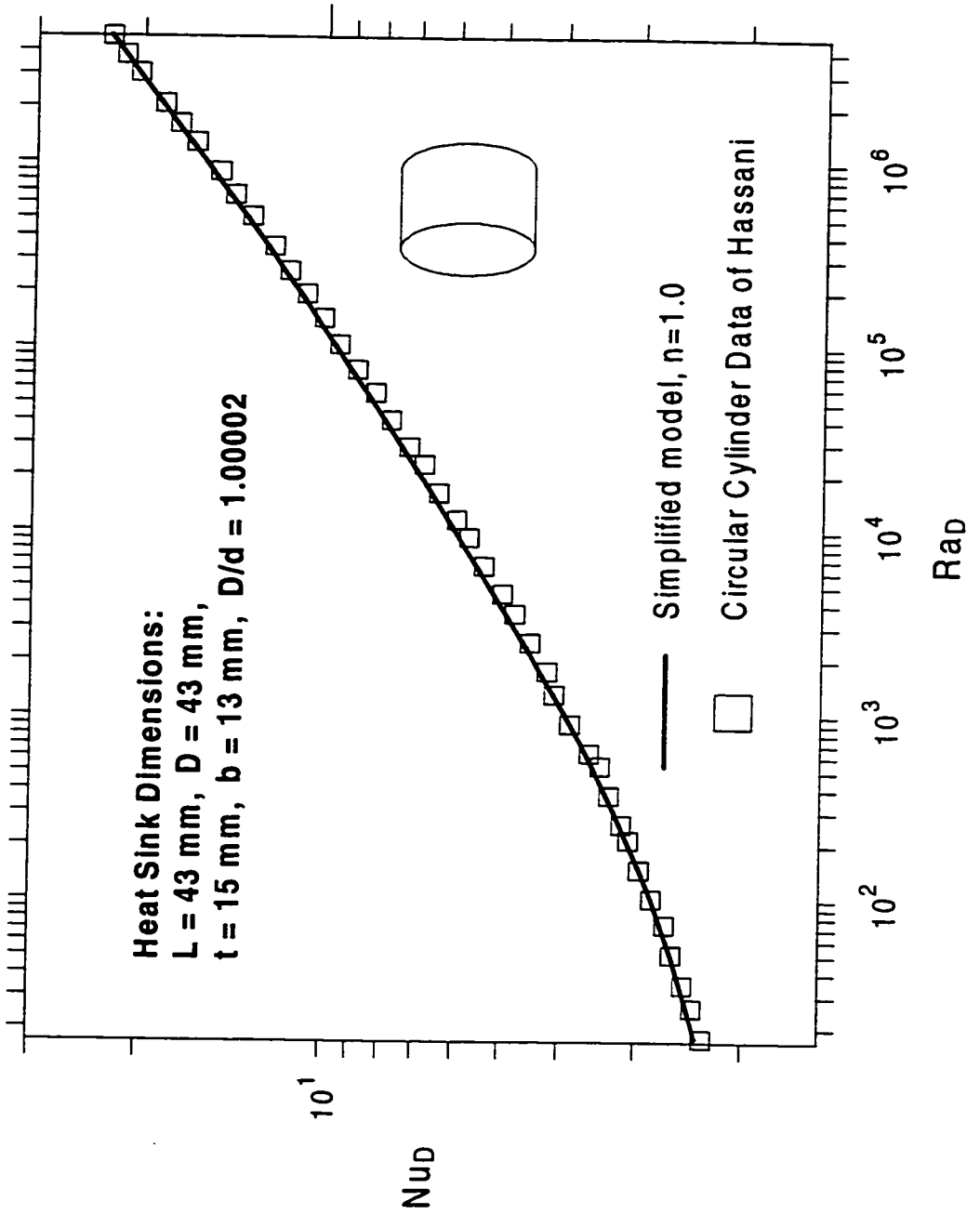

Figure 5.12: Comparison with Circular Cylinder Data of Hassani and Hollands.

5.5.3 Vertical Circular Disk Data of Hassani and Hollands

In Table 5.12 and Fig. 5.13 the present model is compared with the vertical thin circular disk data of Hassani and Hollands (1989). The dimensions of the disk are $D = 82\ mm$, $L = 8.2\ mm$ while the dimensions of the heat sink used for the model are $D = 82\ mm$, $L = 8.2\ mm$, $t = 3\ mm$, $b = 2.2\ mm$, $d = 81.999\ mm$, $D/d = 1.00002$, $N_f = 2$.

The maximum and the RMS differences are 15.8% and 8.2% respectively. In the range of $Ra_D = 896 \sim 8.7 \times 10^6$, the agreement is very good, but in the range of low Ra_D, the model gives higher predictions. The predictions of the Hassani-Hollands model for the circular disk were also plotted in the Fig. 5.13. Their correlation values are about $8 \sim 10\%$ higher than the experimental data at low Ra_b^*.

Table 5.12: Results for Vertical Thin Circular Disk of Hassani and Hollands.

$(L/D = 0.1,\ D/d = 1.00001)$

$(\ b = 2.2\ mm,\ t = 3\ mm,\ N_f = 2,\ n = 1.0)$

Ra_D	Data of Hassani Nu_D	Present Model Nu_D	% Diff.
2.847×10^1	3.11	3.60	15.8
4.240×10^1	3.25	3.72	14.5
6.290×10^1	3.34	3.85	15.4
8.640×10^1	3.35	3.97	18.5
1.277×10^2	3.61	4.12	14.3
1.899×10^2	3.82	4.30	12.6
2.259×10^2	3.89	4.38	12.6
3.320×10^2	4.10	4.58	11.6
4.880×10^2	4.27	4.79	12.2
6.130×10^2	4.42	4.93	11.5
8.960×10^2	4.72	5.17	9.6
1.317×10^3	4.98	5.45	9.4
1.720×10^3	5.18	5.66	9.2
2.503×10^3	5.50	5.97	8.6
3.660×10^3	5.76	6.32	9.8
4.380×10^3	6.02	6.50	7.9
6.300×10^3	6.42	6.88	7.2
9.140×10^3	6.78	7.32	7.9
1.068×10^4	7.08	7.51	6.1
1.498×10^4	7.55	7.96	5.4
2.119×10^4	7.97	8.45	6.1

- More -

Table 5.12: (cont.) Results for Vertical Thin Circular Disk of Hassani and Hollands.

($L/D = 0.1$, $D/d = 1.00001$)

($b = 2.2\ mm$, $t = 3\ mm$, $N_f = 2$, $n = 1.0$)

Ra_D	Data of Hassani Nu_D	Present Model Nu_D	% Diff.
2.644×10^4	8.37	8.80	5.1
3.670×10^4	8.95	9.34	4.3
5.140×10^4	9.47	9.94	5.0
6.440×10^4	10.02	10.38	3.6
8.870×10^4	10.71	11.04	3.1
1.234×10^5	11.34	11.78	3.9
1.635×10^5	12.17	12.46	2.4
2.185×10^5	13.00	13.22	1.7
2.951×10^5	13.78	14.06	2.0
4.050×10^5	14.73	15.02	2.0
5.290×10^5	15.73	15.90	1.1
7.000×10^5	16.67	16.87	1.2
1.066×10^6	18.56	18.49	-0.4
1.345×10^6	19.56	19.46	-0.5
1.710×10^6	20.51	20.52	0.0
2.608×10^6	22.42	22.56	0.6
3.143×10^6	23.60	23.54	-0.3
3.810×10^6	24.74	24.60	-0.6
6.460×10^6	28.19	27.78	-1.5
7.460×10^6	29.31	28.73	-2.0
8.660×10^6	30.33	29.75	-1.9

RMS Diff = 8.2%

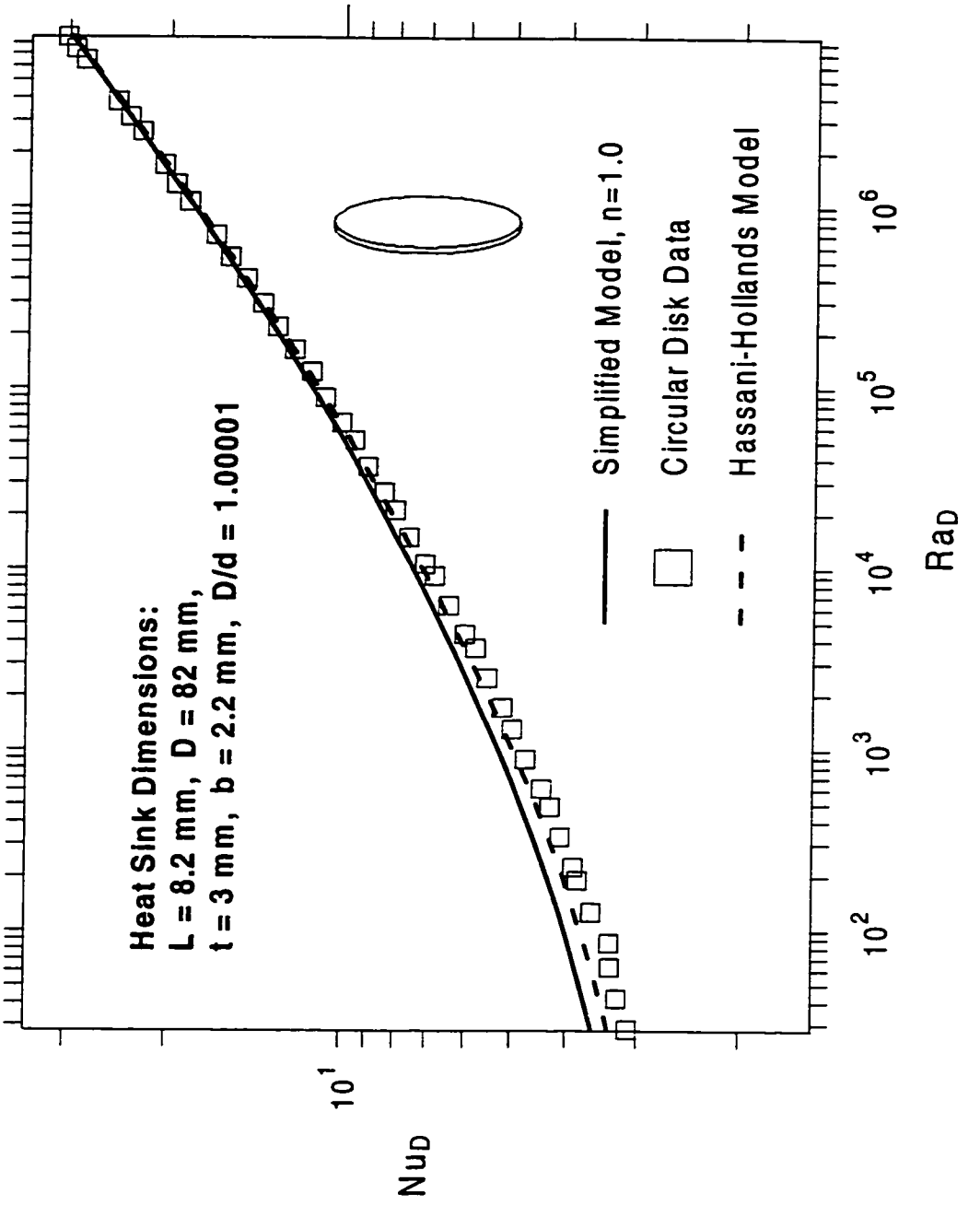

Figure 5.13: Comparison with Circular Disk Data of Hassani and Hollands.

5.6 Summary

The present model is compared with three previous correlations (Edwards and Chaddock, 1963; Jones and Nwizu, 1969; Tsubouchi and Masuda, 1970). Good agreement is observed in these comparisons. The present model also gives very good predictions for the present experimental data, while the previous correlations fail to predict the present data at low Ra_b^*, because they do not account for the effects of the end surfaces and the fin rim surfaces. For the previous data of an apple core (Hassani and Hollands, 1989), a circular disk, a short circular cylinder (Hassani and Hollands, 1989) and a long circular cylinder (Clemes et al., 1994), as well as correlations of channel flow (Elenbaas, 1942; Tsubouchi and Masuda, 1970, Raithby and Hollands, 1985), the present model shows good to excellent agreement.

The comparisons show that the present model can be used for arbitrary dimensions of the heat sinks; and it can be applied to the two cases described in the dimensional analysis in Chapter 4. In one case, the geometry of the heat sink is fixed, Ra_b^* varies with Ra_D, in the other case, Ra_D is fixed, Ra_b^* varies with b/D.

Chapter 6

Summary and Conclusions

A study was carried out on natural convection heat transfer from isothermal, horizontal cylinders with annular fins to establish a comprehensive model which accounts for all geometric parameters and surface components. The heat sinks used in this study were machined from aluminum alloy cylindrical bar stock. The fins were an integral part of the support cylinder with no joints or contact resistance.

A literature review is given in Chapter 2. Several previous studies on annular-fin heat sinks and rectangular fin arrays are examined. It was found that the previous correlations do not include the effects of end surfaces and the fin thickness. Relevant experimental methods and boundary layer solutions are briefly reviewed.

The experimental work of this study includes:

- Measurement of radiative heat transfer from each of the test heat sinks in a vacuum chamber.

- Measurement of natural convection heat transfer from each of the test heat sinks.

- A calculation procedure was developed to estimate wire heat losses in both radiation and natural convection measurements. Subtraction of these wire heat losses resulted in more accurate values of heat transfer from the heat sink.

- Data reduction.

– Uncertainty analysis for the experimental results.

The experimental method was verified by comparison with the results of a established method.

In Chapter 4, an existing solution for laminar natural convection is briefly reviewed; and an approximate solution for fully developed flow between fins is obtained. Based on the existing solution for laminar natural convection, the fully developed flow solution, and making the distinction between the external and internal surfaces of the heat sink, a general model for laminar natural convection heat transfer from isothermal, horizontal cylinders with annular fins is developed. In order to make the model easier to use, a simplified model is also presented which is easy to use and gives very good predictions.

To account for the radiative heat transfer, a radiation model for the heat sinks is presented which showed good agreement with the radiation measurements. A fin efficiency formula for annular fins is also given in the chapter for application to nonisothermal fin surfaces.

In Chapter5, the simplified present model is compared with previous correlations, present experimental data, and previous experimental data. The comparisons with previous correlations for D/d=1.94 show good agreement between the present model and the Jones-Nwizu correlation. The maximum difference is 9.8% and the RMS difference is 5.4%. For the diameter ratio D/d=2.97, good agreement is observed between the Tsubouchi-Masuda correlation and the present model. The maximum and the RMS differences are 13.7% and 8.7%, respectively. For the diameter ratio D/d=5.17, good agreement is shown between the Edwards-Chaddock correlation for aluminum fin and the present model. The maximum difference is 11.5% and the RMS difference is 8.1%.

The comparison of the present model with the present experimental data shows very good agreement, with a maximum difference of 6.2% and an RMS difference

of 4.3%. The previous correlations fail to predict the experimental data at low Ra_b^*, because they do not take into consideration the effects of fin thickness and end surfaces.

In the comparison with the apple core data of Hassani and Hollands (1989), the present model shows good agreement, with a maximum difference of 11.6% and an RMS difference of 5.9%.

In the limiting case of $D/d >> 1$, i.e. when the support cylinder diameter shrinks, the inner surface of the heat sink is considered as a circular-disk channel. the present channel model shows very good agreement with the Tsubouchi-Masuda. Elenbaas and Raithby-Hollands correlations.

In the other limiting case, i.e. $D/d \rightarrow 1$ the heat sink becomes a solid cylinder. the present model shows excellent agreement with the long circular cylinder data of Clemes et al. (1994) and the short circular cylinder data of Hassani and Hollands (1989). In the comparison with the vertical thin circular disk data of Hassani and Hollands (1989), the present model shows good agreement in the range of $Ra_D = 896$ to 8.7×10^6, but larger deviations are observed at low Ra_D.

The comparisons show that the present model can be used for arbitrary dimensions of the heat sinks.

References

1. Acrivos, A (1960), "A Theoretical Analysis of Laminar Natural Convection Heat Transfer to Non-Newtonian Fluids," AIChE Journal, Vol. 6, No 4, pp. 584-590.

2. Bar-Cohen, A., and Rohsenow, W.M. (1984), "Thermally Optimum Spacing of Vertical, Natural Convection Cooled, Parallel Plates," ASME Journal of Heat Transfer, Vol. 106, pp. 116-123.

3. Bejan, A. (1993), "Heat Transfer," John Wiley & Sons, Inc.

4. Brundrett, E. (1998), Personal communication.

5. Churchill, S.W. and Usagi, R. (1972), "A General Expression for the Correlation of Rates of Transfer and Other Phenomena," AIChE Journal Vol. 18, pp. 1121 - 1128.

6. Churchill, S.W. and Churchill, R.U. (1975), "A Comprehensive correlating Equation for Heat and Component Transfer by Free Convection," AIChE Journal, Vol. 21, pp. 604-606.

7. Clemes, S. B. (1990), "Free Convection Heat Transfer from Two Dimensional Bodies," M.A.Sc. Thesis, Mech. Eng. Dept., University of Waterloo.

8. Clemes, S. B., Hollands, K. G. T. and Brunger, A. P. (1994), " Natural Convection Heat Transfer from Long Horizontal Isothermal Cylinders," J. Heat Transfer, Vol. 116, pp. 96-104.

9. Edwards, J. A. and Chaddock, J. B. (1963), "An Experimental Investigation of the Radiation and Free- Convection Heat Transfer from a Cylindrical Disk Extended Surfaces," Trans. ASHRAE, Vol. 69, pp. 313 - 312.

10. Elenbaas, W. (1942), "Heat Dissipation of Parallel Plates by Free Convection," Physica, Vol. IX, No. 1, pp. 1 - 28.

11. Geremia, J. (1988), "Experiments in Fluid Mechanics," Appendix C, Editor: R.A. Granger, Holt, Rinehart and Winston, Inc.

12. Hahne, E. and Zhu, D. (1994), "Natural Convection Heat Transfer on Finned Tubes in Air," Int. J. Heat Mass Transfer, Vol. 37, Suppl. 1, pp. 59 - 63.

13. Hassani, A. (1987), "An Investigation of Free Convection Heat Transfer from Bodies of Arbitrary Shape," Ph.D. Thesis, University of Waterloo.

14. Hassani, A. V. and Hollands, K. G. T. (1989), "On Natural Convection Heat Transfer from Three-Dimensional Bodies of Arbitrary Shapes." J. Heat Transfer, Vol. 111, pp. 363-371.

15. Hollands, K. G. T. (1988), "Direct Measurement of Gaseous Natural Convective Heat Fluxes," First World Conference on " Experimental Heat Transfer, Fluid Mechanics and Thermodynamics," Dubrovnik, Yugoslavia, Sept. 4-9, pp. 160-168.

16. Incropera, F. P. and DeWitt, D. P. (1990), "Fundamentals of Heat and Mass Transfer," 3rd. Ed., John Wiley & Sons, Inc.

17. Jafarpur, K. (1992), "Analytical and Experimental Study of Laminar Free Convective Heat Transfer From Isothermal Convex Bodies of Arbitrary Shape." Ph.D. Thesis, University of Waterloo.

18. Jones, C. D. and Nwizu, E. I. (1969), "Optimum Spacing of Circular Fins on Horizontal Tubes for Natural Convection Heat Transfer," ASHRAE Symp. Bull. DV-69-3, pp. 11 - 15.

19. Karagiozis, A. N. (1991), "An Investigation of Laminar Free Convection Heat Transfer from Isothermal Finned Surfaces," Ph.D. Thesis, University of Waterloo.

20. Karagiozis, A., Raithby, G. D. and Hollands, K. G. T. (1994), " Natural Convection Heat Transfer from Arrays of Isothermal Triangular Fins in Air," J. Heat Transfer, Vol. 116, pp. 105-111.

21. Kayansayan, N. and Karabacak, R. (1992), "Natural Convection Heat Transfer Coefficient for A Horizontal Cylinder with Vertically Attached Circular Fins," Heat Recovery Systems & CHP, Vol. 12, No. 6 pp. 457 - 468.

22. Knudsen, J. G. and Pan, R. B. (1963), "Natural Convection Heat Transfer from Transverse Finned Tubes," Chemical Engineering Progress, Vol. 59, No. 7, pp. 45 - 50.

23. Kuzman Raznjevic (1976), "Handbook of Thermodynamic Tables and Charts," Translated by Dr. Marijan Boskovic, Hemisphere Publishing Corporation, pp. 309.

24. Langmuir, I. (1912), "Convection and Conduction of Heat in Gases," Phys. Rev., Vol. 34, pp. 401-422.

25. Lee, S., Yovanovich, M.M. and Jafarpur, K. (1991), "Effects of Geometry and Orientation on Laminar Natural Convection from Isothermal Bodies," J. Thermophysics and Heat Transfer, Vol. 5, No 2, pp. 208-216.

26. Li, H.H. and Chung, B.T.F. (1996), "A New Look at Natural Convection from Isothermal, Vertical Parallel Plates," HTD-Vol. 333, Proceedings of the ASME Heat Transfer Division, Vol. 2, pp. 249-256.

27. Martin, L., Raithby, G. D. and Yovanovich, M. M. (1991), "On the Low Rayleigh Number Asymptote for Natural Convection Through an Isothermal. Parallel-Plate Channel," J. Heat Transfer, Vol. 113, pp. 899 - 905.

28. McAdams, W. H. (1954), "Heat Transmission," 3rd. Ed., McGraw - Hill. New York.

29. Moffat, R.J. (1988), "Describing the Uncertainties in Experimental Results." Experimental Thermal and Fluid Science, No. 1, pp. 3-17.

30. Raithby, G. D. and Hollands, K. G. T. (1975), "A General Method of Obtaining Approximate Solutions to Laminar and Turbulent Free Convection Problems," Advances in Heat Transfer, Vol 11, Academic Press. New York pp. 264 - 315.

31. Raithby, G. D. and Hollands. K. G. T. (1976), "Laminar and Turbulent Free Convection from Elliptic Cylinders, with A Vertical Plate and Horizontal Circular Cylinder as Special Cases," J. Heat Transfer, February. pp. 72-80.

32. Raithby, G. D., Pollard, A. , Hollands, K. G. T. and Yovanovich. M.M. (1976), "Free Convection Heat Transfer from Spheroids," J. Heat Transfer, Vol. 98, pp. 452-458.

33. Raithby, G. D. and Hollands, K. G. T. (1978), "Analysis of Heat Transfer by Natural Convection (or Film Condensation) for Three Dimensional Flows." Proc. 6th Heat Transfer Conf., Toronto, Vol. 2, pp. 187 - 192.

34. Raithby, G. D. and Hollands, K. G. T. (1985), "Handbook of Heat Transfer Fundamentals," Second Edition, Chapter 6, Eds: Hartnett and Ganic, McGraw-Hill, New York.

35. Siegel, R. and Howell, J.R. (1992), "Thermal Radiation Heat Transfer," 3rd. Ed. Hemisphere Publishing Corporation.

36. Smythe, W. R. (1956), "Charged Right Circular Cylinder," *Journal of Applied Physics*, Vol. 27, No. 8, pp. 917-920.

37. Smythe, W. R. (1962), "Charged Right Circular Cylinder," *Journal of Applied Physics*, Vol. 33, No. 10, pp. 2966-2967.

38. Sparrow, E. M. and Chrysler, G. M. (1981), "Natural Convection Heat Transfer Coefficients for a Short Horizontal Cylinder Attached to A Vertical Plate," J. Heat Transfer, Vol. 103, 1981, pp. 630 - 637.

39. Stewart, W. E. (1971), "Asymptotic Calculation of Free Convection in Laminar Three-Dimensional Systems," Int. J. Heat Mass Transfer. Vol. 14. pp. 1013-1031.

40. Tsubouchi, T. and Masuda, H. (1970), "Natural Convection Heat Transfer from Horizontal Cylinders with Circular Fins," Proc. 6th Int. Heat Transfer Conf. Paper NC 1.10, Paris, pp. 1 - 11.

41. Wang, C.-S. (1993), "Surface Element Methods Based on Ring Sources and Line Sources for Accurate Calculations of Shape Factors for Arbitrary Isothermal Axisymmetric Surfaces and Some Two Dimensional Problems," M.A.Sc. Thesis, Mech. Eng. Dept., University of Waterloo.

42. Yovanovich, M.M. (1987a), "New Nusselt and Sherwood Numbers for Arbitrary Isopotential Geometries at Zero Peclet and Rayleigh Numbers," AIAA Paper No. 87-1643, AIAA 22nd Thermophysics Conference, June 8-10, Honolulu, Hawaii.

43. Yovanovich, M.M. (1987b), "Natural Convection from Isothermal Spheroids in the Conductive to Laminar Flow Regimes," AIAA-87-1587, AIAA 22nd Thermophysics Conference, Honolulu, Hawaii, June 8-10.

44. Yovanovich, M.M. (1987c), "On the Effect of Shape, Aspect Ratio and Orientation Upon Natural Convection from Isothermal Bodies of Complex Shapes," ASME National Heat Transfer Conference, Boston, MA, December 13-18, HTD-Vol. 82, pp. 121-129.

45. Yovanovich, M.M. and Wang, C.-S. (1992), "Surface Element Method Based on Ring Sources for Accurate Calculation of Shape Factors of Complex Axisymmetric Bodies," AIAA-92-2938, AIAA 27th Thermophysics Conference, Nashville, TN, July 6-8.

46. Yovanovich, M.M. (1995), "Formulation of One-Dimensional Conduction in Orthogonal Curvilinear Coordinates: Application to Extended Surfaces," AIAA-95-2043, AIAA 30th Thermophysics Conference, San Diego, CA, June 19-22.

Appendix A

Test Heat Sinks

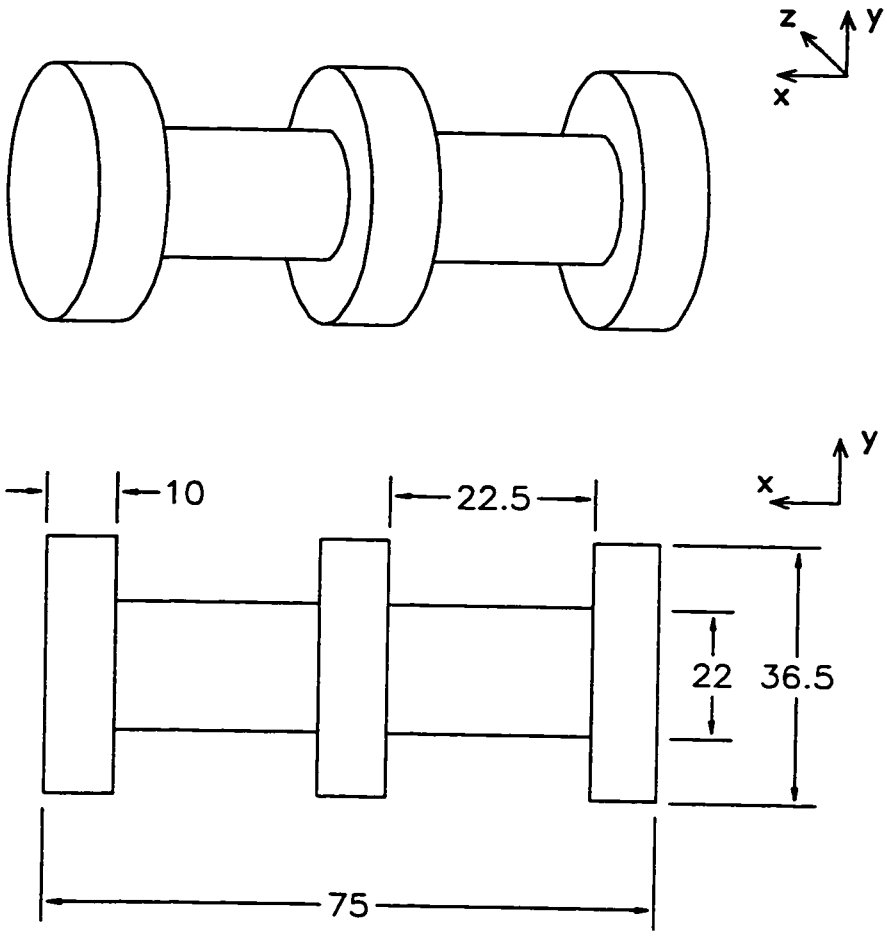

Figure A.1: Heat Sink A (unit: mm).

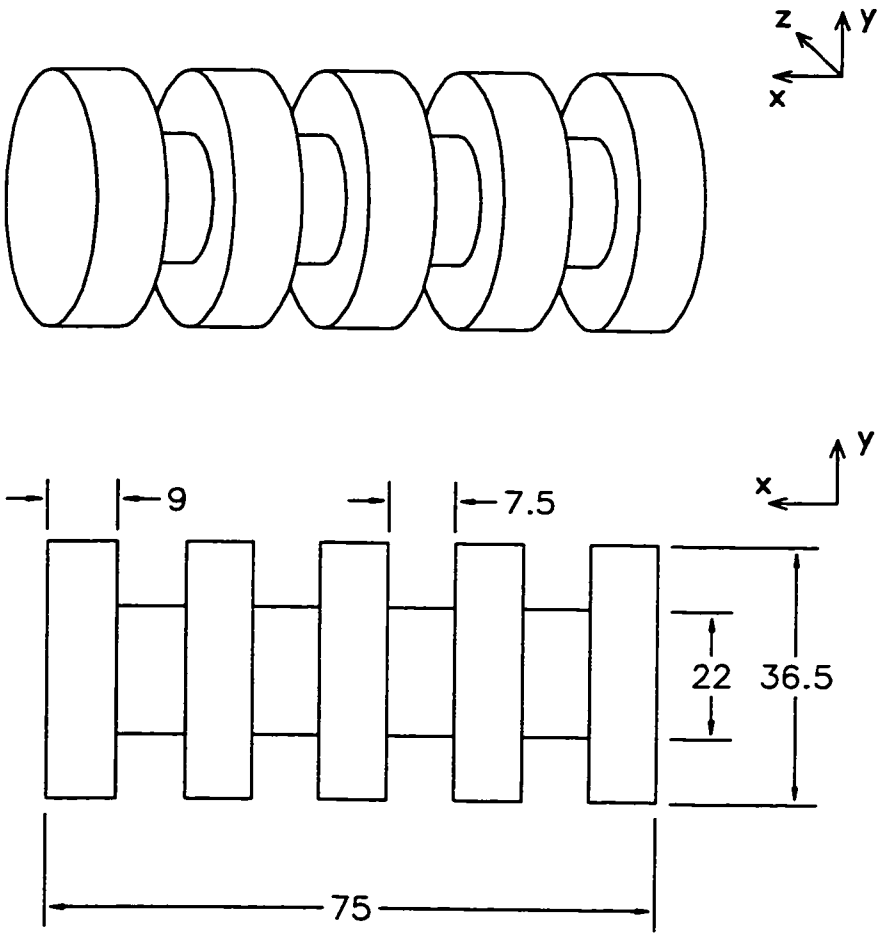

Figure A.2: Heat Sink B (unit: mm).

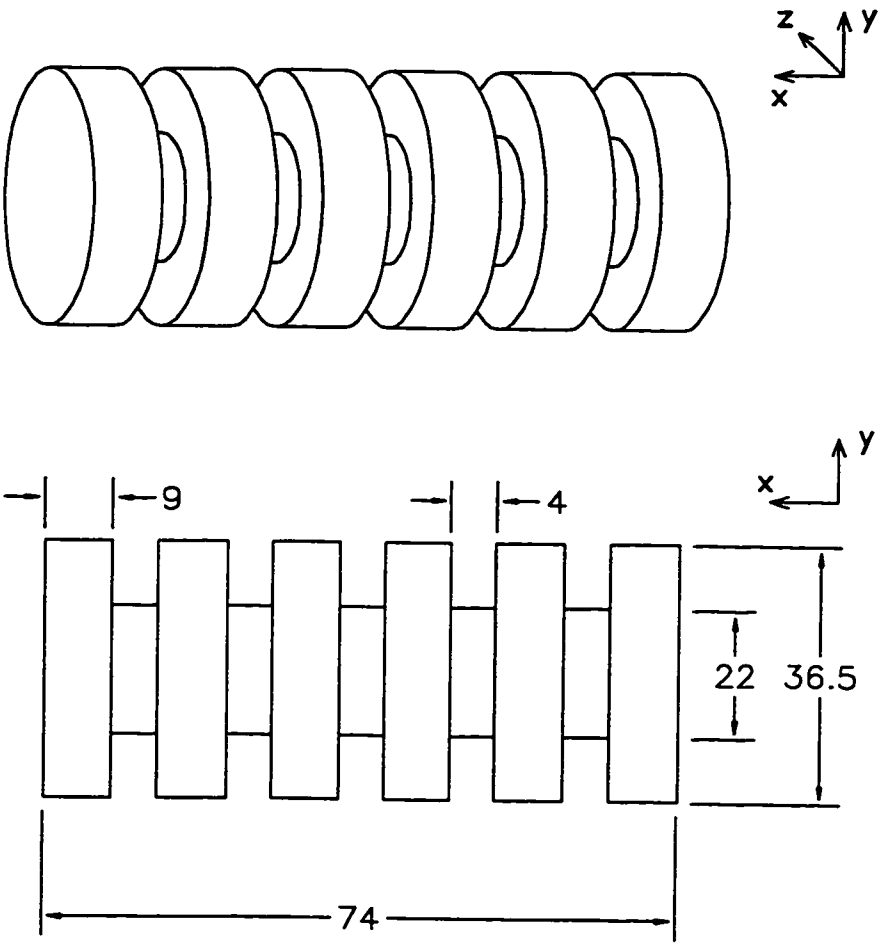

Figure A.3: Heat Sink C (unit: mm).

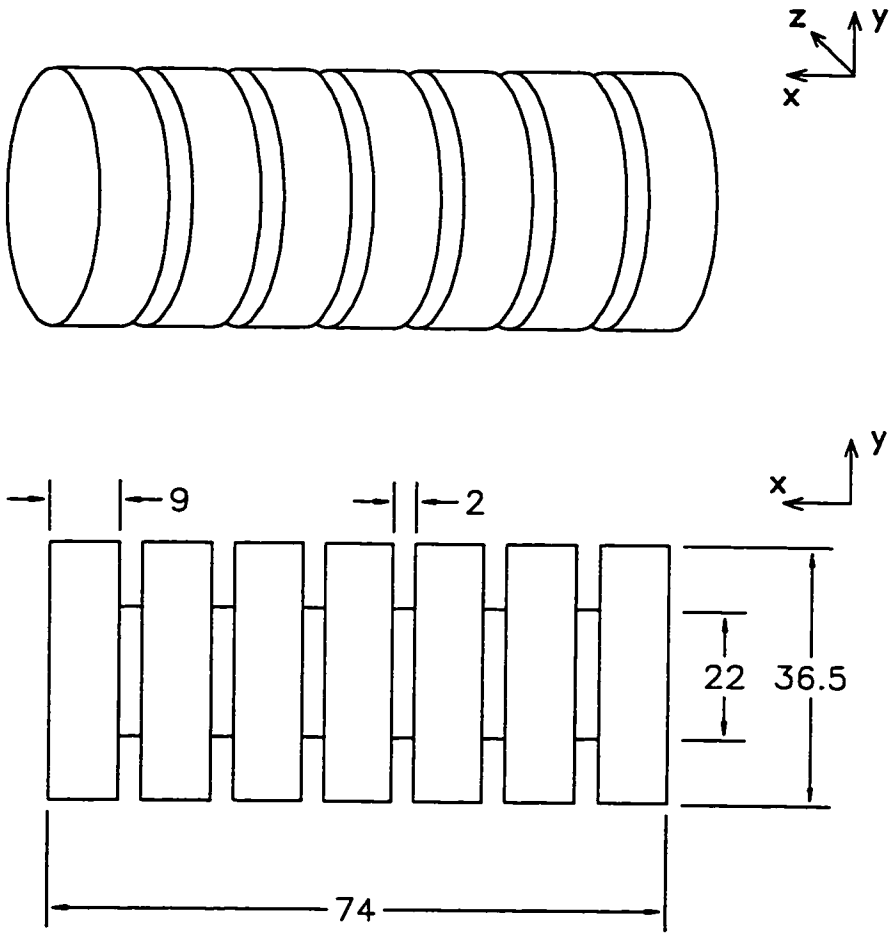

Figure A.4: Heat Sink D (unit: mm).

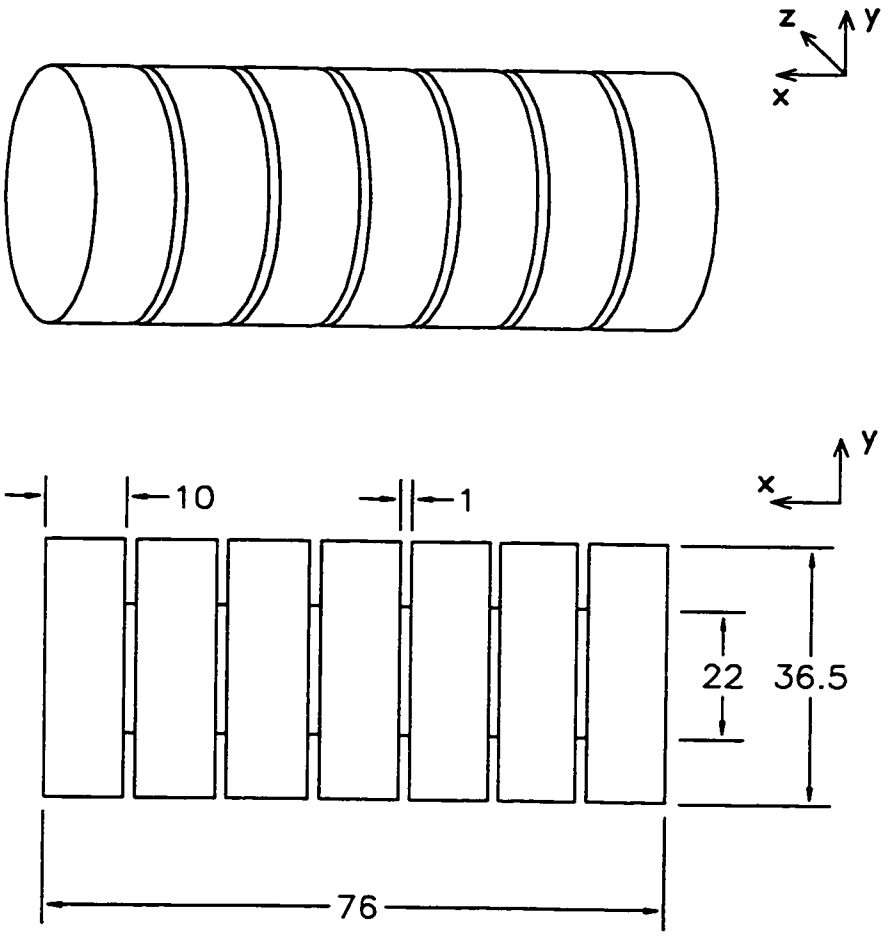

Figure A.5: Heat Sink E (unit: mm).

Appendix B

Estimation of Additional Wire Heat Loss

In the convection heat transfer measurement the wire heat loss for the same heat sink is different from that in the radiation heat transfer measurement. The following sections give the estimation for the difference between the two wire heat losses.

B.1 Heat Transfer Through a Pin Fin of Uniform Cross Section

The heat transfer through a wire attached to the test heat sink is assumed the same as that through a pin fin with uniform cross section as shown in Fig. B.1.

In this figure, q_f is the heat flow rate through the base of pin fin; k is the conductivity of the pin fin; A_C is the cross section area of the pin fin; r_1 is the radius of the pin fin; h is the overall heat transfer coefficient between the pin fin surface and the ambient; P is the perimeter and L is the length of the pin fin.

In the present experiments, the wire attached to the test heat sink can be considered as a pin fin with infinite length. In this case the effective length of the

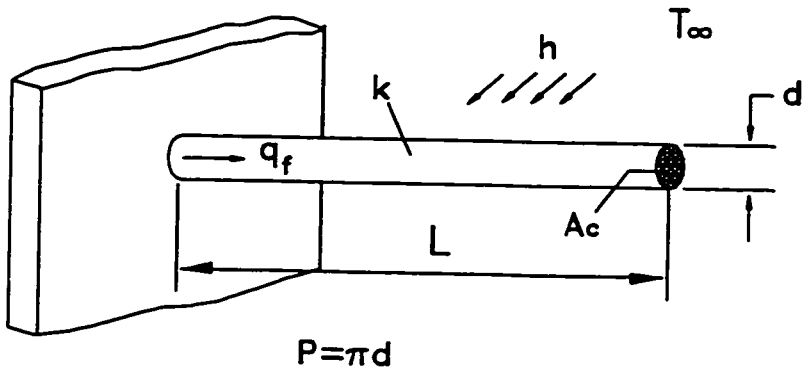

Figure B.1: Pin Fin with Uniform Cross Section.

fin, L_e, can be found by (Incropera and DeWitt, 1990)

$$L_e = 2.65 \sqrt{\frac{kA_C}{hP}} \tag{B.1}$$

and the heat flow rate through the base section of the pin fin, q_f, can be calculated by (Incropera and DeWitt, 1990)

$$q_f = \sqrt{hPkA_C}\,\Delta T \tag{B.2}$$

where ΔT is the temperature difference between the base section and the ambient or that between the heat sink surface and the ambient as used in the following sections.

B.2 Average Surface Temperature for Effective Length

From the definition of heat transfer coefficient and Eq. (B.2), we have

$$\begin{aligned} h &= \frac{q_f}{A\,\Delta\overline{T}} \\ &= \frac{\sqrt{hPkA_C}\,\Delta T}{A\,\Delta\overline{T}} \end{aligned} \tag{B.3}$$

where $\Delta\overline{T}$ is the average surface temperature difference between the wire surface and the ambient for the effective length; A is the surface area of the effective length which can be expressed as

$$\begin{aligned} A &= PL_e \\ &= P\,2.65\sqrt{\frac{kA_C}{hP}} \\ &= 2.65\sqrt{\frac{PkA_C}{h}} \end{aligned} \tag{B.4}$$

Inserting Eq. (B.4) into Eq. (B.3), the average surface temperature difference of the effective length is obtained as

$$\Delta\overline{T} = \frac{\Delta T}{2.65} \tag{B.5}$$

Finally the average surface temperature of the wire surface for the effective length can be found:

$$\overline{T} = T_\infty + \frac{\Delta T}{2.65} \tag{B.6}$$

B.3 Effective Heat Transfer Coefficient for Radiation

From the radiative heat transfer equation, we have the following approximation:

$$Q_{WR} = \epsilon\sigma A(\overline{T}^4 - T_\infty^4) \tag{B.7}$$

where Q_{WR} is the heat transfer rate for wire radiation, $\overline{T}$ is the average surface temperature of the wire, $(T_\infty + \Delta T/2.65)$, ϵ is surface emissivity, σ is Stefan-Boltzmann constant. The radiation heat transfer coefficient for the wire, h_R, can be expressed as

$$h_R = \epsilon\sigma(\overline{T} + T_\infty)(\overline{T}^2 + T_\infty^2) \tag{B.8}$$

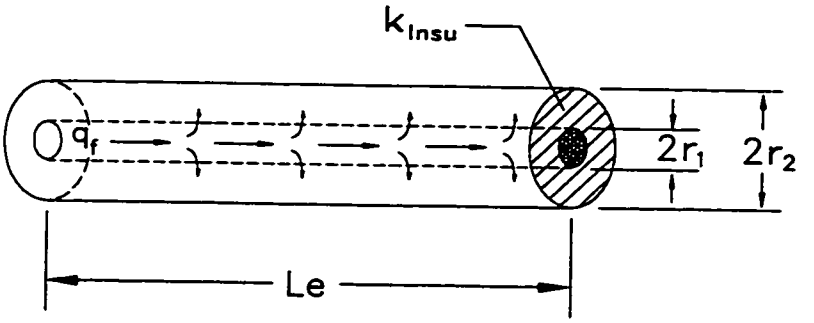

Figure B.2: Heat Transfer Through Wire.

For instance, if $\Delta T = 48.5K$, $T_\infty = 293K$ and $\epsilon = 0.95$, the following results will be obtained. The insulation layer is glass fiber, its ϵ could not be found by the author. Therefore the high value of smooth glass emissivity ($\epsilon = 0.9 - 0.95$, Incropera and Dewitt, 1990) is taken as the emissivity of the glass fiber, because glass fiber has a rough surface which will enhance the emissivity. The following calculation shows that this approximation does not introduce much deviation.

$$\begin{aligned} \overline{T} &= 293 + 48.5/2.65 \\ &= 311\ K \end{aligned}$$

and thus

$$h_R = 5.9\ \ W/m^2K$$

The thermal resistance for the surface radiation of the effective length of the pin fin can be expressed as

$$R_R = \frac{1}{h_R 2\pi r_2 L_e} \tag{B.9}$$

With reference to Fig. B.2, the thermal resistance of the insulation layer is

$$R_{Insu} = \frac{\ln(r_2/r_1)}{2\pi k_{Insu} L_e} \tag{B.10}$$

where k_{Insu} is the conductivity of the insulation layer.

If the overall heat transfer coefficient from the metal wire surface to the ambient is h_{Tot1} based on the metal wire surface area, the corresponding thermal resistance will be

$$R_{Tot1} = \frac{1}{h_{Tot1} 2\pi r_1 L_e} \tag{B.11}$$

From the relationship of

$$R_{Tot1} = R_{Insu} + R_R \tag{B.12}$$

the overall heat transfer coefficient h_{Tot1} is obtained:

$$h_{Tot1} = \frac{1}{\frac{r_1}{r_2 h_R} + \frac{r_1}{k_{Insu}} \ln(r_2/r_1)} \tag{B.13}$$

Then the radiation loss from the wire, q_R, can be found using Eq. (B. 2):

$$q_R = \sqrt{h_{Tot1} P k A_C}\ \Delta T \tag{B.14}$$

and the effective length of the wire, L_e, can be found using Eq. (B.1):

$$L_e = 2.65 \sqrt{\frac{k A_C}{h_{Tot1} P}} \tag{B.15}$$

For example, if $r_1 = 0.3\ mm$, $r_2 = 1\ mm$, $k = 67.49\ W/mK$ (Nickel 200) and $k_{Insu} = 0.035\ W/mK$ for glass fiber (Bejan, 1993), the overall heat transfer coefficient at the metal wire surface, h_{Tot1}, will be

$$h_{Tot1} = 16.3\ W/m^2K \tag{B.16}$$

the wire radiative loss will be

$$q_R = 0.038\ W \tag{B.17}$$

and the effective length of the wire will be

$$L_e = 6.6\ cm \tag{B.18}$$

From this result, it can be seen that in the radiation test the heat loss conducted along the wire is then also dissipated by radiation.

Discussion:

In the above procedure the $\overline{T}$ of Eq. (B.8) is the average temperature for the metal wire surface, instead of that for the insulation layer surface, therefore the h_R from Eq. (B.8) is the first order approximation. Through the calculation for temperature drops at the two thermal resistors, R_{Insu} and R_R which are connected in series, a better value of $\overline{T}$ for the insulation layer surface can be found. Then new values of h_R and R_R can be obtained, and the value of $\overline{T}$ can be further improved by iteration. But in the present experiment the first order approximation of h_R is satisfactory. In fact, the first order approximation differs by less than 1% from the value improved by the iteration.

B.4 Estimation of Convection Heat Transfer Coefficient

With the average surface temperature for the effective length obtained in section B2, the Nusselt number of the wire can be estimated using one of available solutions for isothermal, horizontal circular cylinders. In the following, Raithby and Hollands (1985) formula for this problem will be adopted.

The outer diameter of the insulation layer is taken as the characteristic length, and the Rayleigh number is

$$Ra_{d_2} = \frac{g\beta\Delta\overline{T}d_2^3}{\nu\alpha} \tag{B.19}$$

where $\Delta\overline{T} = \Delta T/2.65$, $d_2 = 2r_2$ and $\overline{T}$ is taken as the surface temperature.

The Nusselt number is

$$Nu_{d_2} = \frac{2f}{\ln(1 + 2f/Nu^T)} \tag{B.20}$$

with

$$Nu^T = 0.772\ \overline{C}_l\ Ra_{d_2}^{1/4} \tag{B.21}$$

where $\overline{C}_l = 0.515$ and

$$f = 1 - \frac{0.13}{(Nu^T)^{0.16}} \tag{B.22}$$

From Eq.(B.20) the heat transfer coefficient for the wire surface can be found:

$$h_{Conv} = \frac{2f}{\ln(1 + 2f/Nu^T)} \frac{k_f}{d_2} \tag{B.23}$$

where k_f is the conductivity of the air.

For the above example, if $\Delta T = 48.5\ K$ and $T_\infty = 293\ K$, then $\Delta\overline{T} \approx 18\ K$, $Ra_{d_2} = 16.8$ and $Nu^T = 0.8$. The heat transfer coefficient, h_{Conv}, is

$$h_{Conv} = 18.1\ W/m^2K \tag{B.24}$$

B.5 Effective Heat Transfer Coefficient for Both Radiation and Convection

The heat transfer coefficient on the insulation layer surface for both radiation and convection, $h_{R,Conv}$, is

$$h_{R,Conv} = h_R + h_{Conv} \tag{B.25}$$

For the above instance,

$$h_{R,Conv} = 24\ W/m^2K \tag{B.26}$$

The thermal resistance corresponding to this coefficient is

$$R_{R,Conv} = \frac{1}{h_{R,Conv} 2\pi r_2 L_e} \tag{B.27}$$

If the effective heat transfer coefficient based on the metal wire surface is h_{Tot2}, the total thermal resistance will be

$$R_{Tot2} = \frac{1}{h_{Tot2} 2\pi r_1 L_e} \tag{B.28}$$

From the relationship:

$$R_{Tot2} = R_{Insu} + R_{R,Conv} \tag{B.29}$$

the effective heat transfer coefficient h_{Tot2} can be found:

$$h_{Tot2} = \frac{1}{\frac{r_1}{r_2 h_{R,Conv}} + \frac{r_1}{k_{Insu}} \ln(r_2/r_1)} \tag{B.30}$$

For the above instance,

$$h_{Tot2} = 43.8\ W/m^2K \tag{B.31}$$

Then the radiation and convection loss from the wire, $q_{R,Conv}$, can be found using Eq. (B.2):

$$q_{R,Conv} = \sqrt{h_{Tot2} P k A_C}\ \Delta T \tag{B.32}$$

For the instance,

$$q_{R,Conv} = 0.06\ W \tag{B.33}$$

Discussion:

In the above procedure the $\Delta\overline{T}$ used in Eq. (B.19) is the temperature difference between the metal wire surface and the ambient, instead of that between the insulation layer surface and the ambient, therefore the h_{Conv} from Eq (B.23) is just the first order approximation. Through the calculation for temperature drops at the two thermal resistors, R_{Insu} and $R_{R,Conv}$ which are connected in series, a better value of $\Delta\overline{T}$ between the insulation layer surface and the ambient can be found. Then new values of h_{Conv} and $R_{R,Conv}$ can be obtained, and the value of $\Delta\overline{T}$ can be further improved by the iteration. But in the present experiment the first order approximation of h_{Conv} is satisfactory. Actually, the first order approximation differs by less than 2% from the value improved by the iteration.

B.6 Additional Wire Heat Loss

The additional wire heat loss ΔQ_{WIR} in convection heat transfer measurement is obtained as

$$\Delta Q_{WIR} = (q_{R,Conv} - q_R)\, N_{WIR} \tag{B.34}$$

where N_{WIR} is the number of wires attached to the test heat sink.

For the above instance with four wires,

$$\Delta Q_{WIR} = 0.092\ W \tag{B.35}$$

The power supplied to the heater embedded inside the heat sink is 5.04 W for this instance, therefore the additional wire heat loss accounts for 1.8% of the total heat dissipation.

Appendix C

Uncertainty Analysis

C.1 Methodology

The overall uncertainty of the experimental results is estimated using the procedure outlined by Moffat (1988) and Geremia (1988). In the method, the result R of an experiment is assumed to be calculated from a set of measurements and it is represented by

$$R = R(X_1, X_2, X_3, \cdots, X_N) \tag{C.1}$$

For multiple-sample measurements, each measurement has its known bias limit and the precision index of the mean of the sample, and the number of degrees of freedom for each precision index is known.

In the following analysis, the uncertainty for each measurement is calculated first and then the uncertainties of all measurements are combined to give the overall uncertainty in the result R.

The effect of the uncertainty in each measurement X_i on the calculated result R would be

$$\delta R_{X_i} = \frac{\partial R}{\partial X_i}\delta X_i \tag{C.2}$$

where the partial derivative of R with respect to X_i is the sensitivity coefficient for the results R with respect to the measurement X_i; and δX_i is the uncertainty

in measurement X_i.

The uncertainty in an individual measurement X_i can be estimated at the confidence level of 95% with its bias limit B_{X_i} and the precision index of the mean of the sample S_{X_i}:

$$\delta X_i = \left\{(B_{X_i})^2 + (t_{95} S_{X_i})^2\right\}^{1/2} \tag{C.3}$$

Here t_{95} is the Student's t multiplier for 95% confidence and the degree of freedom of the measurement. (The degree of freedom of a measurement equals the number of observations minus one.) If the degree of freedom is larger than 30, the value of t_{95} can be taken as 2.0.

When several independent variables are used in the function R, the individual terms are combined by a root-sum-square method:

$$\delta R = \left\{\sum_{i=1}^{N} \left(\frac{\partial R}{\partial X_i}\delta X_i\right)^2\right\}^{1/2} \tag{C.4}$$

In particular, whenever the equation describing the result R has the following form:

$$R = X_1^a\, X_2^b\, X_3^c \cdots X_N^m \tag{C.5}$$

then the overall relative uncertainty can be found directly:

$$\frac{\delta R}{R} = \left\{\left(a\frac{\delta X_1}{X_1}\right)^2 + \left(b\frac{\delta X_2}{X_2}\right)^2 + \cdots + \left(m\frac{\delta X_N}{X_N}\right)^2\right\}^{1/2} \tag{C.6}$$

If each individual measurement has the same confidence level of 95% as expressed in Eq. (C.3), the estimated uncertainty in the result R by Eq. (C.4) or Eq. (C.6) will have the same confidence level of 95%.

C.2 Measurement of Radiation Loss

C.2.1 measurement uncertainty

i) total voltage, $V = 4.5\ V$ (typical value for heat sink A)

From the manual of the instrument, the bias (or accuracy) of the measured voltage is

$$B_V = 4.5 \times 0.02\% + 0.004 = 0.0049\ (V)$$

In the experimental measurement, the precision index of the mean is $S_V = 0.001\ (V)$ and $t_{95} = 2.0$. Thus

$$\begin{aligned} \delta V &= \left\{(B_V)^2 + (t_{95}S_V)^2\right\}^{1/2} \\ &= \left\{0.0049^2 + (2 \times 0.001)^2\right\}^{1/2} \\ &= 0.005 \end{aligned}$$

The relative uncertainty is

$$\frac{\delta V}{V} = 0.005/4.5 = 0.0012$$

ii) voltage for the resistor in series with the heaters, $V_1 = 15\,mV$

By the same procedure, the relative uncertainty in V_1 is

$$\frac{\delta V_1}{V_1} = 0.00065$$

iii) current

From Eq. (C.6), the relative uncertainty of the current ($I = V/R$) is

$$\begin{aligned} \frac{\delta I}{I} &= \left\{\left(\frac{\delta V_1}{V_1}\right)^2 + \left(\frac{\delta R_1}{R_1}\right)^2\right\}^{1/2} \\ &= \left\{0.00065^2 + 0.00042^2\right\}^{1/2} \\ &= 0.0008 \end{aligned}$$

where the value of $\delta R_1/R_1$ is from the specifications of the resistor.

iv) radiation loss, $Q_R = VI$

Following the same procedure, the relative uncertainty of the loss is found:

$$\frac{\delta Q_R}{Q_R} = 0.00144$$

For $\Delta T = 50\,K$, the typical Q_R is $0.6\,W$, Thus

$$\delta Q_R = 0.00144 \times 0.6 = 0.000864\ (W) \tag{C.7}$$

v) temperature difference ($\Delta T = T_S - T_w$)

With $\delta T_S = 0.2\,K$, $\delta T_w = 0.3\,K$ and $\Delta T = 50\,K$, the uncertainty of ΔT is obtained by Eq. (C.4):

$$\begin{aligned} \delta\Delta T &= \left\{(\delta T_S)^2 + (\delta T_w)^2\right\}^{1/2} \\ &= \left\{0.2^2 + 0.3^2\right\}^{1/2} \\ &= 0.36\ (K) \end{aligned}$$

C.2.2 uncertainty in the value predicted by the correlation for the radiative loss, $Q_{R,C}$

i) the uncertainty of the fitting (heat sink A)

The correlation of radiation loss was obtained as

$$Q_{R,C} = 0.00107 + 0.0932X - 0.001X^2 \tag{C.8}$$

with

$$X = (T_S^4 - T_w^4) \times 10^{-9}\ \ (K^4)$$

The fitting uncertainty with 95% confidence is $\pm 0.007\ \ (W)$

ii) the uncertainty in $Q_{R,C}$ resulting from δT_S and δT_w in radiation measurement (heat sink A)

With $T_S = 343\ K, \delta T_S = 0.2\ K$, and $T_w = 293\ K, \delta T_w = 0.3\ K$, and from Eq. (C.4), the uncertainty of X is found:

$$\begin{aligned} \delta X &= \left\{(4\,T_S^3\,\delta T_S)^2 + (4\,T_w^3\,\delta T_w)^2\right\}^{1/2} \times 10^{-9} \\ &= 0.044\ \ (K^4) \end{aligned}$$

with $X = 6.5\ \ (K^4)$.

Thus the uncertainty in $Q_{R,C}$ is obtained:

$$\begin{aligned} [\delta Q_{R,C}]_{T_S,T_w} &= (0.0932 - 0.001 \times 2\,X)\,\delta X \\ &= 0.0035\ (W) \end{aligned}$$

iii) the uncertainty in $Q_{R,C}$ resulting from the measurement of Q_R, i.e. from measurements of V and I

$$[\delta Q_{R,C}]_{VI} = \delta Q_R = 0.000864\ (W)$$

iv) the uncertainty due to the ambient temperature variation (see Subsection 3.3.3)

$$[\delta Q_{R,C}]_{ambient} = 0.012\ \ (W)$$

v) the uncertainty of the correlation prediction $Q_{R,C}$

The four uncertainties above are combined by the root-sum-square method, Eq. (C.4):

$$\begin{aligned} \delta Q_{R,C} &= \left\{0.007^2 + 0.0035^2 + 0.000864^2 + 0.012^2\right\}^{1/2} \\ &= 0.017\ (W) \end{aligned} \tag{C.9}$$

and the relative uncertainty of the correlation is

$$\frac{\delta Q_{R,C}}{Q_R} = \frac{0.017}{0.6} = 0.028$$

C.3 Measurement of Natural Convection Heat Transfer

C.3.1 uncertainty of Ra_b^*

From the definition of Ra_b^*:

$$Ra_b^* = \frac{g\,\Delta T\,b^4\,Pr}{\nu^2\,T_\infty\,D}$$

the relative uncertainty of Ra_b^* can be calculated by Eq. (C.6):

$$\frac{\delta Ra_b^*}{Ra_b^*} = \left\{ \left(\frac{\delta \Delta T}{\Delta T}\right)^2 + \left(4\frac{\delta b}{b}\right)^2 + \left(\frac{\delta Pr}{Pr}\right)^2 + \left(2\frac{\delta \nu}{\nu}\right)^2 + \left(\frac{\delta T_\infty}{T_\infty}\right)^2 + \left(\frac{\delta D}{D}\right)^2 \right\}^{1/2} \tag{C.10}$$

In this part of the experiment, typical values related to temperature are $T_\infty = 295\,K$, $\Delta T = 50\,K$, $\delta T_S = 0.25\,K$ and $\delta T_\infty = 0.2\,K$. The uncertainty of ΔT is obtained by Eq. (C.4): $\delta \Delta T = 0.32\,K$ and thus,

$$\frac{\delta \Delta T}{\Delta T} = 0.32/50 = 0.0064$$

For heat sink A, $b = 22.5\,mm$, $\delta b = 0.05\,mm$ and therefore

$$4\,\frac{\delta b}{b} = 4 \times 0.05/22.5 = 0.009$$

For heat sink E, $b = 2\,mm$, $\delta b = 0.02\,mm$ and thus

$$4\,\frac{\delta b}{b} = 4 \times 0.02/2 = 0.04$$

The other values are calculated as follows. (The uncertainties in physical properties are calculated from the round off errors in the tables except ν which is sensitive to changes in the pressure. The experimental pressure condition was the same as that for the table values, i.e. $1\,at = 98 \times 10^3\ N/m^2$.) (Kuzman Raznjevic

1976)

$$\frac{\delta Pr}{Pr} = 0.005/0.71 = 0.007$$

$$\frac{\delta D}{D} = 0.05/36.5 = 0.0014$$

$$\frac{\delta T_\infty}{T_\infty} = 0.2/295 = 0.00068$$

Because $\nu = \mu/\rho$,

$$\frac{\delta \nu}{\nu} = \left\{ \left(\frac{\delta \mu}{\mu}\right)^2 + \left(\frac{\delta \rho}{\rho}\right)^2 \right\}^{1/2}$$

From $\rho = p/RT$ and the atmospheric pressure uncertainty $\delta p/p \approx 1.5\%$ for the measurement period (Brundrett, 1998), the uncertainty of the air density is found:

$$\frac{\delta \rho}{\rho} = \left\{ \left(\frac{\delta T_f}{T_f}\right)^2 + \left(\frac{\delta p}{p}\right)^2 \right\}^{1/2}$$

$$= \left\{ (0.25/318)^2 + 0.15^2 \right\}^{1/2}$$

$$= 0.015$$

From the table, $\delta \mu/\mu = 2.5 \times 10^{-5}$. Thus

$$\frac{\delta \nu}{\nu} = \left\{ \left(\frac{\delta \mu}{\mu}\right)^2 + \left(\frac{\delta \rho}{\rho}\right)^2 \right\}^{1/2}$$

$$= \left\{ (2.5 \times 10^{-5})^2 + 0.015^2 \right\}^{1/2}$$

$$= 0.015$$

and

$$2\frac{\delta \nu}{\nu} = 2 \times 0.015 = 0.03$$

Among them $\delta T_\infty/T_\infty$ and $\delta D/D$ are negligible and finally the uncertainty of Ra_b^* for heat sink A (high Ra_b^*) is

$$\frac{\delta Ra_b^*}{Ra_b^*} = \left\{\left(\frac{\delta\Delta T}{\Delta T}\right)^2 + \left(4\frac{\delta b}{b}\right)^2 + \left(\frac{\delta Pr}{Pr}\right)^2 + \left(2\frac{\delta\nu}{\nu}\right)^2\right\}^{1/2}$$

$$= \left\{0.0064^2 + 0.009^2 + 0.007^2 + 0.03^2\right\}^{1/2}$$

$$= 0.033 \text{ or } 3.3\%$$

For heat sink E (low Ra_b^*) it is

$$\frac{\delta Ra_b^*}{Ra_b^*} = \left\{0.0064^2 + 0.04^2 + 0.007^2 + 0.03^2\right\}^{1/2}$$

$$= 0.051 \text{ or } 5.1\%$$

Therefore the uncertainty in the Rayleigh number is $\pm 3.3\%$ for $Ra_b^* \approx 2.6 \times 10^4$, and $\pm 5.1\%$ for $Ra_b^* \approx 1.5$.

C.3.2 uncertainty of Nu_b

From the definition of Nu_b:

$$Nu_b = \frac{Q_{Conv}\, b}{k\,\Delta T\, A}$$

the relative uncertainty of Nu_b can be calculated by Eq. (C.6):

$$\frac{\delta Nu_b}{Nu_b} = \left\{\left(\frac{\delta Q_{Conv}}{Q_{Conv}}\right)^2 + \left(\frac{\delta b}{b}\right)^2 + \left(\frac{\delta k}{k}\right)^2 + \left(\frac{\delta\Delta T}{\Delta T}\right)^2 + \left(\frac{\delta A}{A}\right)^2\right\}^{1/2} \qquad \text{(C.11)}$$

In this part of the experiment, the typical power supplied to the heaters is $Q = 5\,W$, the heat loss by radiation is $Q_R = 0.6\,W$ (known from radiation loss measurement), and the additional wire loss is $\Delta Q_{WIR} \approx 0.09\,W$ (Appendix B), so the heat flow rate due to the convection is

$$Q_{Conv} = Q - Q_R - \Delta Q_{WIR}$$

$$= 5 - 0.6 - 0.09$$

$$= 4.31\ (W) \tag{C.12}$$

By the same procedure as in the calculation for measurement of radiation loss, the uncertainty of Q is

$$\delta Q = 0.0072\ (W)$$

In the natural convection measurements, with $T_S = 343\ K$, $\delta T_S = 0.25\ K$, $T_\infty = 293\ K$, and $\delta T_\infty = 0.2\ K$, the uncertainty of radiation loss resulting from δT_S and δT_∞ is calculated as follows.

$$\begin{aligned} \delta X &= \left\{(4\,T_S^3\,\delta T_S)^2 + (4\,T_\infty^3\,\delta T_\infty)^2\right\}^{1/2} \times 10^{-9} \\ &= 0.045\ \ (K^4) \end{aligned}$$

and

$$X = (T_S^4 - T_\infty^4) \times 10^{-9} = 6.5\ \ (K^4)$$

Thus the uncertainty of radiation loss resulting from δT_S and δT_∞ is

$$\begin{aligned} [\delta Q_{R,C}]_{T_S,T_\infty} &= (0.0932 + 2 \times 0.001\,X)\delta X \\ &= 0.0036\ (W) \end{aligned}$$

which is combined with the uncertainty of the correlation, i.e. $\delta Q_{R,C}$, Eq. (C.9), by the root-sum-square method, Eq. (C.4), to give the uncertainty of Q_R for measurement of natural convection:

$$\begin{aligned} \delta Q_{R,2} &= \left\{0.017^2 + 0.0036^2\right\}^{1/2} \\ &= 0.017\ (W) \end{aligned} \tag{C.13}$$

The relative uncertainty in the additional wire loss calculated using the procedure in Appendix B should be within 10%, thus the uncertainty of ΔQ_{WIR} is

$$\begin{aligned} \delta\Delta Q_{WIR} &= 0.1 \times 0.092 \\ &= 0.009\ (W) \end{aligned}$$

Thus the uncertainty of Q_{Conv} is obtained using Eq. (C.4):

$$\begin{aligned} \delta Q_{Conv} &= \left\{(\delta Q)^2 + (\delta Q_{R,2})^2 + (\delta\Delta Q_{WIR})^2\right\}^{1/2} \\ &= \left\{0.0072^2 + 0.017^2 + 0.009^2\right\}^{1/2} \\ &= 0.021\ (W) \end{aligned}$$

and hence

$$\frac{\delta Q_{Conv}}{Q_{Conv}} = 0.021/4.31 = 0.0049$$

The other values are as follows.

$$\begin{aligned} \frac{\delta k}{k} &= 0.00005/0.0293 = 0.002 \\ \frac{\delta b}{b} &= 0.05/22.5 = 0.002 \\ \frac{\delta A}{A} &= 0.01 \end{aligned}$$

Then the uncertainty of Nu_b of heat sink A (high Ra_b^*) can be calculated:

$$\begin{aligned} \frac{\delta Nu_b}{Nu_b} &= \left\{0.0049^2 + 0.002^2 + 0.002^2 + 0.0064^2 + 0.01^2\right\}^{1/2} \\ &= 0.013 \text{ or } 1.3\% \end{aligned} \tag{C.14}$$

For heat sink E (low Ra_b^*) $b = 1\,mm$ and $\delta b/b = 0.01$ the uncertainty is

$$\frac{\delta Nu_b}{Nu_b} = 0.016 \text{ or } 1.6\% \tag{C.15}$$

Therefore the uncertainty in the Nusselt number is $\pm 1.3\%$ for $Nu_b \approx 6.9$, and $\pm 1.6\%$ for $Nu_b \approx 0.36$.

Appendix D

Tables of Comparisons with Previous Correlations

The present simplified model with $n = 1$ is compared with the three previous correlations in the following tables. In each of the comparisons the heat sink dimensions adopted for the present model are the same as those used in the experiments for the corresponding previous correlation (referring to Table 2.5). And Ra_D is fixed. Ra_b^* varies with b/D. The percent difference is given in the form:

$$\frac{Nu_b - Nu_b(reference)}{Nu_b(reference)} \times 100\%$$

and the present model is the reference in the comparisons.

D.1 Edwards-Chaddock Correlations

In Table D.1 through Table D.6, the present model is compared with the Edwards-Chaddock correlations of both copper and aluminum fin for the diameter ratios $D/d = 1.94$, 2.97 and 5.17.

D.2 Jones-Nwizu Correlations

In Table D.7 and Table D.8, the present model is compared with the Jones-Nwizu correlation for the diameter ratios $D/d = 1.67$, and 1.94.

D.3 Tsubouchi-Masuda Correlations

In Table D.9 through Table D.11, the present model is compared with the Tsubouchi-Masuda correlations for the diameter ratios $D/d = 1.94$, 2.97 and 5.17.

Table D.1: Results for Edwards-Chaddock Heat Sink (1).

(copper fins, $D/d = 1.94$)

Ra_b^*	Edwards-Chaddock Nu_b	Present Model Nu_b	% Diff.
1.000×10^0	0.125	0.106	18.3
1.585×10^0	0.161	0.137	17.2
2.512×10^0	0.208	0.181	14.6
3.981×10^0	0.267	0.240	11.4
6.310×10^0	0.345	0.319	8.1
1.000×10^1	0.444	0.420	5.7
1.585×10^1	0.572	0.547	4.6
2.512×10^1	0.737	0.700	5.2
3.981×10^1	0.941	0.879	7.1
6.310×10^1	1.182	1.082	9.3
1.000×10^2	1.448	1.307	10.8
1.585×10^2	1.731	1.553	11.4
2.512×10^2	2.030	1.822	11.4
3.981×10^2	2.348	2.116	11.0
6.310×10^2	2.690	2.437	10.4
1.000×10^3	3.062	2.790	9.7
1.585×10^3	3.471	3.181	9.1
2.512×10^3	3.924	3.615	8.6
3.981×10^3	4.428	4.099	8.0
6.310×10^3	4.992	4.640	7.6
1.000×10^4	5.624	5.247	7.2

RMS Diff = 10.4%

Table D.2: Results for Edwards-Chaddock Heat Sink (2).

(aluminum fins, $D/d = 1.94$)

Ra_b^*	Edwards-Chaddock Nu_b	Present Model Nu_b	% Diff.
1.000×10^0	0.146	0.106	38.5
1.585×10^0	0.183	0.137	33.4
2.512×10^0	0.230	0.181	26.9
3.981×10^0	0.288	0.240	19.9
6.310×10^0	0.361	0.319	13.3
1.000×10^1	0.452	0.420	7.7
1.585×10^1	0.567	0.547	3.6
2.512×10^1	0.711	0.700	1.5
3.981×10^1	0.891	0.879	1.3
6.310×10^1	1.114	1.082	3.0
1.000×10^2	1.384	1.307	5.9
1.585×10^2	1.694	1.553	9.0
2.512×10^2	2.037	1.822	11.8
3.981×10^2	2.410	2.116	13.9
6.310×10^2	2.817	2.437	15.6
1.000×10^3	3.264	2.790	17.0
1.585×10^3	3.759	3.181	18.2
2.512×10^3	4.313	3.615	19.3
3.981×10^3	4.936	4.099	20.4
6.310×10^3	5.640	4.640	21.5
1.000×10^4	6.437	5.247	22.7

RMS Diff = 18.3%

Table D.3: Results for Edwards-Chaddock Heat Sink (3).

(copper fins, $D/d = 2.97$)

Ra_b^*	Edwards-Chaddock Nu_b	Present Model Nu_b	% Diff.
1.000×10^0	0.125	0.090	40.0
1.585×10^0	0.160	0.119	34.2
2.512×10^0	0.204	0.161	27.0
3.981×10^0	0.261	0.218	19.6
6.310×10^0	0.333	0.295	12.7
1.000×10^1	0.424	0.396	7.1
1.585×10^1	0.542	0.525	3.2
2.512×10^1	0.691	0.682	1.3
3.981×10^1	0.877	0.867	1.1
6.310×10^1	1.099	1.079	1.9
1.000×10^2	1.349	1.314	2.7
1.585×10^2	1.620	1.573	3.0
2.512×10^2	1.911	1.854	3.0
3.981×10^2	2.222	2.160	2.9
6.310×10^2	2.561	2.494	2.7
1.000×10^3	2.932	2.859	2.5
1.585×10^3	3.343	3.262	2.5
2.512×10^3	3.802	3.708	2.5
3.981×10^3	4.317	4.205	2.7
6.310×10^3	4.896	4.759	2.9
1.000×10^4	5.549	5.381	3.1

RMS Diff = 14.1%

Table D.4: Results for Edwards-Chaddock Heat Sink (4).

(aluminum fins, $D/d = 2.97$)

Ra_b^*	Edwards-Chaddock Nu_b	Present Model Nu_b	% Diff.
1.000×10^0	0.116	0.090	29.9
1.585×10^0	0.149	0.119	24.5
2.512×10^0	0.190	0.161	18.0
3.981×10^0	0.242	0.218	11.1
6.310×10^0	0.309	0.295	4.7
1.000×10^1	0.394	0.396	-0.6
1.585×10^1	0.500	0.525	-4.7
2.512×10^1	0.627	0.682	-8.1
3.981×10^1	0.772	0.867	-11.0
6.310×10^1	0.933	1.079	-13.5
1.000×10^2	1.111	1.314	-15.5
1.585×10^2	1.309	1.573	-16.8
2.512×10^2	1.531	1.854	-17.5
3.981×10^2	1.781	2.160	-17.6
6.310×10^2	2.066	2.494	-17.2
1.000×10^3	2.391	2.859	-16.4
1.585×10^3	2.763	3.262	-15.3
2.512×10^3	3.192	3.708	-13.9
3.981×10^3	3.684	4.205	-12.4
6.310×10^3	4.251	4.759	-10.7
1.000×10^4	4.904	5.381	-8.9

RMS Diff = 15.2%

Table D.5: Results for Edwards-Chaddock Heat Sink (5).

(copper fins, $D/d = 5.17$)

Ra_b^*	Edwards-Chaddock Nu_b	Present Model Nu_b	% Diff.
1.000×10^0	0.106	0.084	27.0
1.585×10^0	0.137	0.113	21.7
2.512×10^0	0.177	0.154	15.2
3.981×10^0	0.228	0.210	8.4
6.310×10^0	0.294	0.287	2.2
1.000×10^1	0.379	0.390	-2.8
1.585×10^1	0.488	0.520	-6.2
2.512×10^1	0.626	0.681	-8.0
3.981×10^1	0.794	0.872	-9.0
6.310×10^1	0.983	1.091	-9.9
1.000×10^2	1.188	1.335	-11.1
1.585×10^2	1.404	1.604	-12.4
2.512×10^2	1.633	1.896	-13.9
3.981×10^2	1.877	2.213	-15.1
6.310×10^2	2.142	2.557	-16.2
1.000×10^3	2.431	2.932	-17.1
1.585×10^3	2.750	3.345	-17.8
2.512×10^3	3.105	3.800	-18.3
3.981×10^3	3.501	4.306	-18.7
6.310×10^3	3.945	4.870	-19.0
1.000×10^4	4.442	5.501	-19.3

RMS Diff =15.1%

Table D.6: Results for Edwards-Chaddock Heat Sink (6).

(aluminum fins, $D/d = 5.17$)

Ra_b^*	Edwards-Chaddock Nu_b	Present Model Nu_b	% Diff.
1.000×10^0	0.085	0.084	0.8
1.585×10^0	0.112	0.113	-0.6
2.512×10^0	0.149	0.154	-3.2
3.981×10^0	0.197	0.210	-6.2
6.310×10^0	0.262	0.287	-9.0
1.000×10^1	0.347	0.390	-10.9
1.585×10^1	0.460	0.520	-11.5
2.512×10^1	0.607	0.681	-10.8
3.981×10^1	0.788	0.872	-9.6
6.310×10^1	0.997	1.091	-8.6
1.000×10^2	1.226	1.335	-8.2
1.585×10^2	1.471	1.604	-8.3
2.512×10^2	1.734	1.896	-8.5
3.981×10^2	2.019	2.213	-8.8
6.310×10^2	2.331	2.557	-8.8
1.000×10^3	2.676	2.932	-8.7
1.585×10^3	3.062	3.345	-8.4
2.512×10^3	3.496	3.800	-8.0
3.981×10^3	3.985	4.306	-7.5
6.310×10^3	4.539	4.870	-6.8
1.000×10^4	5.166	5.501	-6.1

RMS Diff = 8.1%

Table D.7: Results for Jones-Nwizu Heat Sink (1).

($D/d = 1.67$)

Ra_b^*	Jones-Nwizu Nu_b	Present Model Nu_b	% Diff.
1.000×10^0	0.116	0.132	-12.3
1.585×10^0	0.148	0.165	-10.5
2.512×10^0	0.189	0.210	-9.9
3.981×10^0	0.241	0.269	-10.2
6.310×10^0	0.308	0.346	-10.9
1.000×10^1	0.393	0.444	-11.4
1.585×10^1	0.502	0.564	-11.1
2.512×10^1	0.640	0.709	-9.7
3.981×10^1	0.813	0.876	-7.2
6.310×10^1	1.019	1.065	-4.3
1.000×10^2	1.252	1.274	-1.8
1.585×10^2	1.504	1.503	0.1
2.512×10^2	1.774	1.752	1.2
3.981×10^2	2.064	2.024	2.0
6.310×10^2	2.379	2.322	2.5
1.000×10^3	2.725	2.649	2.8
1.585×10^3	3.108	3.011	3.2
2.512×10^3	3.536	3.412	3.6
2.512×10^3	3.536	3.412	3.6
2.512×10^3	3.536	3.412	3.6
2.512×10^3	3.536	3.412	3.6

RMS Diff = 7.6%

Table D.8: Results for Jones-Nwizu Heat Sink (2).

($D/d = 1.94$)

Ra_b^*	Jones-Nwizu Nu_b	Present Model Nu_b	% Diff.
1.000×10^0	0.116	0.118	-1.7
1.585×10^0	0.148	0.150	-1.0
2.512×10^0	0.189	0.192	-1.8
3.981×10^0	0.241	0.250	-3.5
6.310×10^0	0.308	0.326	-5.6
1.000×10^1	0.393	0.424	-7.3
1.585×10^1	0.502	0.546	-8.1
2.512×10^1	0.640	0.693	-7.7
3.981×10^1	0.813	0.865	-6.0
6.310×10^1	1.019	1.059	-3.7
1.000×10^2	1.252	1.274	-1.8
1.585×10^2	1.504	1.510	-0.4
2.512×10^2	1.774	1.767	0.4
3.981×10^2	2.064	2.046	0.9
6.310×10^2	2.379	2.351	1.2
1.000×10^3	2.725	2.685	1.5
1.585×10^3	3.108	3.054	1.8
2.512×10^3	3.536	3.463	2.1
2.512×10^3	3.536	3.463	2.1
2.512×10^3	3.536	3.463	2.1
2.512×10^3	3.536	3.463	2.1

RMS Diff = 4.0%

Table D.9: Results for Tsubouchi-Masuda Heat Sink (1).

($D/d = 1.94$)

Ra_b^*	Tsubouchi-Masuda Nu_b	Present Model Nu_b	% Diff.
1.000×10^0	0.101	0.123	-18.0
1.585×10^0	0.132	0.155	-15.2
2.512×10^0	0.174	0.199	-12.7
3.981×10^0	0.232	0.258	-10.3
6.310×10^0	0.310	0.336	-7.8
1.000×10^1	0.412	0.436	-5.5
1.585×10^1	0.539	0.560	-3.7
2.512×10^1	0.690	0.709	-2.7
3.981×10^1	0.861	0.884	-2.5
6.310×10^1	1.050	1.081	-2.9
1.000×10^2	1.254	1.301	-3.6
1.585×10^2	1.474	1.542	-4.4
2.512×10^2	1.711	1.805	-5.2
3.981×10^2	1.968	2.091	-5.9
6.310×10^2	2.248	2.405	-6.5
1.000×10^3	2.555	2.750	-7.1
1.585×10^3	2.893	3.132	-7.6
2.512×10^3	3.267	3.555	-8.1
3.981×10^3	3.682	4.028	-8.6
6.310×10^3	4.143	4.556	-9.1
1.000×10^4	4.657	5.147	-9.5

RMS Diff = 8.5%

Table D.10: Results for Tsubouchi-Masuda Heat Sink (2).

($D/d = 2.97$)

Ra_b^*	Tsubouchi-Masuda Nu_b	Present Model Nu_b	% Diff.
1.000×10^0	0.099	0.107	-7.5
1.585×10^0	0.133	0.138	-3.4
2.512×10^0	0.180	0.180	0.4
3.981×10^0	0.246	0.237	3.8
6.310×10^0	0.334	0.314	6.7
1.000×10^1	0.451	0.413	9.0
1.585×10^1	0.596	0.540	10.4
2.512×10^1	0.768	0.693	10.7
3.981×10^1	0.964	0.875	10.2
6.310×10^1	1.180	1.081	9.1
1.000×10^2	1.414	1.312	7.8
1.585×10^2	1.666	1.565	6.5
2.512×10^2	1.938	1.840	5.3
3.981×10^2	2.232	2.140	4.3
6.310×10^2	2.553	2.466	3.5
1.000×10^3	2.905	2.824	2.9
1.585×10^3	3.292	3.217	2.3
2.512×10^3	3.720	3.653	1.8
3.981×10^3	4.195	4.138	1.4
6.310×10^3	4.724	4.678	1.0
1.000×10^4	5.314	5.284	0.6

RMS Diff = 6.2%

Table D.11: Results for Tsubouchi-Masuda Heat Sink (3).

($D/d = 5.17$)

Ra_b^*	Tsubouchi-Masuda Nu_b	Present Model Nu_b	% Diff.
1.000×10^0	0.082	0.094	-12.5
1.585×10^0	0.116	0.124	-5.9
2.512×10^0	0.167	0.165	1.1
3.981×10^0	0.239	0.221	7.8
6.310×10^0	0.339	0.298	13.6
1.000×10^1	0.469	0.399	17.6
1.585×10^1	0.632	0.528	19.6
2.512×10^1	0.822	0.687	19.7
3.981×10^1	1.036	0.875	18.4
6.310×10^1	1.271	1.090	16.5
1.000×10^2	1.524	1.331	14.4
1.585×10^2	1.795	1.596	12.5
2.512×10^2	2.088	1.884	10.9
3.981×10^2	2.405	2.195	9.6
6.310×10^2	2.750	2.534	8.5
1.000×10^3	3.129	2.903	7.8
1.585×10^3	3.546	3.309	7.2
2.512×10^3	4.008	3.756	6.7
3.981×10^3	4.522	4.251	6.4
6.310×10^3	5.095	4.803	6.1
1.000×10^4	5.735	5.420	5.8

RMS Diff = 12.0%

Appendix E

Comparisons of Present Simplified and Full Models

The simplified model is compared with the full model in the following tables and figures, with $n = 1$ for both models. The four cases presented cover the practical ranges of D/d and Ra_b^*. In these comparisons, Ra_D is fixed, Ra_b^* varies with b/D. In the comparisons, the percent difference is given in the form:

$$\frac{Nu_b - Nu_b(reference)}{Nu_b(reference)} \times 100\%$$

and the full model is the reference.

Excellent agreement can be seen in the comparisons. The comparisons show that in the applicable ranges of D/d and Ra_b^*, the simplified model represents well the full model.

Table E.1: Comparison of Simplified Model and Full Model.

$(D/d = 1.66)$

Ra_b^*	Simplified Model Nu_b	Full Model Nu_b	% Diff.
3.162×10^{-1}	0.225	0.223	0.9
1.000×10^{0}	0.312	0.313	-0.4
3.162×10^{0}	0.447	0.452	-1.0
1.000×10^{1}	0.664	0.670	-0.8
3.162×10^{1}	0.992	0.996	-0.3
1.000×10^{2}	1.446	1.450	-0.3
3.162×10^{2}	2.037	2.048	-0.5
1.000×10^{3}	2.806	2.825	-0.7
3.162×10^{3}	3.818	3.844	-0.7
1.000×10^{4}	5.168	5.193	-0.5
3.162×10^{4}	6.979	6.993	-0.2
1.000×10^{5}	9.412	9.401	0.1

RMS Diff = 0.6%

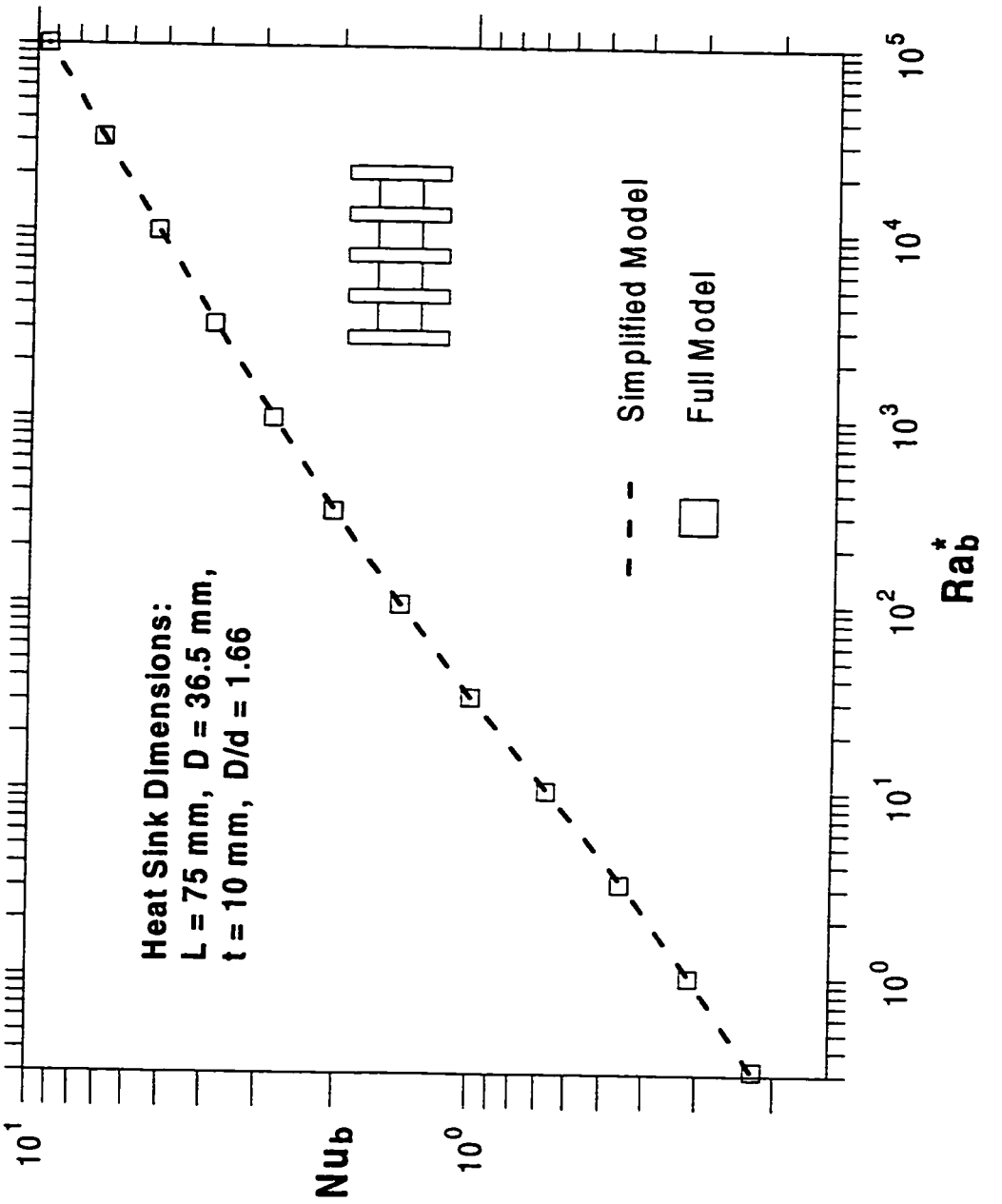

Figure E.1: Comparison of Simplified Model and Full Model($D/d = 1.66$).

Table E.2: Comparison of Simplified Model and Full Model.

$(D/d = 1.94)$

Ra_b^*	Simplified Model Nu_b	Full Model Nu_b	% Diff.
1.000×10^0	0.106	0.115	-7.8
3.162×10^0	0.208	0.226	-7.9
1.000×10^1	0.420	0.442	-4.9
3.162×10^1	0.787	0.804	-2.1
1.000×10^2	1.307	1.321	-1.1
3.162×10^2	1.966	1.989	-1.2
1.000×10^3	2.790	2.828	-1.3
3.162×10^3	3.850	3.901	-1.3
1.000×10^4	5.247	5.304	-1.1
3.162×10^4	7.115	7.162	-0.7
1.000×10^5	9.625	9.640	-0.2

RMS Diff = 3.8%

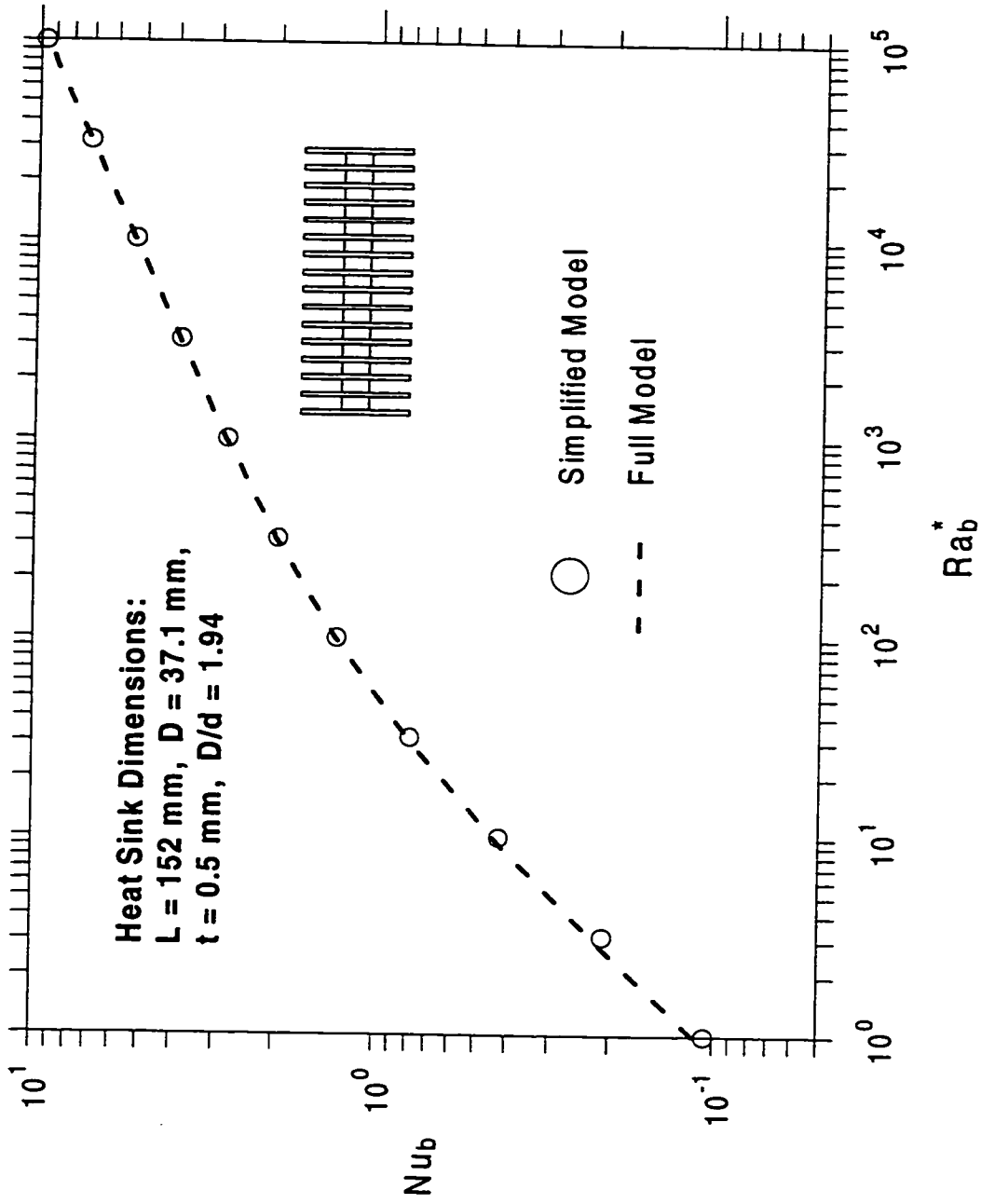

Figure E.2: Comparison of Simplified Model and Full Model($D/d = 1.94$).

Table E.3: Comparison of Simplified Model and Full Model.

$(D/d = 2.97)$

Ra_b^*	Simplified Model Nu_b	Full Model Nu_b	% Diff.
1.000×10^0	0.090	0.092	-2.3
3.162×10^0	0.187	0.196	-4.3
1.000×10^1	0.396	0.408	-2.7
3.162×10^1	0.771	0.775	-0.5
1.000×10^2	1.314	1.305	0.7
3.162×10^2	2.004	1.984	1.0
1.000×10^3	2.859	2.835	0.9
3.162×10^3	3.949	3.923	0.7
1.000×10^4	5.381	5.355	0.5
3.162×10^4	7.296	7.268	0.4
1.000×10^5	9.876	9.843	0.3

RMS Diff = 1.8%

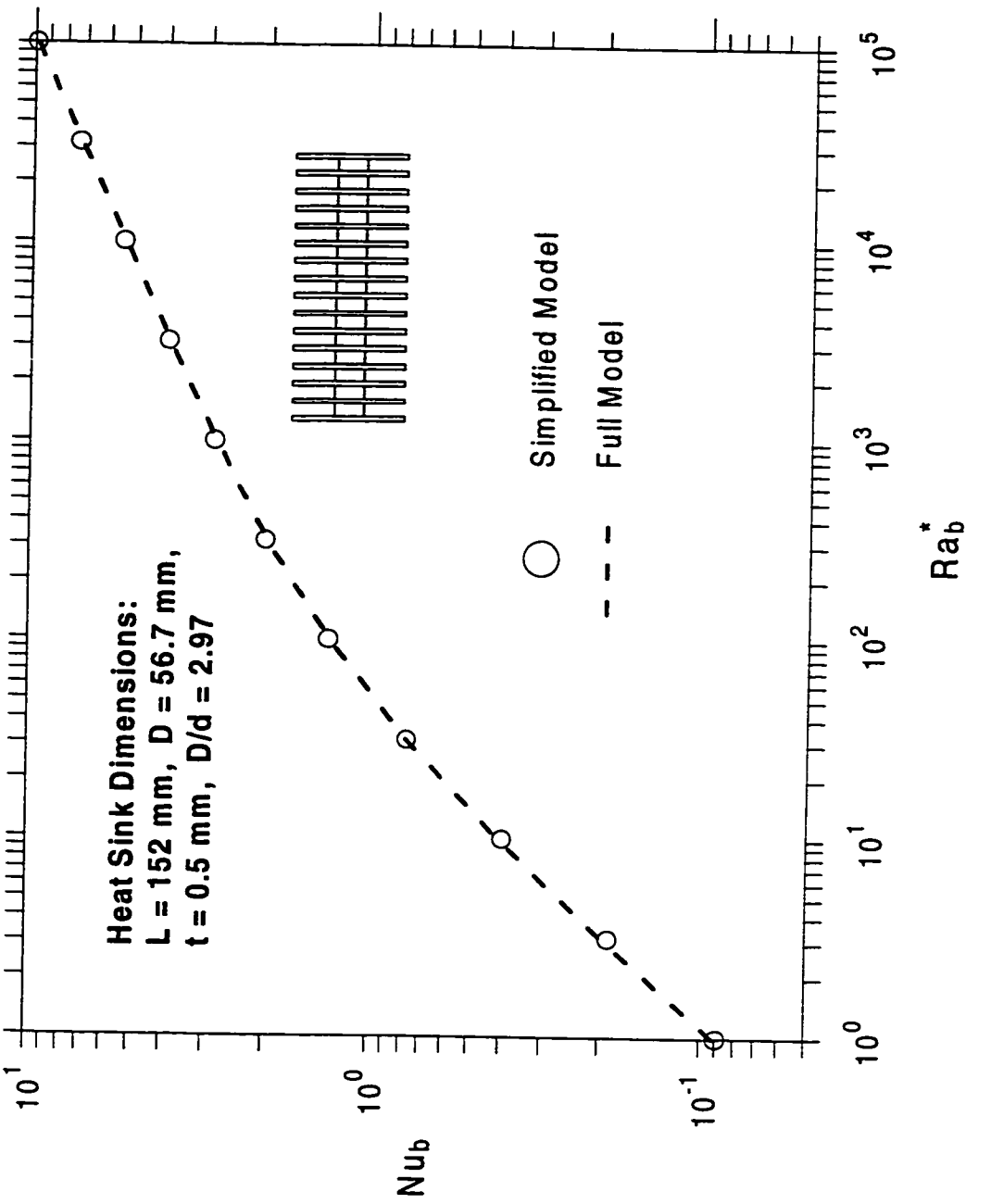

Figure E.3: Comparison of Simplified Model and Full Model($D/d = 2.97$).

Table E.4: Comparison of Simplified Model and Full Model.

$(D/d = 5.17)$

Ra_b^*	Simplified Model Nu_b	Full Model Nu_b	% Diff.
1.000×10^0	0.084	0.078	7.3
3.162×10^0	0.180	0.177	1.3
1.000×10^1	0.390	0.388	0.3
3.162×10^1	0.773	0.762	1.4
1.000×10^2	1.335	1.303	2.5
3.162×10^2	2.051	1.993	2.9
1.000×10^3	2.932	2.848	2.9
3.162×10^3	4.046	3.938	2.8
1.000×10^4	5.501	5.367	2.5
3.162×10^4	7.437	7.275	2.2
1.000×10^5	10.043	9.850	2.0

RMS Diff = 3.1%

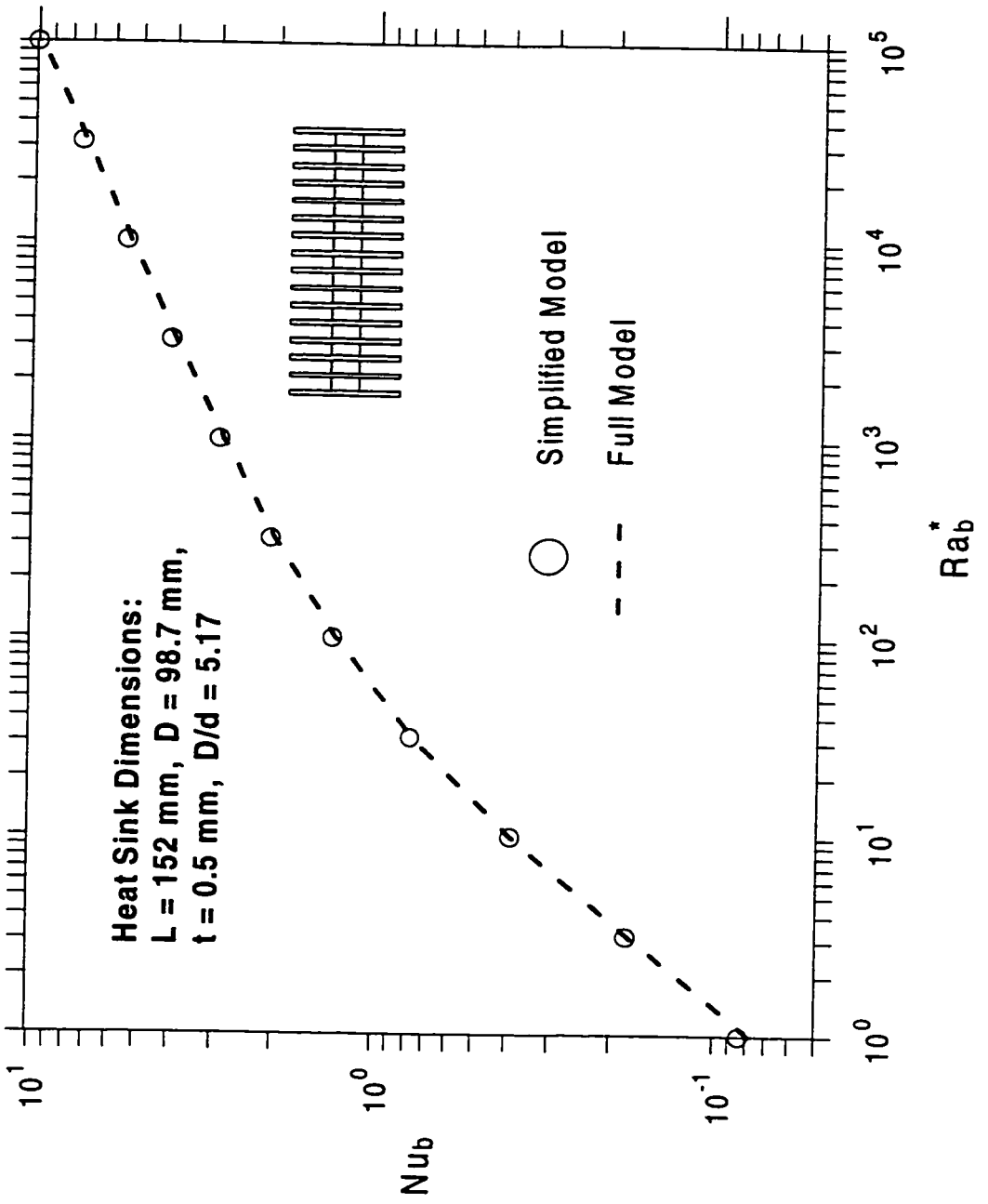

Figure E.4: Comparison of Simplified Model and Full Model($D/d = 5.17$).

Appendix F

Summary of Present Models

The proposed full model is based on the development of the models for inner and outer surfaces.

The model for the inner surface consists of two limiting solutions: the solution for thin boundary layer flow and the solution for fully developed flow. Coupling the two limiting solutions provides the model for the inner surface over the entire range of Ra_b^*.

The model for the outer surface is the thin boundary layer solution for the surface.

Finally the two models for the inner and the outer surfaces are combined with the diffusive limit of the heat sink to form the full model for the heat sink.

The model structure is shown in Fig. F.1.

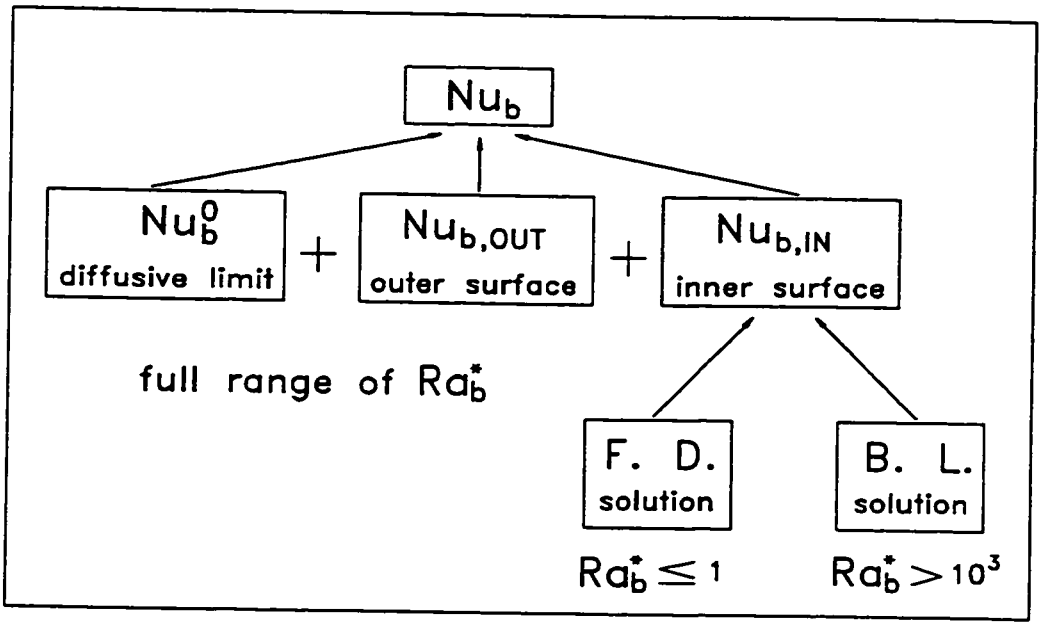

Figure F.1: Model Composition.

F.1 Model for Inner Surface

F.1.1 Thin Boundary Layer Flow Solution

The thin boundary layer Nusselt number for the inner surface is calculated using Eq. (4.24):

$$Nu_{b,A_{IN-T}} = F(Pr)\, G_{\sqrt{A_{IN}}}\, (D/\sqrt{A_{IN}})^{1/4}\, Ra_b^{*1/4} \tag{F.1}$$

where the body gravity function of the inner surface is obtained using the following procedure.

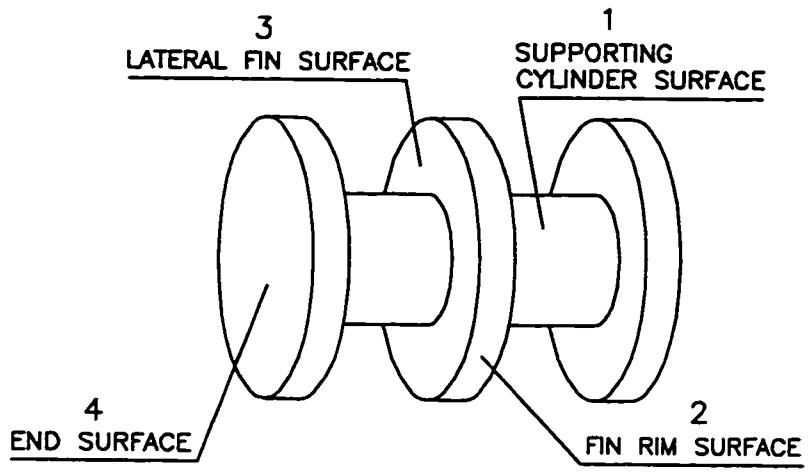

Figure F.2: Heat Sink Surfaces.

As shown in Fig. F.2, the body gravity function for support cylinder surface 1, $G_{\sqrt{A_1}}$, can be calculated using Eq. (4.27):

$$G_{\sqrt{A_1}} = 0.891 \left(\frac{b}{d}\right)^{1/8} \tag{F.2}$$

where b and d are the length and the diameter of the support cylinder respectively.

The body gravity function of lateral fin surface 3 can be calculated using Eq. (4.28) with reference to Fig. 4.5:

$$G_{\sqrt{A}} = \frac{1}{A^{7/8}} \int_0^W S(z)^{3/4}\, dz \tag{F.3}$$

In order to account for the effect of the plume rising from the support cylinder upon the lateral fin surface, as shown in Fig. F.3, the heat transfer rate from area P is reduced by half. Then the body gravity functions of all the inner surface components are combined using Eq. (4.21) for parallel components to give the body gravity function of the inner surface, $G_{\sqrt{A_{IN}}}$:

$$G_{\sqrt{A_{IN}}} = \sum_{i=1}^{N} G_{\sqrt{A_i}} \, (A_i/A_{IN})^{7/8} \tag{F.4}$$

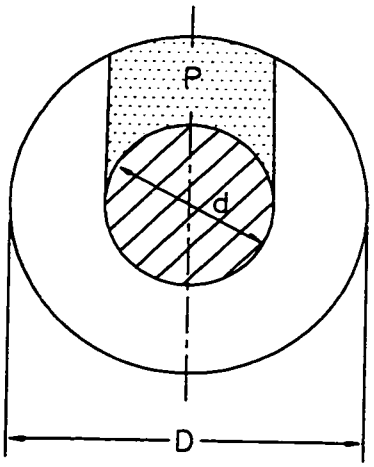

Figure F.3: Area Affected by Cylinder Plume.

F.1.2 Fully Developed Flow Solution

Heat transfer due to channel flow:

Based on the channel surface area, A_{CL}, the Nusselt number for this channel flow is

$$Nu_{b,CLF} = \frac{1}{12} Ra_b^* \frac{D\sqrt{D^2 - d^2}}{A_{CL}} \tag{F.5}$$

Heat transfer due to outward conduction:

The Nusselt number for this part of heat transfer is calculated using Eq. (4.24):

$$Nu_{b,A_{CCS}} = F(Pr)\, G_{\sqrt{A_{CCS}}} \, (D/\sqrt{A_{CCS}})^{1/4} \, Ra_b^{*1/4} \tag{F.6}$$

where the body gravity function of the control surface, $G_{\sqrt{A_{CCS}}}$, can be obtained

using Eq. (4.35).

$$G_{\sqrt{A_{CCS}}} = 0.891 \left(\frac{b}{D}\right)^{1/8} \tag{F.7}$$

Then the Nusselt number is converted to the channel surface to be based on the same surface area as $Nu_{b,CLF}$:

$$Nu_{b,CCS} = Nu_{b,A_{CCS}} A_{CCS}/A_{CL} \tag{F.8}$$

Thus the heat transfer from the inner surface in the fully developed regime is

$$Nu_{b,A_{IN-FU}} = Nu_{b,CLF} + Nu_{b,CCS} \tag{F.9}$$

F.1.3 Combining Two Limiting Solutions

The two limiting solutions for the inner surface are blended as

$$Nu_{b,A_{IN}} = \frac{1}{\left[(1/Nu_{b,A_{IN-T}})^n + (1/Nu_{b,A_{IN-FU}})^n \right]^{1/n}} \tag{F.10}$$

By comparison with the present experimental data, previous correlations and experimental data, $n = 1$ was chosen for heat sink applications and the model becomes

$$Nu_{b,A_{IN}} = \frac{1}{1/Nu_{b,A_{IN-T}} + 1/Nu_{b,A_{IN-FU}}} \tag{F.11}$$

F.1.4 Channel Model

For channel heat transfer ($D/d >> 1$ and without the outer surface heat transfer), Eq. (F.9) will be replaced by

$$Nu_{b,A_{IN-FD}} = Nu_{b,CLF} \tag{F.12}$$

In this case, $n = 1.7$ was chosen based on the comparisons with Tsubouchi-Masuda (1970) channel correlation.

F.2 Thin Boundary Layer Model for Outer Surface

The body gravity functions of the fin rim and the end surface can be found using Eq. (4.41):

$$G_{\sqrt{A}_{RIM}} = 0.891 \left(\frac{t}{D}\right)^{1/8} \tag{F.13}$$

and Eq. (4.42):

$$G_{\sqrt{A}_{END}} = 1.021 \tag{F.14}$$

and then combined using Eq. (4.21) for parallel components to give the body gravity function of the outer surface, $G_{\sqrt{A}_{OUT}}$. The thin boundary layer heat transfer from the outer surface then is calculated using Eq. (4.24):

$$Nu_{b,A_{OUT}} = F(Pr) G_{\sqrt{A}_{OUT}} (D/\sqrt{A}_{OUT})^{1/4} Ra_b^{*1/4} \tag{F.15}$$

F.3 Effective Diffusive Limit

Based on the characteristic length b and the heat sink surface area, the diffusive limit of the heat sink is

$$Nu_b^0 = \frac{3.1915 + 2.7726(L/D)^{0.76}}{\sqrt{1+2(L/D)}} \frac{\sqrt{A_{CC}}\, b}{A_{HS}} \tag{F.16}$$

F.4 Full Model for Heat Sink

The Nusselt number for the inner surface Based on the total surface area of the heat sink, can be written as:

$$Nu_{b,IN} = Nu_{b,A_{IN}} \frac{A_{IN}}{A_{HS}} \tag{F.17}$$

and the Nusselt number for the outer surface is

$$Nu_{b,OUT} = Nu_{b,A_{OUT}} \frac{A_{OUT}}{A_{HS}} \tag{F.18}$$

Finally the total heat transfer from the heat sink is obtained as

$$Nu_b = Nu_b^0 + Nu_{b,OUT} + Nu_{b.IN} \tag{F.19}$$

F.5 Simplified Model

The above Nusselt numbers were simplified as follows. The diffusive limit is

$$Nu_b^0 = [3.36 + 0.087(L/D)]\, \sqrt{A_{CC}}\, b/A_{HS} \tag{F.20}$$

The Nusselt number for the outer surface is

$$Nu_{b,OUT} = [0.499 - 0.026 \ln(t\, N_f/D)]\, Ra_b^{*1/4} A_{OUT}/A_{HS} \tag{F.21}$$

The Nusselt number for the inner surface, $Nu_{b,IN}$, is

$$Nu_{b,IN} = Nu_{b,A_{IN}} \frac{A_{IN}}{A_{HS}} \tag{F.22}$$

with

$$Nu_{b,A_{IN}} = \left[(Nu_{b,A_{IN-T}})^{-n} + (Nu_{b,A_{IN-FD}})^{-n}\right]^{-1/n} \tag{F.23}$$

where $n = 1$ for heat sink applications.

The thin boundary layer Nusselt number for the inner surface can be calculated by

$$Nu_{b,A_{IN-T}} = \left[0.573 - 0.184(d/D) + 0.0388(d/D)^2\right] Ra_b^{*1/4} \tag{F.24}$$

and the fully developed regime Nusselt number for the inner surface, is approximated by

$$\begin{aligned} Nu_{b,A_{IN-FD}} = & \left[0.0323 - 0.0517(d/D) + 0.11(d/D)^2\right] Ra_b^{*1/4} \\ & + \left[0.0516 + 0.0154(d/D) - 0.0433(d/D)^2\right. \\ & \left. + 0.0792(d/D)^3\right] Ra_b^* \end{aligned} \tag{F.25}$$

For the channel model ($D/d >> 1$ and without the outer surface heat transfer), the fully developed regime Nusselt number for the inner surface is

$$\begin{aligned} Nu_{b,A_{IN-FD}} = & \left[0.0516 + 0.0154(d/D) - 0.0433(d/D)^2\right. \\ & \left. + 0.0792(d/D)^3\right] Ra_b^* \end{aligned} \tag{F.26}$$

and the parameter n in Eq. (F.23) is taken as 1.7.

IMAGE EVALUATION TEST TARGET (QA-3)

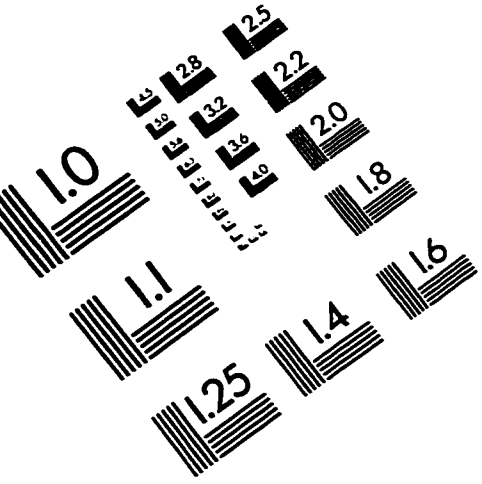

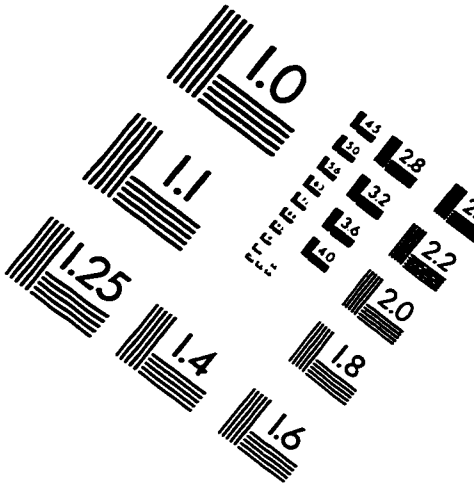

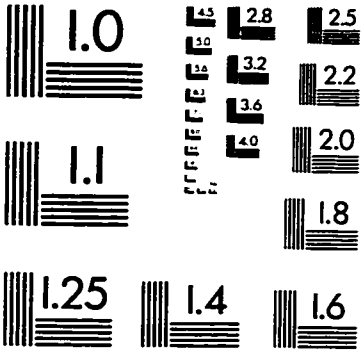

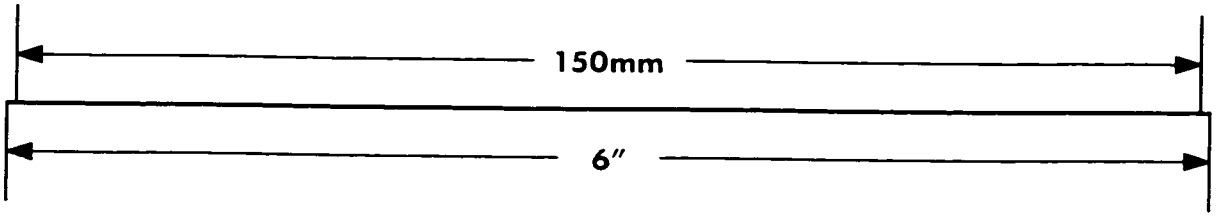

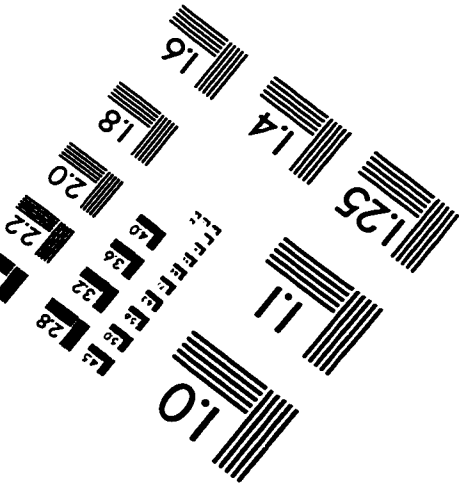

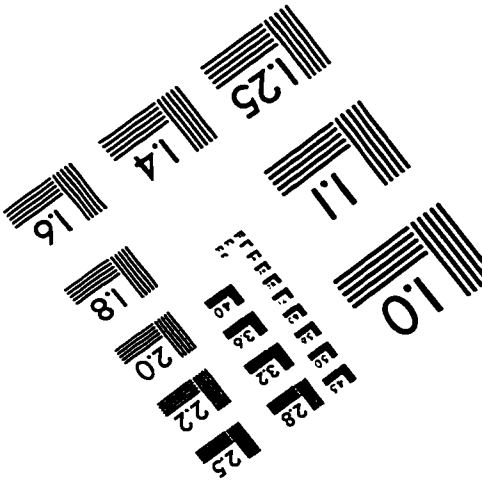

APPLIED IMAGE, Inc
1653 East Main Street
Rochester, NY 14609 USA
Phone: 716/482-0300
Fax: 716/288-5989